Politecnico di Torino

ScuDo
Scuola di Dottorato ~ Doctoral School
WHAT YOU ARE, TAKES YOU FAR

Doctoral Dissertation
Doctoral Program in Electrical, Electronics and Communications Engineering
(38^{th}cycle)

Transverse multi-mode dynamics in VCSELs for high speed applications

By

Martino D'Alessandro

******

Supervisor(s):
Prof. Alberto Tibaldi, Supervisor
Dr. Pierluigi Debernardi, Co-Supervisor
Prof. Francesco Bertazzi, Co-Supervisor

Doctoral Examination Committee:
Prof. Marc Sciamanna
Prof. Franco Prati

Politecnico di Torino
2026

Acknowledgements

I would like to thank my family for their constant support and encouragement throughout these years. A special thanks to Jennifer for her love and support during this journey. I am very grateful to my friends, Giammarco, Dino, Giovanni, Andrea, Gelli, and Farina. Even if we are far apart, it always feels like we are together. A big thanks to my colleagues Alberto, Valerio, Stefania, and Matteo for sharing this journey with me and making it more enjoyable and easier to go through. I would also like to thank my supervisors, Prof. Alberto Tibaldi, Dr. Pierluigi Debernardi, and Prof. Francesco Bertazzi for their guidance and for helping me grow scientifically, as well as all the members of the MOG group. Thanks as well to the colleagues involved in the Eureka project for the collaboration and for providing important experimental results. Finally, I would like to thank the reviewers for their careful reading and helpful scientific feedback.

Abstract

Transverse coupled-cavity vertical-cavity surface-emitting lasers (TCC-VCSEL) have emerged as a promising platform for beam steering, on-chip terahertz generation, and for surpassing the intrinsic modulation bandwidth limitations of conventional VCSELs through the photon–photon resonance (PPR) mechanism. Despite this potential, their practical exploitation remains strongly constrained by high sensitivity to technological imperfections, dynamical instabilities, and the absence of predictive design methodologies.

This thesis introduces a comprehensive, physics-based modeling framework for the multimode dynamics of VCSELs, derived from a modal expansion of the scalar wave equation. The resulting formulation provides a unified description of the rich phenomenology of TCC-VCSELs and, unlike existing phenomenological approaches, explicitly connects geometric and material parameters to the modal coupling coefficients governing device dynamics.

The model is validated through comparison with recent experimental measurements on bow-tie providing physical interpretation of the observed behaviors.

This work establishes a theoretical foundation for the systematic design of next-generation TCC-VCSELs as well as providing general, transferable insights into the multimode dynamics of VCSELs.

Table of contents

Publication list

- **M. D'Alessandro**, V. Torrelli, F. Bertazzi, M. Goano, N. N. Ledentsov, M. Lindemann, M. Gioannini, P. Debernardi, and A. Tibaldi, "Transverse Coupled Cavity VCSELs: Bridging Ultrabroadband Dynamics to Optical Supermodes," IEEE Photonics Journal, vol. 16, no. 2, pp. 1–7, Apr. 2024, Art. no. 0600807, doi: 10.1109/JPHOT.2024.3373171.

- V. Torrelli, **M. D'Alessandro**, W. Elsäßer, and P. Debernardi, "On-demand polarization by a vertical-cavity surface-emitting laser with two tilted sub-wavelength gratings," *Optics Letters*, vol. 49, no. 13, pp. 3773–3776, Jul. 2024, doi: 10.1364/OL.528268.

- V. Torrelli, L. Miri, **M. D'Alessandro**, A. Gullino, M. Zimmer, K. Dahler, M. Jetter, P. Michler, W. Elsäßer, F. Bertazzi, A. Tibaldi, and P. Debernardi, "Elliptical polarization in VCSELs via joint interaction of a tilted sub-wavelength grating and intrinsic semiconductor anisotropies," *Optics Letters*, vol. 50, no. 9, pp. 3082–3085, May 2025, doi: 10.1364/OL.557703.

- A. Gullino, V. Torrelli, **M. D'Alessandro**, A. Tibaldi, F. Bertazzi, M. Goano, and P. Debernardi, "AlGaAs Tunnel Junction (TJ)-VCSELs: A NEGF–Drift-Diffusion Approach," *IEEE Photonics Journal*, vol. 16, no. 2, pp. 1–9, 2024, doi: 10.1109/JPHOT.2024.3360897.

- M. Lindemann, **M. D'Alessandro**, N. Ledentsov, Jr., O. Y. Makarov, N. N. Ledentsov, A. Tibaldi, N. C. Gerhardt, and M. R. Hofmann, "Laterally coupled vertical-cavity surface-emitting lasers with tunable resonance width and frequency," *Journal of Applied Physics*, vol. 138, no. 5, Art. no. 053102, Aug. 2025, doi: 10.1063/5.0275622.

- V. Torrelli, **M. D'Alessandro**, A. Gullino, M. G. C. Alasio, A. Tibaldi, C. Chang-Hasnain, and P. Debernardi, "Elliptically polarized light obtained from tilted high-contrast grating VCSELs," *Optics Letters*, vol. 51, pp. 29–32, 2026.

Conference proceedings

- M. D'Alessandro *et al.*, "Physics-based computer-aided modelling of transverse coupled-cavity VCSELs," in *Proc. SPIE*, Vertical-Cavity Surface-Emitting Lasers XXIX, 2025, doi: 10.1117/12.3042750.

- A. Gullino *et al.*, "Physics-based modeling of AlGaAs tunnel junction VCSELs: A comparative appraisal," in *Proc. Int. Conf. Numerical Simulation of Optoelectronic Devices (NUSOD)*, Turin, Italy, 2023, pp. 99–100, doi: 10.1109/NUSOD59562.2023.10273507.
- N. Ledentsov *et al.*, "Analysis of laterally coupled cavity VCSELs for ultra-high-frequency photon–photon resonance modulation," in *Proc. SPIE*, vol. 12904, Vertical-Cavity Surface-Emitting Lasers XXVIII, 2024, Art. no. 1290405, doi: 10.1117/12.3001177.
- M. Lindemann *et al.*, "Study of electrically excited photon–photon resonances in self-injection-locked coupled-cavity VCSELs," in *Proc. Int. Semiconductor Laser Conf. (ISLC)*, 2024.
- M. D'Alessandro *et al.*, "Physics-oriented model for bow-tie VCSELs," in *Proc. IEEE Photonics Conf. (IPC)*, Rome, Italy, 2024, pp. 1–2, doi: 10.1109/IPC60965.2024.10799891.
- V. Torrelli *et al.*, "Understanding polarization with gratings tilted to crystal axes: Towards circularly polarized VCSELs," in *Proc. IEEE Photonics Conf. (IPC)*, Rome, Italy, 2024, pp. 1–2, doi: 10.1109/IPC60965.2024.10799509.
- A. Gullino *et al.*, "VCSEL thermal sources: A physics-based simulation approach," in *Proc. Int. Conf. Numerical Simulation of Optoelectronic Devices (NUSOD)*, Lodz, Poland, 2025.
- Y. Hu *et al.*, "A coupled-cavity mini-array VCSEL for CW THz generation," in *Proc. SPIE*, vol. 13365, 2025, Art. no. 1336504, doi: 10.1117/12.3038996.
- M. D'Alessandro *et al.*, "Modelling coherent emission in transverse coupled-cavity VCSELs," in *Proc. Int. Conf. Numerical Simulation of Optoelectronic Devices (NUSOD)*, Lodz, Poland, 2025.

Chapter 1

An introduction to VCSELs

Vertical-cavity surface-emitting lasers (VCSELs) are a class of semiconductor lasers that emit light perpendicularly to the wafer surface [1]. First demonstrated in 1977 [2], they differ from the earlier family of edge-emitting lasers (EELs) [3], which emit laterally. This fundamental difference enables on-wafer testing, simplifies fabrication by eliminating the need for facet cleaving, and allows straightforward implementation of large-scale VCSEL arrays. Over time, these technological advantages have established VCSELs as the leading platform across a wide range of applications. Fig. 1.1 illustrates a schematic cross-section of the refractive index profile of a typical circular $Al_xGa_{1-x}As$ VCSEL, together with typical dimensions. Such a structure can be described from two complementary perspectives. From the *optical standpoint*, it acts as a resonant cavity, *i.e.*, a dielectric structure capable of confining light. Vertical confinement (*i.e.*, along the z-direction, perpendicular to the wafer surface) is provided by two distributed Bragg reflectors (DBRs), consisting of alternating high- and low-refractive index layers of $\lambda/4$ optical thickness, realized by varying the aluminum molar fraction in the AlGaAs alloy. Lateral confinement is provided by the oxide aperture (shown on the left of Fig. 1.1), formed by a selectively-oxidized Al_2O_3 layer with a refractive index lower than that of AlGaAs. The device is typically grown epitaxially on a GaAs substrate and terminated with a GaAs cap layer, which protects the structure from unintentional oxidation. Additional surface-relief structures or gratings [4] are often implemented on top of the cap layer to tailor modal or polarization properties. From the *electrical standpoint*, the VCSEL is a forward-biased *p-i-n* junction. The intrinsic region contains multiple quantum wells MQWs of AlGaAs with a reduced aluminum concentration, resulting in a lower bandgap energy. Under typical operating conditions, holes are injected from the *p*-side (top) and electrons from the *n*-side (bottom). These carriers relax into the quantum wells, leading to carrier accumulation and enabling the

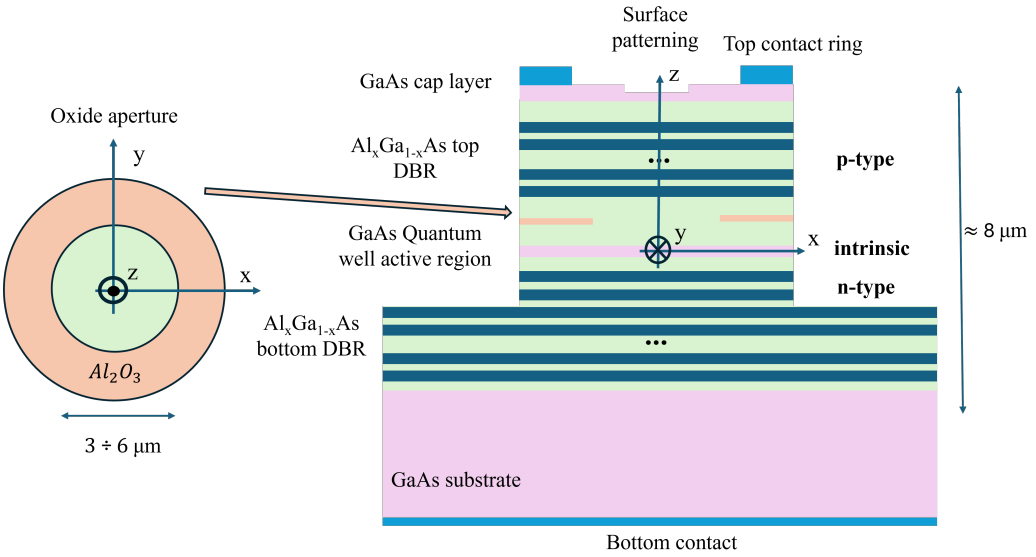

Figure 1.1: Sketch of the cross section of the refractive index of a typical VCSEL (right), and top view of the oxide aperture (left), together with device typical dimensions.

onset of population inversion. In this regime, the MQWs act as an optically amplifying medium.

Under steady-state operation, the optical gain provided by the quantum wells balances the optical losses, thereby sustaining stable light emission. This condition is commonly referred to as the *lasing* or *threshold* condition. Optical losses arise from two primary mechanisms: photon escape through the finite reflectivity of the DBRs (mirror losses) and absorption within the material (intrinsic losses).

Such a dielectric structure supports discrete resonant frequencies, each of which constitutes a distinct optical *mode* characterized by a specific electromagnetic field topography. Because of material anisotropies within the cavity, each mode is typically found in two almost degenerate orthogonally polarized states.

In some application domains discussed in the next section, the device must operate in a single-mode (SM) regime, meaning that the emitted beam is formed of only one transverse mode. In other contexts, the VCSEL typically operates in a multimode (MM) regime, where the output consists of a superposition of multiple modes supported by the cavity.

1.1 VCSEL applications, market, and future developments

Thanks to their low-cost and scalable manufacturing process, compact footprint, and compatibility with array integration, VCSELs have become the leading light sources across numerous technological fields. According to market analyses reported by Fortune [5], the main application domains include:

- data communication (datacom) for short-reach optical links,
- 3D sensing for smartphone facial recognition,
- LiDAR systems for autonomous driving and security,
- industrial heating and laser printing,
- infrared illumination,
- additional applications (e.g., optical mice, gas sensors, quantum gyroscopes).

The report also highlights that datacom VCSELs constitute the largest share of the manufactured devices, whereas overall market growth is increasingly driven by automotive applications. To meet the specific requirements imposed by these diverse application spaces, the conventional circular VCSEL geometry shown in Fig. 1.1 has been extensively modified in both structure and material composition. An overview of these application areas therefore provides useful insight into current front-line VCSEL research.

VCSELs have recently gained particular relevance in LiDAR systems, enabled by their low-cost manufacturability and ease of integration into dense arrays [6]. For such systems, light sources must provide high peak optical power to detect distant targets, operate in the nanosecond pulse regime, and exhibit low beam divergence together with high slope efficiency (*i.e.*, optical power–to–current conversion efficiency). Multi-junction (MJ) VCSELs address these requirements by stacking multiple active regions connected through tunnel junctions, enabling carrier recycling and thereby boosting slope efficiency and output power [7, 8]. This architecture has demonstrated power-conversion efficiencies exceeding 70% [9, 6] and high-power single-mode operation, with continuous-wave output powers up to 14 mW at 940 nm [10]. The main trade-offs of the multi-junction approach are the increased operating voltage and more demanding thermal management, though the latter is mitigated under nanosecond pulsed operation. Moreover, as the number of junctions increases, the presence of multiple oxide apertures and enhanced optical

confinement may lead to higher beam divergence or to excitation of higher-order transverse modes [6, 7].

VCSEL-based quantum sensors, including atomic clocks, magnetometers, and quantum gyroscopes [11–22], require single-mode, high-power emission. Increasing the oxide aperture improves the maximum output power but rapidly leads to multimode (MM) behavior. Surface-relief engineering offers a partial solution by introducing modal-selective reflectivity in the top DBR. For example, [23] reports a high-power single-mode rectangular-aperture VCSEL employing complex surface patterning that simultaneously achieves modal and polarization selection while collimating the output into a circular fiber.

In many quantum-sensing schemes, VCSELs are used to drive atomic transitions between spin states, whose energy splitting matches the photon energy. Angular-momentum selection rules therefore require circularly polarized excitation. This is typically achieved by combining a linearly polarized VCSEL with a quarter-wave plate. Linear polarization can be enforced using the grating-relief (GR) technique [4], which provides both modal and polarization control. However, this approach requires a bulky external component and precise alignment, undermining the intrinsic compactness advantages of VCSELs. For this reason, extensive research is being devoted to realizing monolithic circularly polarized emitters through chiral cavity materials [24], chiral dielectric patterning [25–29], or interacting rotated gratings [30, 31].

SM operation is also essential for coherent applications relying on the monochromatic nature of light, such as optical coherence tomography [32], Doppler interferometry [33], and a wide range of spectroscopic and sensing techniques. In these scenarios, an even more stringent specification is required: the laser must exhibit a stable emission frequency with low linewidth (or low phase noise), which directly determines the coherence length of the emitted beam.

In contrast, MM operation is desirable for heating and laser-printing applications. Breaking the symmetry of a large-area oxide aperture has been shown to produce rich multimode behavior and high output power [34]. MM emission is also valuable in neuromorphic-computing architectures [35, 36], where complex nonlinear transverse-mode dynamics are exploited for spatial reservoir computing.

Material systems used in VCSELs have likewise evolved beyond the conventional AlGaAs alloy to access new wavelength regimes. GaN-based materials are under investigation for UV–green emission [37, 38], while GaSb-based platforms target the far-infrared [39]. In these systems, current confinement is typically achieved using a tunnel junction rather than oxidation, due to the difficulty of forming stable oxide apertures [40]. For datacom

applications, InGaAs quantum wells have been introduced to enhance the differential gain of the active region [41].

A large fraction of VCSEL production is driven by optical-fiber datacom [42–45]. A fundamental distinction in optical communication is the link length. In long-haul systems (several kilometers), the laser must provide high output power to compensate for fiber attenuation and low frequency chirp to mitigate chromatic dispersion. Despite considerable progress, VCSELs currently cannot satisfy the required performance. As a result, long-range systems typically rely on external modulation of a high-power single-mode CW laser.

Short-reach links, in contrast, relax these constraints and enable low-cost direct modulation, where the data stream is encoded directly into the injection current of a high-speed VCSEL without resorting to external modulators. Examples include automotive networks, inter-chip communication, and, most prominently, intra-datacenter links. For such applications, an effective datacom VCSEL must combine high modulation bandwidth, low noise, and low power consumption to mitigate critical self-heating.

Traditional bandwidth-enhancement techniques include minimizing carrier-transport delays, improving thermal management, optimizing carrier and optical confinement, engineering the photon lifetime and the active-region material [46–49]. Although effective, these approaches face fundamental trade-offs and limitations [50], discussed in Sec. 2. Current state-of-the-art VCSELs exhibit small-signal modulation bandwidths around 40 GHz [51, 52], enabling transmission rates up to 200 Gbps when combined with advanced modulation schemes [53–56].

To overcome this limit, several unconventional architectures are being explored, including integrated electro-optic modulators [57], spin-injected VCSELs [58], and transverse coupled-cavity (TCC) VCSELs [59–62]. The latter exploit the coupled resonances of laterally arranged cavities to enhance modulation bandwidth via the photon–photon resonance (PPR) mechanism [63]. Further details on TCC-VCSELs are provided in the next section.

1.2 TCC-VCSELs and motivation for this thesis

Fig. 1.2 illustrates a sketch of some typical TCC-VCSELs geometries. These devices employ a standard epitaxial structure but incorporate oxide apertures that differ substantially from the conventional circular design shown in panel (a). Panel (b) shows a configuration composed of two laterally connected circular apertures, commonly referred to as a bow-tie or two-aperture VCSEL. The geometry in panel (c) features a central aperture connected to multiple elongated lateral cavities, manufactured in [62].

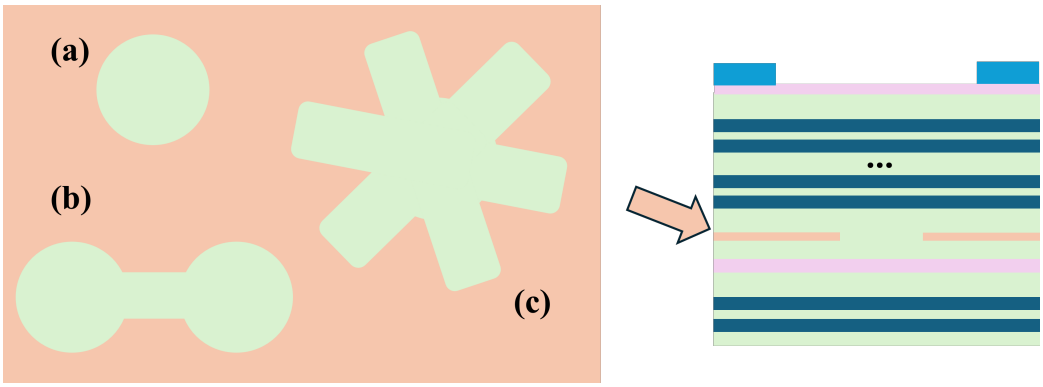

Figure 1.2: Left: sketches of the oxide apertures of (a) a circular standard VCSEL, (b) a two-aperture (bow-tie) VCSEL, and (c) a multi TCC-VCSEL. Right: the standard epitaxial structure typically implied in TCC-VCSELs.

Such geometries have become a major focus in VCSEL research because they offer attractive functionalities, including high modulation speed, beam steering, and terahertz generation, while also introducing significant challenges and trade-offs.

The first demonstration of a TCC-VCSEL was reported in [64], where a two-contact bow-tie device was realized. In that design, each aperture is individually biased and electrically isolated by ion implantation. The modulation scheme biases both apertures at a static operating point while applying RF modulation to only one of them; emission is collected from a single aperture. Using this approach, the authors showed a modulation bandwidth three times larger than that of an equivalent circular VCSEL.

This improvement was modeled by using a feedback mechanism originally described in [65] for edge-emitting lasers. According to this interpretation, a portion of the optical field leaks from the actively driven cavity (the one receiving the larger bias current) into the second cavity, propagates there with a certain group velocity, and eventually couples back, thereby enhancing the modulation response. For the feedback to be effective, the secondary cavity must exhibit a transverse group velocity much smaller than that of free space (i.e., *slow-light* propagation).

Feedback-based models describe external reflections in edge emitters as the sum of multiple optical paths. Under the weak-feedback approximation, the Lang–Kobayashi model [65] retains only the dominant contribution of the first reflection. For TCC-VCSELs, the weak-feedback assumption was removed in [66], where a multiple-reflection model was introduced. This idea was later extended to multi TCC-VCSELs, featuring oxide geometries like that in Fig. 1.2(c), in [60].

Although such reflection-based models qualitatively reproduce the observed bandwidth enhancements, they rely on phenomenological parameters that are difficult to extract from electromagnetic simulations or experimental measurements. For instance, the *coupling strength* between cavities, well defined in edge emitters, is rather ambiguous in transversely coupled geometries. Likewise, the assumption of slow-light propagation is not straightforward to justify within a modal description. Additional parameters, such as the effective transverse cavity length, critically affect the predictions but cannot be directly deduced. Furthermore, temperature effects, believed to play a key role in photon–photon resonance (PPR) experiments, are typically neglected. Device-specific considerations, such as the asymmetric pumping and probing schemes employed in [64], also remain difficult to interpret within such a framework.

Other examples of TCC-VCSELs have been demonstrated using photonic-crystal structures [59, 61, 67–69]. Here, the two apertures are again individually pumped and isolated via proton bombarding. Several studies (*e.g.* [61]) show that such devices may operate either in a *decoupled* regime, in which each cavity emits at a distinct wavelength, or in a *coherent* regime, in which both cavities lase at the same wavelength. The coherent regime is typically observed when the injected currents in both cavities are similar. In this regime, beam steering [70] and excellent modulation bandwidths [59] have been reported. Such ultrabroadband operation has been tentatively described exploiting rate equations under external optical injection [59]. Subsequently, coupled-mode theory [70] was employed to explain the formation of supermodes and beam steering, incorporating concepts from parity–time symmetry and exceptional points [71]. More recently, a complex waveguide model was introduced [72]. These works offer a detailed characterization of near fields, optical spectra, steering properties, and dynamic behavior.

Another bow-tie VCSEL design was recently proposed in [73, 74], featuring an oxide-defined bow-tie aperture biased through a single central contact. In [74], temporal measurements of the emissions from the two apertures revealed antiphase beating oscillations. In [75], we demonstrated that coherent emission can be achieved under single-contact operation by increasing the input current, and observed a modest bandwidth enhancement. A detailed comparison with modeling was presented, including spectrally and spatially resolved near-field measurements, optical spectra, time-domain traces, and frequency responses. In [76], the wavelength difference between the two cavities was converted directly into an RF signal, an operation that conventionally requires two independent lasers, thus eliminating the need for thermal or current synchronization.

Despite substantial progress, existing models still rely heavily on phenomenological descriptions, making it difficult to develop predictive design tools capable of starting from

a target geometry and accurately forecasting the resulting device performance. Moreover, present approaches lack a self-consistent treatment of the coupled carrier and optical field dynamics, an essential ingredient behind phenomena such as PPR [63] and frequency-dependent stability effects reported in [77–79].

The objective of this thesis is to obtain, starting from the scalar wave equation, a comprehensive set of coupled equations capable of reproducing the wide range of physical phenomena observed in TCC-VCSELs, and to relate key device-level characteristics to the underlying geometry. The resulting model is then used to interpret recent experimental results. The remainder of this thesis is organized as follows:

- **Chapter 2** reviews high-speed VCSEL design strategies and their corresponding modeling.
- **Chapter 3** discusses the weakly guiding approximation in VCSELs, enabling scalar modeling of device dynamics.
- **Chapter 4** begins with the scalar wave equation, whose domain of validity is discussed in Chapter 3, and derives a complete, ready-to-use set of governing equations for the dynamics of the transverse modes of a VCSEL.
- **Chapter 5** applies the developed model to the bow-tie device, first in the ideal symmetric case and then including asymmetries and thermal effects, and compares the results with experimental observations.
- **Chapter 6** develops a lumped model and analyzes its behavior under the perfectly symmetric approximation, providing a closed-form expression for PPR dynamics and a stability analysis revealing frequency-dependent modal competition.

Chapter 2

High-speed VCSELs modelling

This section provides a review of the main optimization strategies applied to datacom devices and supports the findings of the literature with the corresponding simulation modeling. VCSELs are commonly studied by means of a rate-equations model [1, 3, 80], consisting of two ordinary differential equations, which read, neglecting the spontaneous emission:

$$\begin{aligned} \frac{\mathrm{d}S}{\mathrm{d}t} &= \left(\Gamma v_{\mathrm{g}} g - L\right) S, \\ \frac{\mathrm{d}N}{\mathrm{d}t} &= -\frac{N}{\tau} - v_{\mathrm{g}}\, g(N)\, S + \frac{\eta I}{\mathrm{q} V_{\mathrm{act}}}. \end{aligned} \tag{2.1}$$

Here, S is the photon density, N is the carrier density in the active region, τ is the carrier lifetime in the quantum well, v_{g} is the group velocity in the quantum well, V_{act} is the volume of the active region, *i.e.,* the volume of the region where the optical gain takes place, q is the charge of the electron, $g(N)$ is the carrier-dependent material gain, Γ is the confinement factor, *i.e.,* a coefficient that accounts for the effective overlap of the mode with the active region, and L are the modal losses and η is the injection efficiency. The latter quantity is the sum of the mirror losses α_{m}, which arise due to the openness of the cavity, and the intrinsic losses α_{i}, which arise due to material absorption, and are usually reported as its reciprocal, defined as the photon lifetime τ_{p}:

$$L = \alpha_{\mathrm{m}} + \alpha_{\mathrm{i}} = \frac{1}{\tau_{\mathrm{p}}}. \tag{2.2}$$

In order to find analytical solutions of (2.1), a linear form of the gain is usually adopted:

$$g(N) = \frac{G_{\mathrm{d}}(N - N_{\mathrm{tr}})}{1 + \varepsilon S}. \tag{2.3}$$

where G_d is the differential gain, N_tr is the transparency carrier density, and ε is the spectral hole-burning factor. The threshold carrier density can be defined as the value of N for which the lasing condition is met ($g - L = 0$), which, within this approximation, reads:

$$N_\mathrm{th} = \frac{L}{G_\mathrm{d}\Gamma v_\mathrm{g}} + N_\mathrm{tr} = \frac{G_\mathrm{th}}{G_\mathrm{d}} + N_\mathrm{tr}, \qquad G_\mathrm{th} \triangleq \frac{L}{\Gamma v_\mathrm{g}}, \tag{2.4}$$

where G_th is defined as the threshold gain and represents the value of the gain provided from the active region to compensate the threshold losses. Consequently, the threshold current is defined as the value that provides N_th for $S = 0$ and $\frac{\mathrm{d}}{\mathrm{d}t} = 0$:

$$I_\mathrm{th} = \frac{\mathrm{q} V_\mathrm{act} N_\mathrm{th}}{\eta\,\tau}. \tag{2.5}$$

The steady-state solution of (2.1) reads, neglecting ε:

$$N = N_\mathrm{th}, \qquad S = \eta\,\frac{\tau_\mathrm{p}}{V_\mathrm{opt}}\,\frac{I - I_\mathrm{th}}{\mathrm{q}} \quad \text{for} \quad I > I_\mathrm{th}, \qquad S = 0 \quad \text{for} \quad I < I_\mathrm{th}, \tag{2.6}$$

where the optical volume V_opt is defined as $V_\mathrm{act}/\Gamma_\mathrm{z}$. The photon density is then converted into an output power:

$$P = \frac{E_\mathrm{ph}}{\mathrm{q}}\,\underbrace{\frac{\alpha_\mathrm{m}}{\alpha_\mathrm{m} + \alpha_\mathrm{i}}}_{\triangleq\,\eta_0}(I - I_\mathrm{th}) \quad \text{for} \quad I > I_\mathrm{th}, \qquad P = 0 \quad \text{for} \quad I < I_\mathrm{th}. \tag{2.7}$$

Here, E_ph is the photon energy, η_0 is referred to as the outcoupling efficiency and tends to 1 (ideal slope) for increasing mirror losses.

To evaluate the dynamic performance of the device, a small-signal analysis is usually carried out. This consists of superimposing a small time-varying current on top of the bias one, leading to small sinusoidal changes of the unknowns:

$$I(t) = I_0 + \tilde{I}(t) \;\Rightarrow\; N(t) = N_0 + \tilde{N}(t), \quad S(t) = S_0 + \tilde{S} \tag{2.8}$$

where the quantities denoted with subscript 0 are the static ones. The nonlinear system (2.1) can therefore be turned into a linear one by Taylor expansion. Finally, assuming harmonic excitations of the form $\mathrm{e}^{\mathrm{i}\omega t}$, and consequently $\frac{\mathrm{d}}{\mathrm{d}t} = \mathrm{i}\omega$, a complex linear system is obtained, whose solution, varying the value of ω, provides the frequency response of the VCSEL for the quantities of interest S and N. The latter consists of a second-order response, whose

resonant frequency is found by [3]:

$$f_{\mathrm{r}} \approx D\sqrt{I - I_{\mathrm{th}}}, \quad \text{with:} \quad D = \frac{1}{2\pi}\sqrt{\frac{\eta\Gamma v_{\mathrm{g}}}{\mathrm{q}V_{\mathrm{act}}}G_{\mathrm{d}}}. \tag{2.9}$$

or expressed as a function of the photon density:

$$f_{\mathrm{r}} \approx \frac{1}{2\pi}\sqrt{\frac{v_{\mathrm{g}}G_{\mathrm{d}}}{\tau_{\mathrm{p}}}S}. \tag{2.10}$$

The damping factor is given by:

$$\gamma \approx Kf_{\mathrm{r}}^2, \quad \text{with:} \quad K = 4\pi^2\left(\tau_{\mathrm{p}} + \frac{\varepsilon}{v_{\mathrm{g}}G_{\mathrm{d}}}\right). \tag{2.11}$$

As a figure of merit, $f_{3\mathrm{dB}}$, *i.e.,* the frequency at which the transfer function falls by $-3\,\mathrm{dB}$ with respect to its value at $f = 0$, is usually reported. Its value is linked to the quantities defined so far by the useful approximation, valid for low currents:

$$f_{3\mathrm{dB}} \approx 1.55\, f_{\mathrm{r}}, \qquad \left(\frac{\gamma}{\omega_{\mathrm{r}}} \ll 1\right), \tag{2.12}$$

while it is expected to saturate at high currents roughly at:

$$f_{3\mathrm{dB,max}} \approx \frac{2\pi\sqrt{2}}{K}. \tag{2.13}$$

From inspection of (2.9), it can be observed that large bandwidth can be reached at low bias current by high differential gain, high optical confinement, and small active volume, ultimately resulting in a low-power high-speed optical source. The first factor depends on the choice of the active material [41]. The second one can be optimized by careful electromagnetic design, while the third is constrained by technological feasibility. In principle, the active volume could be reduced by shrinking the oxide aperture. However, this approach is difficult to control and typically leads to poor device yield. A promising alternative is the use of lithographically defined apertures [81], which offer significantly improved fabrication precision.

2.1 Thermal limitations

The formulas derived so far suggest that the modulation speed can be enhanced by increasing the injected current. However, this concept holds true until self-heating produces a saturation effect. In [48], a fit of the K and D parameters is performed, from which a maximum intrinsic bandwidth of roughly 60 GHz is inferred. Experimental observations, however, show a saturation at roughly 30 GHz. These observations suggest that thermal effects are essential limitations, which should be included in high-speed VCSEL modeling. In doing so, at least the interplay of three elements should be considered: a temperature increase, assumed as $\Delta T = k_{\text{th}} I$, k_{th} being a phenomenological factor, a thermally dependent expression for the material gain [1, 82], and a non-ideal description of the active region. In this example, the material library of [83], which is a function of the wavelength, holes, electrons, and temperature, will be used. For the active region description, a phenomenological injection-efficiency term is introduced to account for the limited carrier density that the quantum well can support:

$$\eta(N) = \frac{1}{1 + \mathrm{e}^{(N-N_2)/N_0}}. \tag{2.14}$$

where N_2 is the maximum carrier density, used as fitting parameter, and N_0 is a phenomenological coefficient set to $N_0 = 10^{24}\,\mathrm{m}^{-3}$. Fig. 2.1 (left) shows the simulated output power versus the current (LI-characteristics) obtained with the ideal model (2.1) compared to the one obtained by including the described non-ideal effects. In the first case, the power has a linear trend above threshold (2.7), while in the second case it is constrained by the characteristic roll-off behavior.

The intensity modulation response (IMR) can be computed by evaluating the fast Fourier transform (FFT) of the impulse response of the photon density. Fig. 2.1 (right) shows the -3 dB frequency as a function of the square root of the current. It can be seen that the linear trend predicted in (2.9) is found for low currents. For high currents, instead, the thermal effects limit the bandwidth. The simulated results are in qualitative agreement with the reported experiments [48].

Thermal limitations arise from the temperature dependence of the quantum-well gain, which exhibits a peak at a specific wavelength. As temperature increases, the gain peak shifts and progressively detunes from the cavity's resonant wavelength [1]. Consequently, the threshold carrier density increases until it approaches the maximum allowed carrier density N_2. Beyond this point, further increases in current can no longer compensate for the growing threshold carrier density, causing the photon density to decrease. The consequent saturation in the photon density ultimately leads to reduced damping and

a reduction of the resonance frequency, as described in (2.10). This problem could be partially mitigated through careful thermal design of the laser and by introducing an appropriate detuning offset [83], which compensates for the temperature-induced shift of the gain peak. Nevertheless, additional temperature-dependent mechanisms, not included in this example, such as the increase in intrinsic optical losses, are still expected to arise.

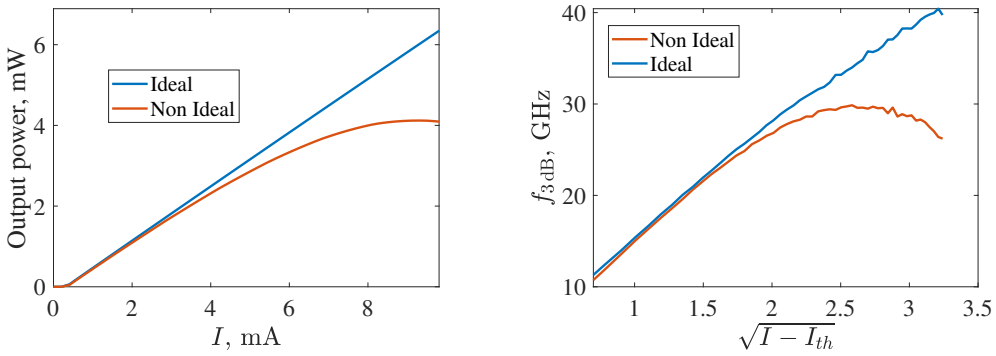

Figure 2.1: *LI*-characteristics (left) and $f_{3\mathrm{dB}}$ (right), obtained with the ideal rate-equation model (blue) and by assuming self-heating, temperature-dependent gain, and non-ideal capture behaviour (2.14).

2.2 Photon lifetime engineering

Eq. (2.12) suggests that the reduction of the photon lifetime, or equivalently the increase of the threshold gain, results in an enhanced maximum $f_{3\mathrm{dB}}$. Again, this is only true for ideal linear gain and neglected self-heating. Experimental observations show indeed the existence of an optimum value: reducing it beyond this point results in degraded dynamical performance [47]. Fig. 2.2a shows the simulated *LI*-characteristics for varying photon lifetime, with the top left inset highlighting the threshold region. The effect is twofold: first, the threshold current is higher for lower photon lifetime, as described in Eq. (2.5). Second, the slope efficiency increases, in agreement with (2.7). Fig. 2.2b shows the maximum $f_{3\mathrm{dB}}$ for each threshold gain, calculated with the ideal model (blue) and including the thermal effects (red). For low threshold-gain values (corresponding to long photon lifetimes), the bandwidth is intrinsically limited by the K-factor in both ideal and non-ideal models, as described by (2.12). As the photon lifetime is reduced, the 3 dB bandwidth initially increases, reaches a maximum, and then drops sharply for the non-ideal model, while it increases for the ideal one. This decline cannot be captured by

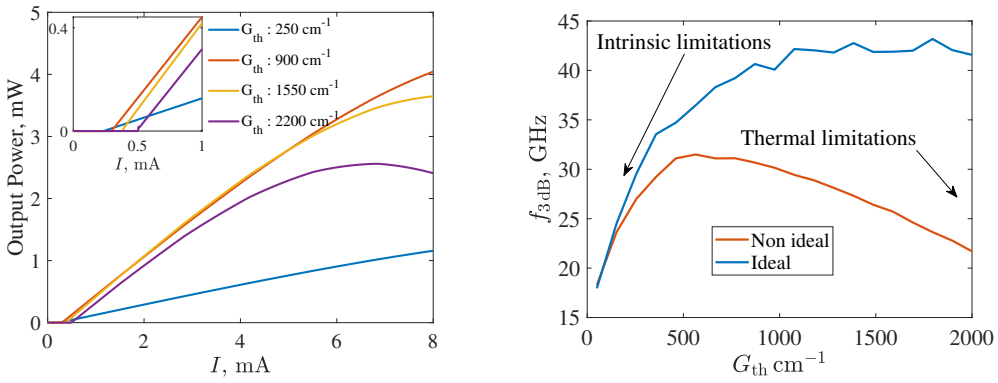

(a) (b)

Figure 2.2: Left: *LI*-characteristics for varying threshold gain. Right: max $f_{3\text{dB}}$ as a function of G_{th}, computed with accounted thermal effects (red) or with the ideal model (2.1) (blue).

simple analytical expressions, as it originates from an interplay of gain and temperature. These modeling results are in qualitative agreement with the experiments reported in the literature [46, 47].

2.3 Carrier transport delays beyond circuital models

In addition to the intrinsic limitations described so far, the high-speed performance of the device is also limited by carrier transport delays. These effects are usually included in the rate-equation model (2.1) by multiplying the transfer function of the VCSEL with a parasitic response:

$$H(\omega) = H_{\text{p}}(\omega)H_{\text{i}}(\omega). \tag{2.15}$$

where $H(\omega)$ is the total response, $H_{\text{i}}(\omega)$ is the intrinsic response computed with the small-signal analysis described in the previous sections, and $H_{\text{p}}(\omega)$ is the parasitic response, the latter usually inferred by means of a lumped circuital model [84].

To go beyond this phenomenological approach, a much more complex model is needed [83, 49], which consists of solving the drift-diffusion model governing the transport of carriers in semiconductor devices, coupled to the photon rate equation and the quantum

well capture problem:

$$-\nabla^2\phi = \frac{\mathrm{q}}{\varepsilon}\Big(p^{3\mathrm{D}} - n^{3\mathrm{D}} + p^{2\mathrm{D}} - n^{2\mathrm{D}} + N_{\mathrm{D}}^{+} - N_{\mathrm{A}}^{-}\Big), \tag{2.16}$$

$$\frac{\partial n^{3\mathrm{D}}}{\partial t} = \frac{1}{\mathrm{q}}\nabla\cdot\mathbf{J}_{\mathrm{n}}^{3\mathrm{D}} - U_{\mathrm{n}}^{3\mathrm{D}}, \tag{2.17}$$

$$\frac{\partial p^{3\mathrm{D}}}{\partial t} = -\frac{1}{\mathrm{q}}\nabla\cdot\mathbf{J}_{\mathrm{p}}^{3\mathrm{D}} - U_{\mathrm{p}}^{3\mathrm{D}}, \tag{2.18}$$

$$\frac{\partial n^{2\mathrm{D}}}{\partial t} = \frac{1}{\mathrm{q}}\nabla\cdot\mathbf{J}_{\mathrm{n}}^{2\mathrm{D}} - U_{\mathrm{n}}^{2\mathrm{D}}, \tag{2.19}$$

$$\frac{\partial p^{2\mathrm{D}}}{\partial t} = -\frac{1}{\mathrm{q}}\nabla\cdot\mathbf{J}_{\mathrm{p}}^{2\mathrm{D}} - U_{\mathrm{p}}^{2\mathrm{D}}, \tag{2.20}$$

$$\frac{\partial S_q}{\partial t} = \Gamma_{\mathrm{z}}\big(g_q - L_q\big)S_q, \qquad q = 1,\ldots,N_{\mathrm{modes}}, \tag{2.21}$$

where n and p are electrons and holes, respectively, ϕ is the electrostatic potential, $J_{\mathrm{n,p}}$ are the electron and hole current, whose expressions are reported in [83], $U_{\mathrm{n,p}}$ are the generation rates, ε is the dielectric constant, and the subscript q labels the modes. In this model, the carriers are divided into bulk, labeled with the superscript 3D, and confined ones, *i.e.,* captured in the quantum well, labeled with the superscript 2D. The 2D and 3D populations are linked by capture rates $C_{\mathrm{cap,n,p}}$, embedded into the recombination terms $U_{\mathrm{n,p}}$. The active quantum-well current I_{qw} can therefore be defined as the integral of the capture rate converted into a current, restricting the integral to the oxide region, where the modal envelope is different from zero:

$$I_{\mathrm{qw,np}} = \mathrm{q}\iiint_{\text{ox. aperture}} C_{\mathrm{cap,np}}\,\mathrm{d}V. \tag{2.22}$$

where $C_{\mathrm{cap,np}}$ is the spatial distribution of the capture rate. Since the only carrier population that contributes to the modal gain is the confined one, $I_{\mathrm{qw,np}}$ is the quantity that must be considered in the lumped rate equation as injected current I in (2.1). Equations (2.16)–(2.21) are discretized by means of finite element methods and transformed into a nonlinear system, whose general form is:

$$\partial_{\mathrm{t}}\underline{u} = f(\underline{u}) + \underline{t}. \tag{2.23}$$

where $\underline{u}$ is the vector of the discretized unknowns, f is a function depending on the discretization technique, and t is the forcing term, related to the injected current. Further details on the discretization are found in [83]. If a perturbative time-harmonic contribution

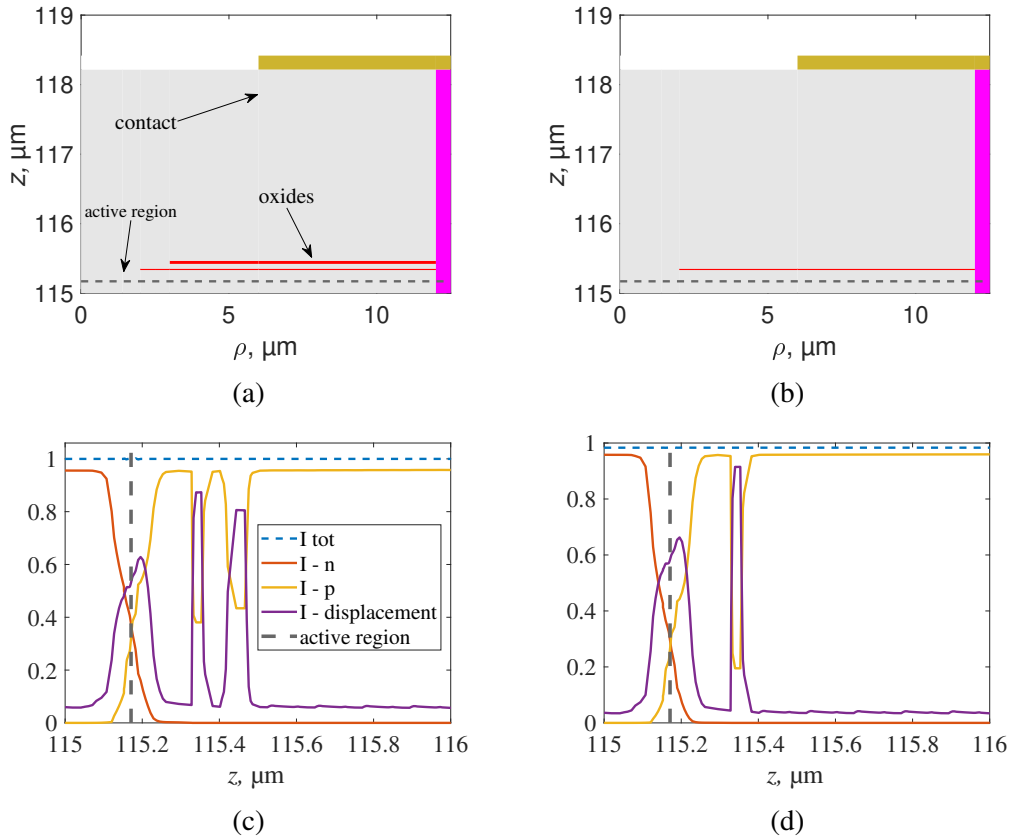

Figure 2.3: Top: sketch of the VCSEL under investigations, with a single (a) and double (b) oxide aperture. Bottom: integral of the current density contributions as defined in (2.27) as a function of z for the single (c) and double (d) oxide aperture, at a modulation frequency of 25 GHz.

$\tilde{t}e^{i\omega t}$ is added to the static value of the forcing term t, a small-signal analysis of (2.23) provides:

$$\tilde{u}(\omega) = (i\omega \underline{\underline{I}} - \underline{\underline{J}})^{-1}\tilde{t}, \tag{2.24}$$

where the tilde refers to the time-harmonic variations with respect to the static value and J is the Jacobian matrix of the function f. The transfer function can be computed, based on (2.22), as:

$$H(\omega) = \frac{P(\omega)}{I(\omega)} = \underbrace{\frac{P(\omega)}{I_{\mathrm{qw}}(\omega)}}_{H_{\mathrm{i}}} \underbrace{\frac{I_{\mathrm{qw}}(\omega)}{I(\omega)}}_{H_{\mathrm{p}}}. \tag{2.25}$$

In order to give a spatial visualization of the parasitic sources that give rise to $H_{\mathrm{p}}(\omega)$, (2.20) + (2.18) - (2.19) - (2.17) is considered. Taking the time derivative of (2.16), and after some algebraic substitutions, the usual time-varying divergence condition on the current is obtained:

$$\nabla \cdot \Big(\underbrace{\partial_t \varepsilon E}_{\triangleq J_{\mathrm{d}}} + J_{\mathrm{n}} + J_{\mathrm{p}} \Big) = 0. \tag{2.26}$$

where $U_{\mathrm{n}} = U_{\mathrm{p}}$ and $E = -\nabla\phi$ have been used. The quantity J_{d} is normally referred to as displacement current. Let z be defined as the epitaxial direction, *i.e.,* the direction perpendicular to wafer surface, as in Fig. 1.1. By taking the volume integral of (2.26) on a large enough cylindrical volume, and applying Gauss theorem, one obtains:

$$I_{\mathrm{contact}}(t) = \iint_S J_{\mathrm{d},z}(z,t) + J_{\mathrm{n},z}(z,t) + J_{\mathrm{p},z}(z,t)\,\mathrm{d}x\,\mathrm{d}y. \tag{2.27}$$

where S denotes a surface at an arbitrary z coordinate, denoted by a versor on $\hat{z}$ direction. This expression highlights an important physical interpretation. Firstly, the total current flowing through the structure is conserved at every z. The particle current $(J_{\mathrm{n}} + J_{\mathrm{p}})$ does not necessarily equal the externally measured terminal current at every section inside the device, the difference being supplied by the displacement current. In other words, charge storage within the device, which gives rise to J_{d}, allows the displacement current to "substitute" for the conduction current locally, in the same way of a shunt capacitor. Equation (2.27) therefore represents a distributed equivalent of a parallel configuration of a capacitive branch (the displacement current) and conductive branches (the electron and hole currents).

This modeling strategy is applied to a toy example of oxide-capacitance reduction: the multi-oxide VCSEL architecture [85]. Figures 2.3a and 2.3b illustrate the two simulated device geometries: on the left, a conventional VCSEL with a single oxide layer, and on the right, a modified structure that incorporates a secondary, thicker oxide. The aperture of this additional oxide is large enough to avoid perturbing the fundamental mode. Figs. 2.3c and 2.3d show the integral on the transverse plane of each contribution as a function of z, computed at $f = 25\,\mathrm{GHz}$. As described in Eq. (2.27), the sum of the contributions is constant. The displacement current component exhibits a peak at the oxide(s) locations, which indicates that, under high-frequency operation, a large fraction of the current is given by displacement current through the oxide. Fig. 2.4 shows the normalized profile of the z component of the displacement and total currents at the active region, together with the sketch of the fundamental mode for the case of single and double oxide. It can be seen that in the single oxide the current profile is more *spread* outside the oxide aperture

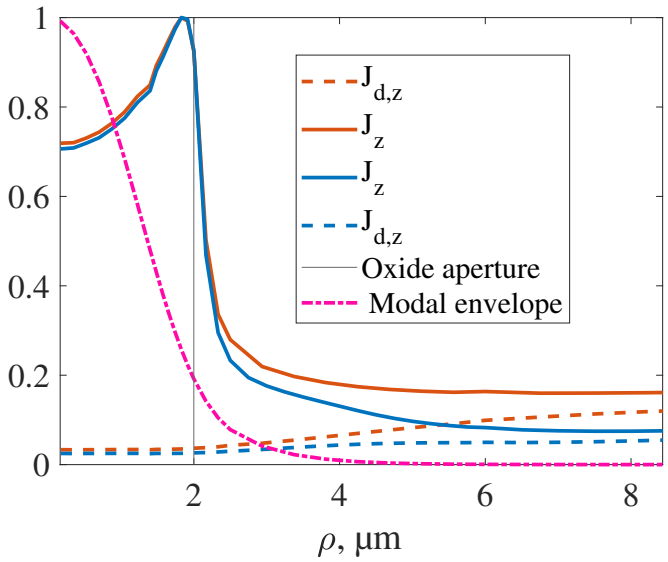

Figure 2.4: Plot of the z component of the normalized profiles of total current (solid), displacement current (dotted) for the single (red) and double (blue) oxide. The black vertical line denotes the oxide aperture, while the magenta curve is the plot of the intensity distribution of the fundamental mode.

due to the poor high-frequency oxide carrier confinement effect. Fig. 2.5 shows the partial contributions and the total response, as defined in (2.25) for both devices. It can be seen that the single oxide device is severely limited by the parasitic response. The addition of the second oxide takes the parasitic response from roughly 8 GHz to 15 GHz, confirming the multi-oxide bandwidth improvement. Further optimizations of this concept rely on placing more oxide layers, which however requires a careful design and alignment with the nodes of the optical standing wave, in order to not interfere with the optical mode, which goes beyond the scope of this work. Finally, it has to be remarked that such approach naturally handles any capture delay [86], arising from the interplay of transport and capture problems. The specific reported example does not include the pad capacitance, as it is excluded from the simulation box.

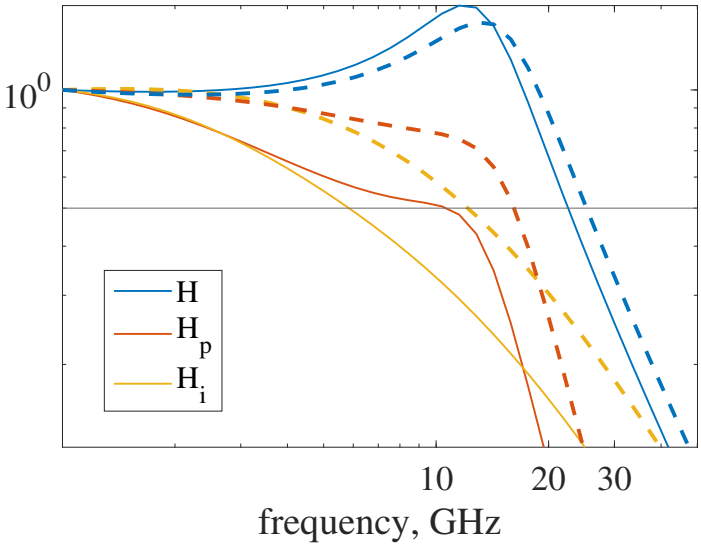

Figure 2.5: IMR response for the single oxide (solid) and double oxide (dashed). In particular, the yellow curve represents H_{p}, the red curve represents H, and the blue curve represents H_{i}, as defined in (2.25).

Chapter 3

The scalar approximation in VCSELs

This section reviews the scalar approximation of Maxwell's equations, which reduces the full vectorial electromagnetic problem to a simpler scalar formulation. This approximation has been adopted in several laser modeling studies [77, 87, 88] under conditions in which the vectorial nature of the optical field does not play a dominant role.

In VCSELs, the optical cavity is realized as a stratified dielectric structure, in which lateral confinement is typically provided by a single transversely varying layer. This concept underlies effective-index models [89], which map the vertical cavity structure onto an equivalent dielectric waveguide. Because the oxide aperture occupies only a fraction of the full epitaxial stack (see Fig. 1.1), VCSELs can be regarded as weakly guiding waveguides.

These considerations motivate a preliminary investigation of an equivalent dielectric waveguide in order to review the weakly guiding approximation. The considered waveguide consists of a core with refractive index $n_{\text{core}} = n_1$ embedded in a cladding with refractive index $n_{\text{clad}} = n_2$. Its transverse cross section has a bow-tie aperture geometry, as illustrated in Fig. 3.1. The aperture is formed of two circular regions of radii R_{l} and R_{r}, whose center-to-center separation is denoted by L_{br}, and by a central connecting region referred to as the *bridge*, with thickness t_{br}. The refractive index profile is assumed to be invariant along the propagation direction z.

In the general procedure described in [90], the six components of the electric and magnetic fields are expressed in terms of the two longitudinal unknowns H_{z} and E_{z}. Within each homogeneous region of the core and cladding, where the material parameters are constant, these longitudinal components satisfy a scalar wave equation that follows directly from Maxwell's equations in a uniform medium. The transverse field components are then obtained from E_{z} and H_{z} through the corresponding constitutive relations. However,

the continuity of the transverse field components at material interfaces must still be enforced explicitly. Imposing these continuity conditions generally requires fully vectorial modal solutions, *i.e.,* modes in which all six field components contribute and vary across the transverse plane, aside from a few special cases. In other words, in a piecewise-homogeneous waveguide, the *coupling* among field components that enforces the vectorial character of the modes arises exclusively from the boundary conditions at the dielectric interfaces.

When the refractive index jump is small, *i.e.,* $n_1 \approx n_2$, a great simplification is possible. Maxwell's equations in the frequency domain at frequency ω are considered, assuming a refractive index that depends only on the transverse coordinates x and y:

$$\nabla \times \mathbf{E} = \mathrm{i}\,\omega\,\mu_0\,\mathbf{H}, \qquad \nabla \times \mathbf{H} = -\,\mathrm{i}\,\omega\,\varepsilon(x,y)\,\mathbf{E}. \tag{3.1}$$

In standard waveguide theory [90, 91], the solutions that propagate in the longitudinal z direction are found:

$$\underline{E}_i(x,y,z,\omega) = \underline{E}_i(x,y,\omega)\,\mathrm{e}^{\mathrm{i}\beta_i(\omega)z}, \qquad \beta \triangleq \frac{\omega}{\mathrm{c}}\,n_{\mathrm{eff}}, \tag{3.2}$$

where $\mathbf{E}_i(x,y,\omega)$ is the transverse mode, $\beta(\omega)$ is the propagation constant, and n_{eff} is the

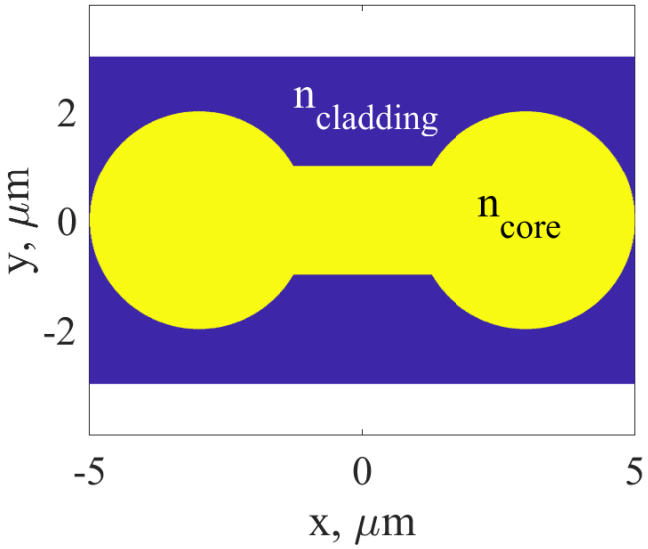

Figure 3.1: Sketch of the considered waveguide

effective index. The guided mode features an n_{eff} between the cladding and core refractive

indices, which in the low-contrast approximation means:

$$n_{\text{eff}} \approx n_{\text{core}} \approx n_{\text{clad}}, \tag{3.3}$$

from which one can approximate:

$$\beta \approx \frac{\omega}{\mathrm{c}} n_{\text{core}} \rightarrow k_{\mathrm{t}} \triangleq \sqrt{\beta^2 - \frac{\omega^2}{\mathrm{c}^2}\varepsilon} \approx 0. \tag{3.4}$$

The transverse component of the fields for each mode is related to the longitudinal ones by [90]:

$$\mathbf{E}_{\mathrm{t}} = \frac{\mathrm{i}}{k_{\mathrm{t}}^2}\left[\beta \nabla_{\mathrm{t}} E_{\mathrm{z}} + \omega\mu\, \hat{z} \times \nabla_{\mathrm{t}} H_{\mathrm{z}}\right], \tag{3.5}$$

$$\mathbf{H}_{\mathrm{t}} = \frac{\mathrm{i}}{k_{\mathrm{t}}^2}\left[\beta \nabla_{\mathrm{t}} H_{\mathrm{z}} - \omega\varepsilon\, \hat{z} \times \nabla_{\mathrm{t}} E_{\mathrm{z}}\right]. \tag{3.6}$$

Assuming for the i-th mode $\nabla_{\mathrm{t}} \approx \mathrm{i}k_{\mathrm{t},i}$ [91], it can be seen that the ratio between the transverse and longitudinal components scales as β/k_{t}, tending to infinity in low-contrast regimes. For this reason, in order to have finite transverse components, the longitudinal one must be zero. The solution of the full set of Maxwell's equations can be obtained by reducing the problem to the scalar wave equation for an arbitrary component of the transverse electric field:

$$\nabla_{\mathrm{t}}^2 E_i + \frac{\omega^2}{\mathrm{c}^2} n^2 E_i = \beta^2 E_i. \tag{3.7}$$

Since the field E is assumed to be continuous and differentiable, explicit enforcement of boundary conditions is not required. This follows from the quasi-homogeneity of the material system, see Eq. (3.3), which ensures that the scalar formulation automatically satisfies the appropriate continuity relations.

It is important to note that the unknown E may represent *any* transverse field component: the specific polarization orientation is not important, and the light is treated as a scalar. The corresponding modes are commonly referred to as "linearly polarized" (LP) modes, as they exhibit a single dominant transverse field component.

Fig. 3.2a shows n_{eff} versus λ, usually referred to as dispersion curves, computed with a full-wave optical waveguide solver, denoted with markers, for the first four guided modes compared with the curves obtained by solving the scalar Helmholtz equation (3.7) with a finite element modelling (FEM) method, denoted with solid lines. The comparison is performed in two cases: in panel (a) a weakly constrast waveguide, with $n_1 = 1.61$ and $n_2 = 1.6$, and in panel (b) a high-contrast case, with $n_1 = 1.8$ and $n_2 = 1.6$. The modes

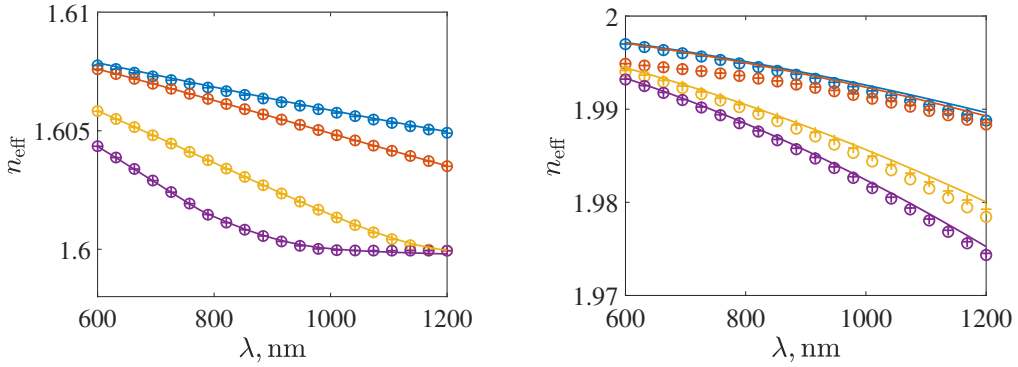

Figure 3.2: n_{eff} as a function of wavelength for the considered waveguide in small (a) and large (b) refractive index jump.

of the full-wave solver are divided into two classes: those denoted with a circle feature a dominant component along the x direction, while those denoted with "+" have a dominant y component. It can be seen that, in the weakly guiding case (a), excellent agreement between the scalar theory and the full-wave analysis is found. Furthermore, the x and y dominant modes are degenerate, meaning that the vector orientation of the light is not important. In the high-contrast case, the scalar method does not approximate well the full-wave solutions, and, in general, the x and y modes are not degenerate.

The standard weakly guiding approximation is typically formulated for dielectric waveguides with slowly varying transverse refractive-index profiles. More recent studies [92–95] have extended the analysis of vertical-cavity surface-emitting lasers (VCSELs) through the adoption of exact coupled-modes formulations. This approach, described in detail in [96], leverages the fact that a VCSEL is composed of a large number of layers stacked along the longitudinal z direction, with only a limited subset exhibiting transverse $\varepsilon(x,y)$ inhomogeneities, (see Fig. 1.1). This structural property enables an optimized numerical strategy in which the global resonance problem is constructed by considering z as a propagation direction, and cascading the individual transmission matrices associated with each layer. The transmission matrix for each layer is represented on a vectorial cylindrical-wave basis defined in a homogeneous reference medium of relative permittivity ε_{r} [90].

The basis elements are labeled by the order in the azimuthal direction m, a label l that determines the choice of angular functions, sine or cosine, a label that determines the polarization, TE or TM, the transverse wavenumber k_{tr}, and a label s that determines the

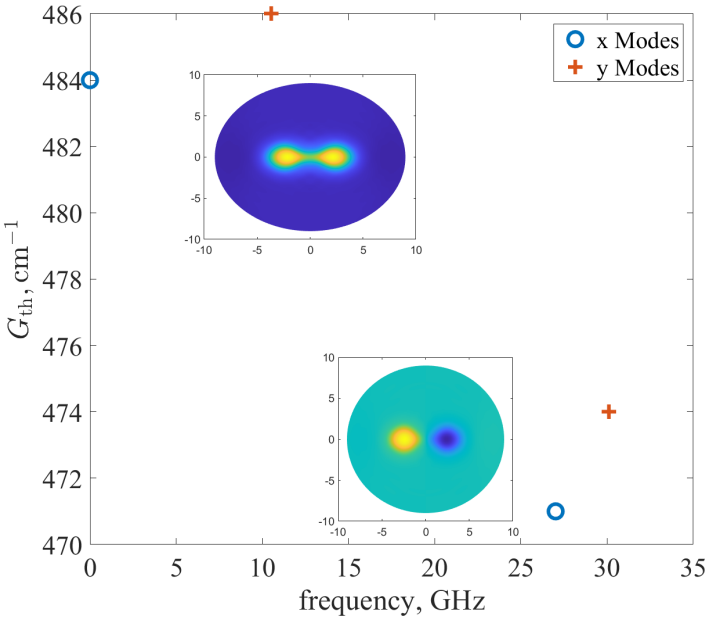

Figure 3.3: First two supported modes for the investigated bow-tie geometry, for x and y polarizations and for neglected electro-optic anisotropy.

forward or backward propagation. Within this framework, [92] derives a scalar approximation by assuming a distribution of small k_{tr}, yielding simplified coupled-mode equations, in analogy with Eq. (3.4).

Figure (3.3) shows the first two transverse modes of a bow-tie VCSEL with geometric parameters $L_{br} = 5\,\mu m$, $t_{br} = 1.2\,\mu m$, and $R_{r,l} = 1.5\,\mu m$, based on a standard epitaxial structure [97]. As in the waveguide case, the modes are classified according to whether the dominant electric field component is oriented along the x or y axis.

Under this assumption, the computed x- and y-polarized modes are nearly degenerate, with a frequency separation, birefringence, of only a few GHz. This value is negligible compared with the modal spacing of a circular oxide aperture, but it is comparable to the separation between the first two transverse modes in a bow-tie geometry. The electro-optic anisotropy introduces a further birefringence on the order of tens of GHz [31].

The key point is that the obtained modes remain essentially LP, so that each one can be assumed as governed by an independent scalar wave equation for the x and y components. Spin-flip model (SFM) [98, 99], treats this condition as a two sets of equation for the time evolution of x and y modes, whose dynamics is coupled only by gain anisotropy induced by an imbalance of spin-up and spin-down populations in the active region. This imbalance

can be obtained by spin-polarized pumping [100], which lies outside the scope of this work, or can be self-induced by dynamical instability, leading to polarization switches [101].

In the context of this work however, the phenomena of interest, such as photon–photon resonance and transverse mode locking, are not expected as a result of the interaction between x- and y-polarized modes. The vectorial treatment of the SFM is thus omitted, and the scalar wave equation (SWE) is adopted as the starting point for the analysis of the device dynamics. This choice prevents the observation of polarization related dynamical instabilities, [102], which might be present in the device under investigation. In particular, Eq. (3.7) is considered by transforming $-\beta^2 = \partial_z^2$, and $-\omega_0^2 = \partial_t^2$. Furthermore, the effect of the electron-hole injection is accounted for by a material polarization term at the right-hand side of the SWE [87].

Within this approximation, polarization switching and other secondary polarization-related effects cannot be captured. In datacom VCSELs however, polarization suppression is commonly achieved using a surface grating relief [4, 103, 104]. In such devices, the grating selects a single linear polarization, allowing the field to be described by a SWE for that single component. This further supports the scalar approximation as a reasonable basis for the present study.

Chapter 4

Multimode rate equation

In this section a ready-to-use set of equations for the investigation of the multimode dynamics in VCSELs is derived.

As discussed in the previous section, the inhomogeneous SWE, which governs the time evolution of the LP modes, is considered, where the unknown field $\mathscr{E}$ represents the dominant transverse component of the electric field:

$$\nabla^2 \mathscr{E}(\boldsymbol{r},t) - \frac{\varepsilon_\mathrm{r}(\boldsymbol{r})}{\mathrm{c}^2}\,\partial_t^2 \mathscr{E}(\boldsymbol{r},t) = \frac{1}{\varepsilon_0 \mathrm{c}^2}\,\partial_t^2 \mathscr{P}(\boldsymbol{r},t), \tag{4.1}$$

where $\varepsilon_\mathrm{r}(\boldsymbol{r})$ is the refractive-index distribution of the unpumped VCSEL and $\mathscr{P}$ denotes the material polarization induced by the optical response of the active region, ultimately related to electron–hole pair injection.

A slowly varying envelope phasor transformation is applied, in which the field amplitude is a complex, time-dependent quantity. The electric field is written as

$$\mathscr{E}(\boldsymbol{r},t) = \Re\left[E_\mathrm{s}(\boldsymbol{r},t)\, e^{\mathrm{i}\omega_0 t}\right], \tag{4.2}$$

where ω_0 is an arbitrary carrier frequency and E_s is a slowly varying complex envelope.

Under this transformation, the temporal derivative becomes $\partial_t \to \mathrm{i}\omega_0 + \partial_t$ due to the chain rule:

$$\partial_t \mathscr{E} = \Re\left[(\mathrm{i}\omega_0 + \partial_t) E_\mathrm{s}(\boldsymbol{r},t)\, e^{\mathrm{i}\omega_0 t}\right]. \tag{4.3}$$

The polarization is assumed to depend linearly on the electric field through the electric susceptibility χ. Since the envelope dynamics are slow compared to the optical oscillation, the field effectively probes the material response at ω_0. In the phasor domain, the

polarization can therefore be approximated as:

$$\mathscr{P} \rightarrow \varepsilon_0 \chi(\omega_0) E_\mathrm{s}(\boldsymbol{r},t). \tag{4.4}$$

To relate the optical response to carrier dynamics, the susceptibility is expressed in terms of the material gain [87]:

$$\chi = \mathrm{i}\, n \frac{g(N)}{k_0}, \tag{4.5}$$

where n is the refractive index and $g(N)$ is the carrier-density-dependent gain and $k_0 = \frac{\omega_0}{c}$. Typically in lasers, light–matter interaction is described by the semiclassical Maxwell–Bloch equations, involving coupled dynamics for the polarization and carrier population [105]. Due to the fast polarization relaxation in semiconductors, the polarization dynamics can be adiabatically eliminated, justifying the simplified treatment.

Applying the phasor transformation to the scalar wave equation yields:

$$-\frac{\varepsilon_\mathrm{r}}{\mathrm{c}^2}\,\partial_t^2 \mathscr{E} \rightarrow -\frac{\varepsilon_\mathrm{r}}{\mathrm{c}^2}\left[(\mathrm{i}\omega_0)^2 E_\mathrm{s} + 2\,\mathrm{i}\omega_0 \dot{E}_\mathrm{s} + \ddot{E}_\mathrm{s}\right], \tag{4.6}$$

$$\nabla^2 \mathscr{E} \rightarrow \nabla^2 E_\mathrm{s}(\boldsymbol{r},t), \tag{4.7}$$

while the polarization term becomes:

$$\frac{1}{\varepsilon_0 \mathrm{c}^2}\,\partial_t^2 \mathscr{P} \rightarrow \frac{\mathrm{i}\, n\, g(N)}{\omega_0 \mathrm{c}}\left[(\mathrm{i}\omega_0)^2 E_\mathrm{s} + 2\,\mathrm{i}\omega_0 \dot{E}_\mathrm{s} + \ddot{E}_\mathrm{s}\right], \tag{4.8}$$

where the dotted symbols denote the time derivative. The electric field envelope is expanded as a sum of the lasing modes:

$$E_\mathrm{s}(\boldsymbol{r},t) = \sum_i \phi_i(\boldsymbol{r}) E_i(t). \tag{4.9}$$

To leverage the modal expansion, the principle of operation of the optical solver has to be recalled. The latter finds that a stable time-harmonic mode exists provided that a specific gain distribution is applied within the quantum-well region. The i-th electromagnetic mode is described by:

$$\phi_i(\boldsymbol{r}) \cos(\omega_i t) = \Re\left(\phi_i(\mathbf{r}) e^{\mathrm{i}\omega_i t}\right), \tag{4.10}$$

where ϕ_i is the spatial modal profile and ω_i is the emission frequency. In representing the i-th mode in the frequency domain, the reference frequency of Eq. (4.2) has been set arbitrarily to $\omega_0 = \omega_i$, in such a way that the envelope E_s is steady (*i.e.,* $E_\mathrm{s} = 1$). The

equation for the i-th mode can be therefore written by combining (4.6),(4.7),(4.8):

$$\nabla^2\phi_i - (\mathrm{i}\omega_i)^2\frac{\varepsilon_\mathrm{r}}{\mathrm{c}^2}\phi_i = -\mathrm{i}nk_0 g_{\mathrm{th},i}(\boldsymbol{r})\phi_i, \tag{4.11}$$

where $g_{\mathrm{th},i}$ is the spatial gain distribution sustaining the i-th mode, and $k_0 = \frac{\omega_0}{\mathrm{c}}$. Assuming that ω_i lies close to ω_0, a first-order expansion gives:

$$(\mathrm{i}\omega_i)^2 \simeq (\mathrm{i}\omega_0)^2 - 2\omega_0\Delta\omega_i, \qquad \Delta\omega_i = \omega_i - \omega_0. \tag{4.12}$$

The term of Eq. (4.7), accounting for the modal expansion (4.9) and for the approximation of Eq. (4.12), becomes:

$$\begin{aligned}\nabla^2 E_\mathrm{s}(\boldsymbol{r},t) = \sum_i \nabla^2 E_i\phi_i(\mathbf{r}) &= \frac{\varepsilon_\mathrm{r}}{\mathrm{c}^2}\sum_i E_i\phi_i(\mathbf{r})\left[(\mathrm{i}\omega_i^2) - \mathrm{i}nk_0 g_\mathrm{th}(\mathbf{r})\right] \\ &\approx \frac{\varepsilon_\mathrm{r}}{\mathrm{c}^2}\sum_i E_i\phi_i(\mathbf{r})\left[(\mathrm{i}\omega_0^2) - 2\omega_0\Delta\omega_i - \mathrm{i}nk_0 g_{\mathrm{th},i}(\mathbf{r})\right].\end{aligned} \tag{4.13}$$

Combining Eqs. (4.6)–(4.8), using Eq. (4.13) yields:

$$\begin{aligned}-\frac{\varepsilon_r}{\mathrm{c}^2}\sum_i \phi_i\left[2\omega_0\Delta\omega_i E_i + 2\mathrm{i}\omega_0\dot{E}_i + \ddot{E}_i\right] = \sum_i \phi_i\frac{\mathrm{i}ng(N)}{\omega_0\mathrm{c}}\left[(\mathrm{i}\omega_0)^2 E_i + 2\mathrm{i}\omega_0\dot{E}_i + \ddot{E}_i\right] \\ -\sum_i \phi_i E_i\,\mathrm{i}nk_0\,g_{\mathrm{th},i}(\boldsymbol{r}).\end{aligned} \tag{4.14}$$

Under the slowly varying envelope approximation (SVEA):

$$|\dot{E}_i| \ll \omega_0|E_i|, \qquad |\ddot{E}_i| \ll \omega_0|\dot{E}_i|, \tag{4.15}$$

only the first-order terms in ω_0 are retained, yielding:

$$\varepsilon\sum_i \phi_i\left[-\mathrm{i}\Delta\omega_i E_i + \dot{E}_i\right] = \frac{n\mathrm{c}}{2}\left[\sum_i \phi_i E_i\, g(N) - \sum_i \phi_i E_i\, g_{\mathrm{th},i}(\boldsymbol{r})\right]. \tag{4.16}$$

The power orthogonality, which is true only in closed cavities, is assumed *i.e.,*:

$$\iiint \varepsilon_r\phi_i\phi_j^*\,\mathrm{d}r = \delta_{ij}, \tag{4.17}$$

where integration domain is restricted to the VCSEL volume. Such a choice could seem arbitrary and therefore is justified in Sec. 4.2. Assuming separability of the eigenmodes:

$$\phi_i(\boldsymbol{r}) = \Psi_i(x,y)\,b(z), \tag{4.18}$$

where z denotes the direction perpendicular to the wafer surface, and $n \simeq n(z)$, the orthogonality relation becomes:

$$\int n(z)^2 |b(z)|^2 \,\mathrm{d}z \iint \Psi_i \Psi_j \,\mathrm{d}x\,\mathrm{d}y = \delta_{ij}. \tag{4.19}$$

By multiplying (4.16) by ϕ_j^* and integrating yields, accounting the modal orthogonality (4.17):

$$\dot{E}_j = \mathrm{i}\Delta\omega_j E_j + \frac{\mathrm{c}}{2}\sum_i E_i \iiint \phi_i(\mathbf{r})\phi_j(\mathbf{r})^* n g(\mathbf{r})\,\mathrm{d}r - \frac{\mathrm{c}}{2}\sum_i E_i \iiint \phi_j(\mathbf{r})^* \phi_i(\mathbf{r}) n g_{\mathrm{th},i}(\mathbf{r})\,\mathrm{d}r. \tag{4.20}$$

Since the gain is confined to the quantum wells:

$$g_{\mathrm{th}}(\boldsymbol{r}) = p(z) G_{\mathrm{th}}, \qquad g(\boldsymbol{r}) = p(z) g(x,y), \tag{4.21}$$

where $p(z)$ is a port function different from zero only at the active region, the second integral at the RHS becomes:

$$\begin{aligned} -\frac{c}{2}\sum_i \iiint \phi_j^*(\boldsymbol{r})\,\phi_i(\boldsymbol{r})\,E_i\,n\,g_{\mathrm{th},i}(\boldsymbol{r})\,\mathrm{d}r = \\ -\frac{G_{\mathrm{th}}}{n_a}\frac{\mathrm{c}}{2}\sum_i \underbrace{\int_{\mathrm{qw}} n_a^2 |b(z)|^2 \,\mathrm{d}z}_{\triangleq \Gamma_z} \underbrace{\iint \Psi_j^* \Psi_i \,\mathrm{d}x\,\mathrm{d}y}_{=\delta_{ij}} E_i = -L_j \frac{E_j}{2\tau_{\mathrm{p}}}. \end{aligned} \tag{4.22}$$

where the modal losses L_j are defined as:

$$L_j = \frac{1}{2\tau_{\mathrm{p}}} \triangleq \Gamma_{\mathrm{z}} v_{\mathrm{g}} G_{\mathrm{th,j}} \tag{4.23}$$

The first integral on the right-hand side yields an analogous expression:

$$\begin{aligned} \frac{c}{2}\sum_i E_i \iiint \phi_i(\boldsymbol{r})\,\phi_j^*(\boldsymbol{r})\,n\,g(\boldsymbol{r})\,\mathrm{d}r &= \frac{\Gamma_z v_{\mathrm{g}}}{2}\sum_i E_i \iint \Psi_i \Psi_j^*\, g(N)\,\mathrm{d}x\,\mathrm{d}y \\ &= \sum_i k_{ij} E_i. \end{aligned} \tag{4.24}$$

The coupling terms k_{ij} arise from spatial distribution of the gain on the transverse plane:

$$k_{ij} = \frac{v_{\mathrm{g}}\Gamma_{\mathrm{z}}}{2} \iint \Psi_j^* \Psi_i g(x,y)\,\mathrm{d}x\mathrm{d}y. \tag{4.25}$$

Also variations on the refractive index profile δn, due to self-heating or variation from the nominal structures can be accounted by an equivalent gain [106]:

$$g = g(N) - \mathrm{i}k_0\delta n \tag{4.26}$$

The dynamical equations finally read:

$$\partial_t E_i = \left(\mathrm{i}\Delta\omega_i - \frac{1}{2\tau_{\mathrm{p,i}}}\right) E_i + \sum_{j=1}^{N_{\mathrm{m}}} k_{ij} E_j \tag{4.27}$$

4.1 Carriers diffusion equation

To complete the set of equations (4.27), the evaluation of the carrier distribution in the active region as a function of time is needed. For this reason, the carrier diffusion equation, corrected with the stimulated recombination term, is considered [107]:

$$\partial_t N(x,y) = -N/\tau - v_{\mathrm{g}}\Re(g)S(x,y) + D_{\mathrm{n}}\nabla^2 N + \frac{J(x,y)}{qW} \tag{4.28}$$

where D_{n} is the diffusivity, J is the current density injection profile in the active region, W is the width of the active region, τ_{n} is the carriers lifetime, S is the photon density:

$$S = |\sum_i E_i \Psi_i|^2. \tag{4.29}$$

The carrier diffusion equation is solved by means of a finite-element method (FEM), self-consistently with the electric field equations, on a mesh generated with the software *gmsh* [108]. An evaluation of the carrier diffusion allows the simultaneous investigation of multi-mode dynamics and modal competition accounting for the spatial hole burning.

4.2 Modal normalization and orthogonality

To get a set of equations for the i-th mode, Eq. (4.16) has been multiplied by Ψ_j^* and integrated. This crucial operation, usually referred to as *projection* on the j-th mode, requires an orthogonality relation in order to retrieve a diagonal system for the unperturbed ($k_{ij} = 0$) system of equation. However, the orthogonality condition of Eq. (4.17) is, in general, not guaranteed in open cavities. This section revisits this aspect using a simplified one-dimensional SWE. Starting from (4.11) for the i-th and j-th modes, and taking the

complex conjugate of the equation for the j-th mode, one obtains

$$\frac{\mathrm{d}^2\phi_i}{\mathrm{d}z^2} + \omega_i^2 \frac{\varepsilon_r(z)}{\mathrm{c}^2}\,\phi_i(z) = -\mathrm{i}\,n\,k_0\,g_{\mathrm{th},i}(z)\,\phi_i(z), \tag{4.30}$$

$$\frac{\mathrm{d}^2\phi_j^*}{\mathrm{d}z^2} + \omega_j^2 \frac{\varepsilon_r(z)}{\mathrm{c}^2}\,\phi_j^*(z) = \mathrm{i}\,n\,k_0\,g_{\mathrm{th},j}(z)\,\phi_j^*(z). \tag{4.31}$$

Multiplying the first equation by $\phi_j^*(z)$ and the second by $\phi_i(z)$, subtracting the resulting expressions, and integrating over the cavity region, denoted by the interval $[z_1, z_2]$, Green's identity yields:

$$\begin{aligned}\frac{\omega_i^2 - \omega_j^2}{\mathrm{c}^2}\int_{z_1}^{z_2} \varepsilon_r(z)\,\phi_i(z)\phi_j^*(z)\,\mathrm{d}z = \mathrm{i}\,n\,k_0\,(g_{\mathrm{th},i} + g_{\mathrm{th},j})\int_{z_1}^{z_2} g_0(z)\,\phi_i(z)\phi_j^*(z)\,\mathrm{d}z \\ - \int_{z_1}^{z_2}\left(\phi_j^*(z)\frac{\mathrm{d}\phi_i(z)}{\mathrm{d}z} - \phi_i(z)\frac{\mathrm{d}\phi_j^*(z)}{\mathrm{d}z}\right)\mathrm{d}z.\end{aligned} \tag{4.32}$$

The two terms on the right-hand side of Eq. (4.32) arise from the open nature of the cavity. In particular, the boundary term, upon setting $\frac{\mathrm{d}}{\mathrm{d}z} = \mathrm{i}k$, is proportional to an output power, whereas the volume integral is associated with the power generated in the active region to sustain optical gain. In the case of a closed cavity, both contributions vanish. Consequently, modal power orthogonality strictly holds only for closed cavities, and lasing modes in open systems cannot, in general, be used as an orthogonal basis.

In the specific case considered here, namely an oxide-defined VCSEL, the transverse lasing modes can be reasonably treated as orthogonal, allowing the desired orthogonality relation to hold. This is not a general property of VCSEL resonators, but rather an empirical assumption that applies to the particular geometry under investigation.

Another problem in evaluating the integral in (4.22), is the infinite support of the lasing modes, which do not decay outside the cavity. In this work, as a reasonable approximation the integration box is restricted to the VCSEL region. This choice, which might seem arbitrary, finds a justification in quasi-normal modes theory [109–113] which provides a *regularization* of the modal normalization by including boundary contributions:

$$\int_{-R}^{R} n^2(z)\,\Psi_i^2(z)\,\mathrm{d}z + \frac{\mathrm{i}\,\mathrm{c}}{2\omega_m}\left[n(z)\,\Psi_i^2(z)\right]_{-R}^{R} = N_0 = 1. \tag{4.33}$$

Equation (4.33) is independent of the truncation boundary R, provided that R lies within a homogeneous region outside the cavity. Notably, no complex conjugation appears, implying that the confinement factor can, in general, be complex. In VCSELs, however, the conjugation in (4.22) has no practical effect, since the electric field within the active

region can be assumed real. Moreover, the boundary contributions in (4.33) are negligible due to the high reflectivity of the distributed Bragg reflectors.

For these reasons, this work adopts a *quasi-closed* cavity approximation. Under this assumption, modal confinement and orthogonality are treated as in a closed cavity, despite the intrinsically open nature of the VCSEL. While this approximation is adequate for the phenomena investigated in this work, it is expected that a more general treatment will be required for strongly open cavities or for VCSEL geometries with unconventional or highly asymmetric shapes, where the transverse mode orthogonality cannot be assumed, which will be the subject of future investigation.

4.3 The incoherent approximation for large frequency separation

Eqs. (4.27) are considered with two modes ($N_\mathrm{m} = 2$), featuring a large frequency spacing $\Delta\omega$. The following solution is assumed:

$$E_2 = E_{2,0}e^{\mathrm{i}\Delta\omega t}, \qquad E_1 = E_{1,0}, \tag{4.34}$$

meaning that both modes are lasing and that $k_{ii} = L_i$. The stimulated emission term in the carrier equations reads:

$$v_\mathrm{g}g(N)S = -v_\mathrm{g}g(N)[|E_{1,0}\Psi_1|^2 + |E_{2,0}\Psi_2|^2 + 2\Re(E_1E_2^*\Psi_1\Psi_2e^{\mathrm{i}\Delta\omega})] \tag{4.35}$$

while the electric field equations read:

$$\partial_t E_{1,0} = -L_1E_{1,0} + k_{11}E_{1,0} + k_{12}E_{2,0}e^{\mathrm{i}\Delta\omega t} \tag{4.36}$$

$$\partial_t E_{2,0} = -L_2E_{2,0} + k_{22}E_{2,0} + k_{21}E_{1,0}e^{-\mathrm{i}\Delta\omega t} \tag{4.37}$$

if $\Delta\omega$ is big enough, the oscillating term in (4.35) is cut off from the carrier dynamics. Furthermore, the beating of these modes is not visible in the photodetector bandwidth. The same reasoning holds for the oscillating term of (4.37) (4.36). As a rule of thumb, one can neglect the cross terms if:

$$\frac{k_{ij}}{\Delta\omega_{ij}} \ll 1 \tag{4.38}$$

This means that, if the frequency separation is big enough, one can solve the following simplified system for the modal amplitudes:

$$\partial_t E_{i,0} = (v_g \Gamma_z g_i - L_i) E_{i,0}, \qquad g_i = \frac{1}{2} \iint_{AR} \Psi_i^* \Psi_i g(N) dx dy, \tag{4.39}$$

and compute the photon density *incoherently* as:

$$S = \sum_i |\Psi_i E_{i,0}|^2 \tag{4.40}$$

Equations (4.40),(4.39) represent the textbook rate equations that are normally implied in the investigation of multimode devices [83] when coherent effects are not important.

4.4 Overview of the modelling chain

The dynamical equations used in this work are:

$$E_i' = \Omega_i E_i + \sum_j k_{ij} E_j, \qquad \Omega_i = -L_i + \mathrm{i}\Delta\omega_i, \tag{4.41}$$

$$k_{ij} = k_g + k_{ox} + k_{th}, \tag{4.42}$$

$$k_g = \underbrace{\frac{v_g \Gamma_z}{2} \iint_{AR} \Psi_j^*(x,y)\, g(N)\, \Psi_i(x,y)\, dx dy}_{\text{carrier-induced coupling}}, \tag{4.43}$$

$$k_{ox,th} = -\underbrace{\mathrm{i} v_g \frac{2\pi \Gamma_z'}{\lambda_0} \iint_{AR} \Psi_j^*(x,y) \Psi_i(x,y)\, \delta n_{ox,th}(x,y)\, \mathrm{d}x\, \mathrm{d}y}_{\text{thermal and technological-index perturbations}}, \tag{4.44}$$

$$\partial_t N(x,y) = -\frac{N}{\tau} - v_g \Re\big(g(N)\big) S(x,y) + D_n \nabla^2 N + \frac{J(x,y)}{qW}, \tag{4.45}$$

$$S(x,y) = \left| \sum_i E_i(t)\, \Psi_i(x,y) \right|^2, \tag{4.46}$$

$$\iint_{AR} |\Psi_i(x,y)|^2 dx dy = 1. \tag{4.47}$$

Here, Γ_z' is the longitudinal confinement of a refractive-index perturbation δn. The overall simulation workflow is summarized in Fig. 4.1, and consists of two main stages:

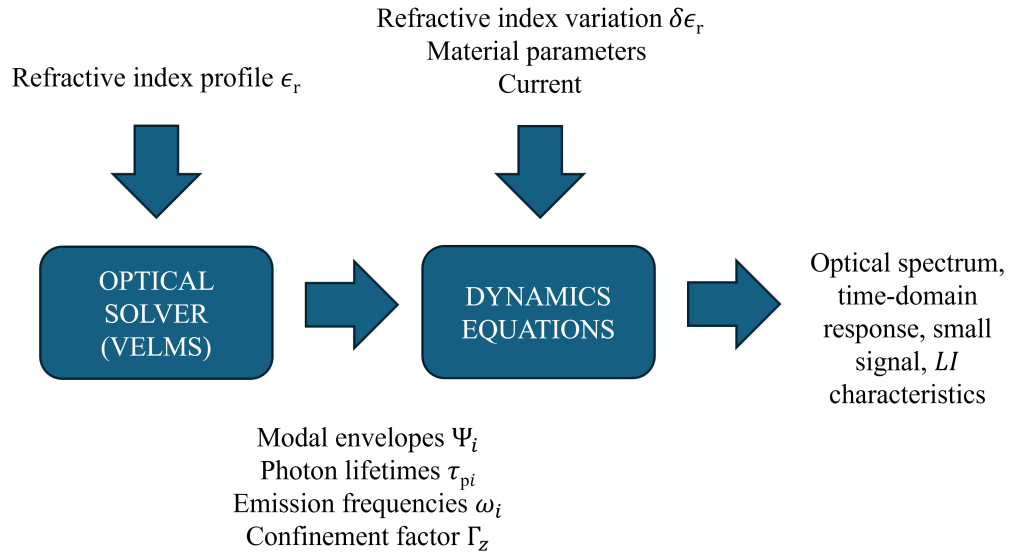

Figure 4.1: Schematic overview of the modelling chain.

- **Optical modal solver:** the device geometry is provided as input to our in-house VCSEL eigenmode solver VELMS [92]. The solver returns the electromagnetic modal envelopes, photon lifetimes, emission frequencies, and confinement factors.

- **Dynamical equations:** the above coupled-mode and carrier-diffusion equations are solved using the modal data, spatial distributions of refractive-index perturbations (thermal or technological), current-injection profiles, and the relevant material parameters.

Equations of this type were previously derived in [114, 115] and used to analyze the formation of supermodes in coupled VCSEL arrays, including cases of asymmetric pumping. These approaches, however, rely on the eigenmodes of isolated cavities as a basis, which requires *inferring* a coupling coefficient. Similarly, [70] presents an experimental and theoretical study of mode hopping and beam steering in a 1×2 photonic-crystal VCSEL array, again using a framework based on diagonalizing an effective coupling matrix.

The present work emphasizes that the modal-coupling terms k_{ij} are, in general, complex, time-dependent quantities that originate from the spatially nonuniform and dynamically evolving gain distribution. Accounting for this dependence naturally incorporates dynamical effects such as PPR and frequency-dependent instabilities, supported by a nonzero imaginary part of the gain, as discussed in [79, 78].

A related modeling framework was introduced by [116] for edge-emitting lasers, in which the cross-coupling coefficients arise from longitudinal gain-field overlap integrals, where carrier evolution is treated by means of a polynomial expansion. An analogous formulation for VCSELs was recently applied in [117, 118] to analyze relative-intensity noise, employing a Gauss-Laguerre modal basis, and in [102] for the investigation of the coupled polarization-multimode dynamics.

In this work, the access to a full electromagnetic modal basis, obtained through the in-house solver VELMs [92], allows the framework to be applied to devices with nonconventional apertures, such as bow-tie geometries.

Furthermore, this work examines the range of validity and intrinsic limitations of the model, such as the quasi-closed cavity approximation, and explores possible extensions, including perturbative terms $k_{\mathrm{ox,th}}$. The results demonstrate that a wide range of experimentally observed phenomena, including PPR, self-heating, technological variations, beam steering, terahertz generation, and modal locking, traditionally treated using disparate modeling approaches, emerge naturally from the same unified set of dynamical equations.

Chapter 5

Bow-tie VCSELs

5.1 Optical modes

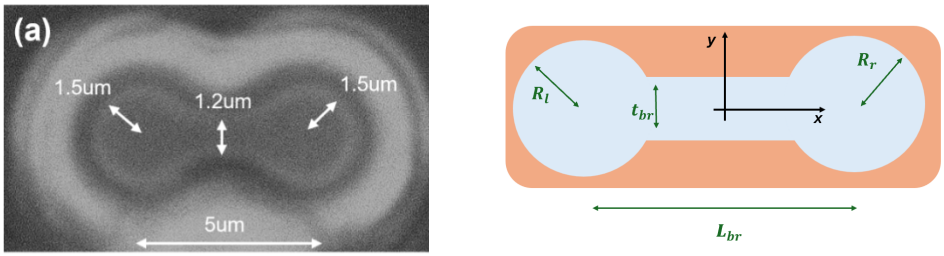

Figure 5.1: Oxide aperture photo and schematic for the considered bow-tie geometry, taken from [75]

The considered oxide aperture is sketched in Fig. 5.1 (right) together with a photograph of a manufactured device [73] (left). The latter consists of two apertures of radii $R_{\mathrm{l,r}}$, connected by a central region referred to as the *bridge*, whose thickness is denoted by t_{br}. The distance between the centers of the two apertures is defined as the bridge length L_{br}.

As a first step in analyzing this nonconventional geometry, the optical modes of the structure are computed. To comply with the dynamical equations, which have been developed in a scalar framework, the modes are computed within the LP approximation [92]. Modes are numbered from lower to higher emission frequency, with the i-th mode featuring $i-1$ zeros along the x direction. In addition, the origin of the transverse axis is fixed at the center of the bow-tie, as indicated in Fig. 5.1.

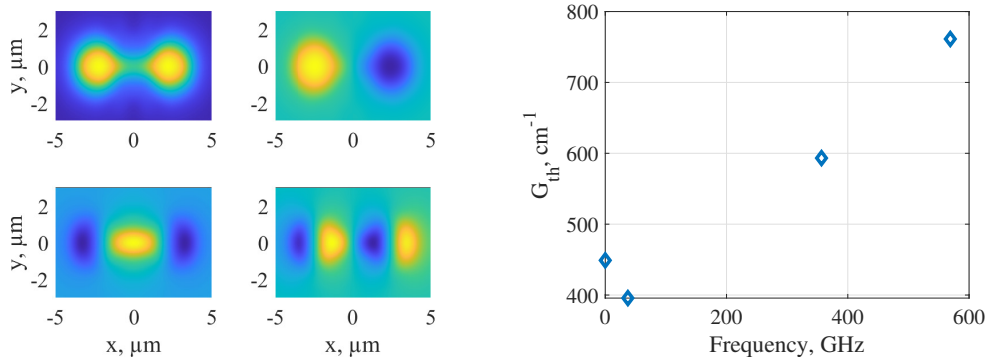

Figure 5.2: Left: modal envelope of the first four modes. Right: representation of the first four modes on the threshold gain–emission frequency plane.

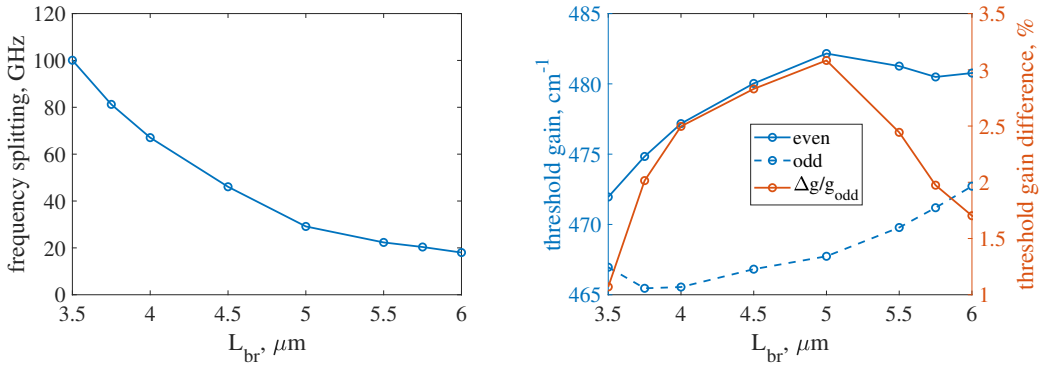

Figure 5.3: Left: frequency splitting as a function of the bridge length. Right: threshold gain separation, taken from [119].

Figure 5.2 (left) shows the envelope of the first four computed optical modes of a perfectly symmetrical bow-tie VCSEL, featuring $R_{l,r} = 1.5\,\mu m$, $L_{br} = 5\,\mu m$, and $t_{br} = 1.2\,\mu m$ and a standard epitaxial structure emitting at 850 nm, reported in [73]. The first two modes are usually referred to as even and odd *supermodes* and are usually derived within a perturbative picture [115, 114]. Figure 5.2 (right) shows the threshold losses versus the emission frequencies, where the first-mode frequency is set to zero. The inspection of this plot reveals the peculiarity of the investigated device, which lies in the presence of almost-degenerate even and odd modes, suggesting strongly coupled dynamics.

The analysis performed in the following sections shows that the relevant modal parameters are the threshold gain separation ΔG and the frequency separation Δf of the even and odd supermodes, which can be controlled by electromagnetic design. The quantity Δf can be varied up to approximately 100 GHz by the bridge length, as shown in Fig. 5.3

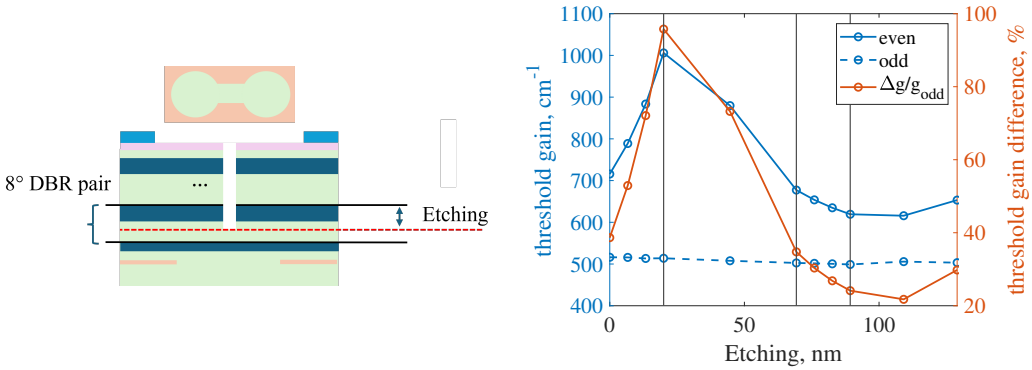

Figure 5.4: Right: threshold gain separation as a function of the etching depth, starting from the beginning of the eighth DBR pair from above, as schematically depicted in the left part of the figure.

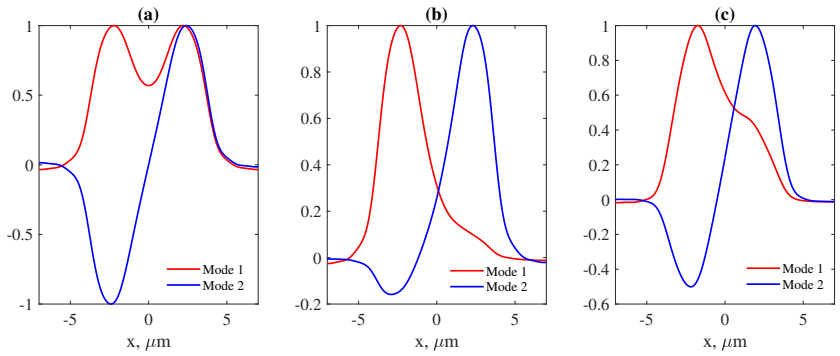

Figure 5.5: Cut of the two first optical modes for a symmetric device (a), an asymmetric device with $R_l = 1.5\,\mu m$ and $R_r = 1.4\,\mu m$ (b), and an asymmetric device with an added thermal profile (c), taken from [75].

(left). This modification has only a minor impact on the threshold gain separation, reported in Fig. 5.3 (right). The threshold gain separation ΔG can instead be increased by etching a trench, which worsens the reflectivity at the center of the device, where only the even mode differs from zero, as shown in Fig. 5.4. For the sake of readability, the threshold-gain separation is reported throughout this work in normalized percentage form, defined as:

$$\Delta g = \frac{G_{th1} - G_{th2}}{G_{th1}} \cdot 100\,(\%). \tag{5.1}$$

In particular, the etching is performed starting from the eighth DBR pair, as sketched in the left part of the figure, enabling values of ΔG up to 100 % without significantly altering Δf.

Based on these electromagnetic simulations, Δf and ΔG are assumed to be independently controllable by design within the ranges reported above.

In a realistic experimental scenario, a slight asymmetry $R_\mathrm{l} \neq R_\mathrm{r}$ must be considered, arising from the poor controllability of the oxidation process. Figure 5.5 (b) shows the even and odd supermodes for $R_\mathrm{l} = 1.4\,\mu\mathrm{m}$ and $R_\mathrm{r} = 1.5\,\mu\mathrm{m}$. Such an asymmetry tends to localize the modal envelopes, with the second mode confined in the smaller cavity, leading to a decoupled operation. The third and fourth modes are not shown because they remain approximately unchanged. Another important effect is self-heating: panel (c) shows the computed modes for the asymmetric bow-tie of panel (b), with an added Gaussian temperature profile. The latter has three main effects: it tends to recover distributed supermodes, it localizes the modes toward the center of the bridge due to thermal lensing, and it increases the frequency separation, as observed in [120]. These results highlight the opposing interplay between temperature and geometrical asymmetries, the former promoting coupled operation and the latter leading to decoupled emission of the two cavities. This behavior will be investigated in more detail in the next section by introducing the coupling terms k_ox and k_th, as defined in Eq. (4.44).

5.2 Perfectly symmetric bow-tie

As a first step, the model derived in the previous section is applied to investigate a perfectly symmetrical device with neglected self-heating effects, *i.e.,* $k_\mathrm{ox} = k_\mathrm{th} = 0$. The simulation is driven to a steady state by a static current whose transverse profile is assumed to coincide with the oxide aperture. The second (odd) mode is assumed to feature a larger photon lifetime. For this reason, the steady-state solution, provided that the threshold gain separation is sufficiently large to ensure stable operation, results in sole lasing of the odd mode, while the amplitude of the even mode is zero. Once the turn-on transient is completed, a current impulse is applied and FFT of the photon density is evaluated to compute the IMR.

Figure 5.6a shows the IMR in three cases. The blue curve represents the IMR obtained by probing the light only at the left cavity and injecting the current impulse only into the left cavity. The black curve represents the IMR response under the same excitation, but with total probing of the emitted light. The dotted yellow curve represents the IMR obtained by probing the left cavity while injecting the current impulse into both cavities. It can be observed that the yellow and black curves correspond to the response of an isolated VCSEL, whereas the blue curve exhibits a photon–photon resonance (PPR) effect that enhances the modulation bandwidth. This example shows that, in order to observe

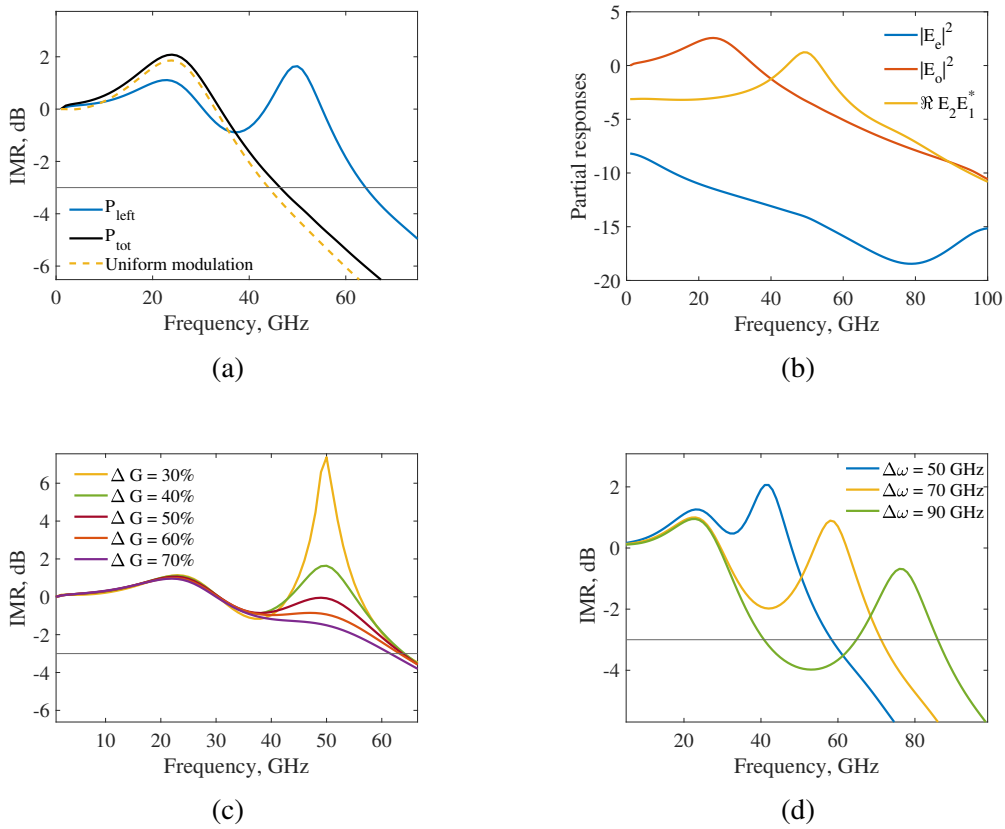

Figure 5.6: Panel (a): comparison of the IMR obtained by an RF excitation applied at the left cavity, probing the left cavity (blue) or both cavities (black). In the latter case, the IMR is comparable with that obtained under uniform modulation (yellow). Panel (b): modal contributions to the IMR as defined in (5.2). Panel (c): IMR for varying threshold gain separation. Panel (d): IMR for varying frequency separation.

a PPR bandwidth enhancement, the perfect symmetry of the device must be broken by asymmetric pumping and partial probing, which can be achieved through schemes such as those reported in [121].

Figure 5.6c shows the effect of the threshold gain separation on the IMR. It can be observed that the PPR oscillations are increasingly damped as ΔG increases. This aspect is crucial, since datacom VCSELs require a flat frequency response in order to avoid signal distortion. If ΔG is too small, the PPR oscillations become underdamped and ultimately lead to modal beating (*i.e.,* both even and odd supermodes lasing) which is detrimental for

datacom applications [117]. Figure 5.6d shows that the position of the PPR peak can be controlled by the frequency splitting $\Delta\omega$.

In order to gain a better understanding of the PPR mechanism, the photon density at the left aperture, denoted as LA, is considered:

$$S_{\mathrm{l}} = \iint_{\mathrm{LA}} \left| E_{\mathrm{e}}\Psi_{\mathrm{e}} + E_{\mathrm{o}}\Psi_{\mathrm{o}} \right|^2 \mathrm{d}x\,\mathrm{d}y \approx \frac{1}{2}|E_{\mathrm{e}}|^2 + \frac{1}{2}|E_{\mathrm{o}}|^2 - \Re\left(E_{\mathrm{e}}^* E_{\mathrm{o}}\right), \tag{5.2}$$

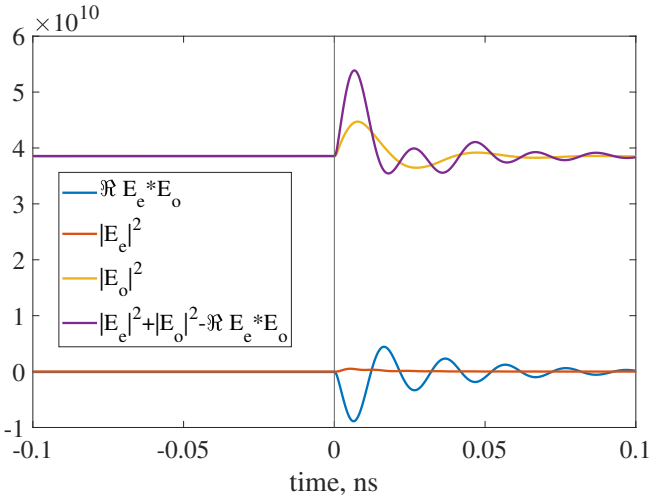

Figure 5.7: Time-resolved modal response to the impulse, as defined in (5.2).

Figure 5.7 shows the step response resolved into the three contributions of (5.2). It can be observed that the even mode is suppressed, but it remains sufficiently close to threshold to be activated during modulation and to participate in the transient response, as pointed out in [63]. These quantities can also be analyzed as a function of the modulation frequency. Figure 5.6b shows the contributions of the three addends of (5.2) to the IMR. The modal power of the suppressed mode is negligible. In addition, the carrier–photon resonance (CPR) dynamics is dominated by the power of the lasing mode, while the PPR is dominated by the cross-power term.

5.3 Effect of structural asymmetry

In order to understand the effect of structural asymmetries, such as $R_{\mathrm{l}} \neq R_{\mathrm{r}}$, a perfectly symmetric structure is first considered and the oxide-induced coupling terms k_{ox} defined in (4.44) are introduced. The cold cavity structure is considered by setting the gain $k_{\mathrm{g}} = 0$

and neglecting self-heating, *i.e.*, $k_{\mathrm{th}} = 0$. The carrier rate equations can therefore be dropped, leading to purely electric-field temporal equations of the form:

$$\partial_t E_i = \Omega_i E_i + \sum_{j=1}^{N_{\mathrm{m}}} k_{ij} E_j, \qquad k_{ij} = -\mathrm{i} v_{\mathrm{g}} k_0 \Gamma_{\mathrm{z}}' \iint_{\mathrm{AR}} \Psi_i^* \Psi_j \, \delta n_{\mathrm{ox}}(x,y) \, \mathrm{d}x \, \mathrm{d}y. \tag{5.3}$$

Here $\Omega_i = -L + \mathrm{i}\Delta\omega_i$, $N_{\mathrm{m}} = 4$, and $\Gamma_{\mathrm{z}}' = 0.01$. This system can be written in compact form as:

$$\partial_t \underline{E} = \underline{\underline{A}}\,\underline{E}, \tag{5.4}$$

The modes of the asymmetric cavity are obtained as linear combinations of the cold-cavity modes featuring time-harmonic evolution,

$$\partial_t \underline{E}_i = \lambda_i \underline{E}_i. \tag{5.5}$$

By combining (5.4) and (5.5), the eigenvalue problem:

$$\underline{\underline{A}}\,\underline{E} = \lambda\,\underline{E} \tag{5.6}$$

is obtained, where the real part of λ_i represents the attenuation of the i-th perturbed-cavity mode, while the imaginary part corresponds to its emission-frequency offset with respect to the carrier frequency ω_0. The modal envelopes are reconstructed as weighted sums of the cold-cavity modes,

$$\Psi_{\mathrm{pert},i} = \sum_{j=1}^{N_{\mathrm{m}}} V_{ji} \Psi_j, \tag{5.7}$$

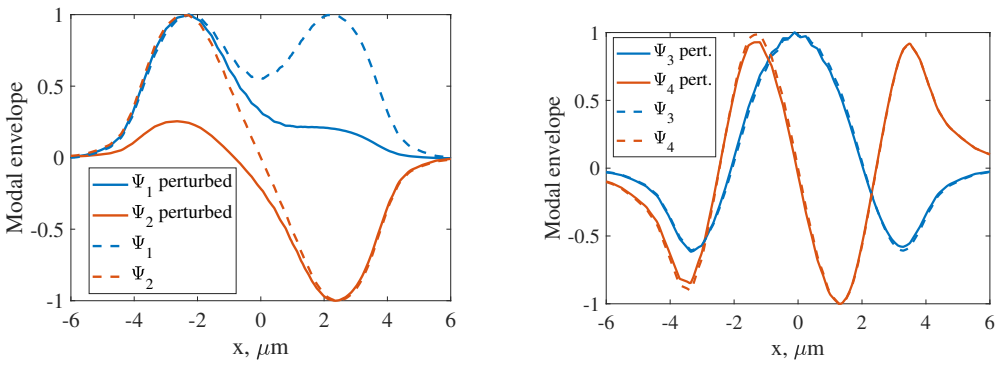

(a) (b)

Figure 5.8: Modes of the nominal cavity (dotted) and perturbed cavity (solid).

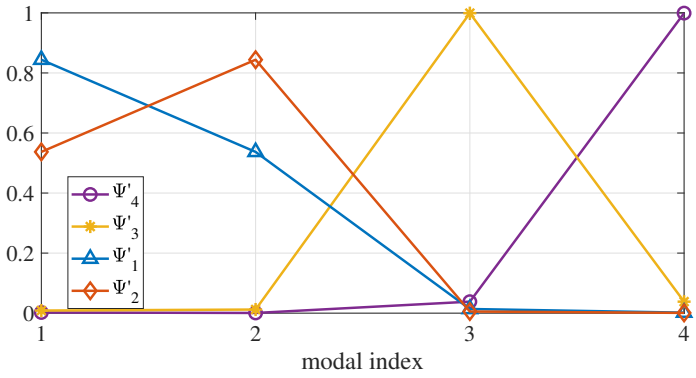

Figure 5.9: Expansion coefficients of the computed modes of Fig. 5.8b.

where Ψ_j are the nominal cavity eigenfunctions and V_{ji} is the j-th component of the i-th eigenvector of the matrix $\underline{\underline{A}}$.

Figure 5.8a shows a cut of the asymmetric-cavity modes computed by diagonalization of (5.6). The coupling matrix $\underline{\underline{A}}$ is assembled by evaluating the overlap integrals numerically on a mesh [108], assuming as an equivalent larger cavity a refractive-index perturbation $\delta n = \Delta n\, g(x,y)$, where $g(x,y)$ is a port function different from zero over the left aperture, as in [122], and $\Delta n = 0.01$. The matrix $\underline{\underline{A}}$ is then assembled and diagonalized numerically, and the perturbed-cavity modes are reconstructed using (5.7). It can be observed that the first two modal envelopes tend to localize, whereas the third and fourth are almost unaffected, in agreement with the rigorous electromagnetic simulations shown in Fig. 5.5.

Figure 5.9 shows the spectral composition of the computed modes, obtained by plotting the i-th eigenvector of the matrix $\underline{\underline{A}}$. Its inspection shows that the third and fourth modes are not *mixed*, whereas the first and second perturbed cavity modes are superpositions of the first two nominal-cavity modes.

To further clarify this result, an analytic investigation of (5.6) is carried out. The third and fourth modes are neglected, and the resulting 2×2 system obtained from (5.6) is considered:

$$\left[\begin{pmatrix} k_{11} & k_{12} \\ k_{21} & k_{22} \end{pmatrix} + \begin{pmatrix} \Omega_1 & 0 \\ 0 & \Omega_2 \end{pmatrix} \right] \begin{pmatrix} E_1 \\ E_2 \end{pmatrix} = \lambda \begin{pmatrix} E_1 \\ E_2 \end{pmatrix}. \tag{5.8}$$

By dividing the first equation by E_1 and the second one by E_2, and subtracting the latter from the former, the following equation is obtained:

$$(A_{11} - A_{22}) + A_{12}\chi - \frac{A_{21}}{\chi} = 0, \tag{5.9}$$

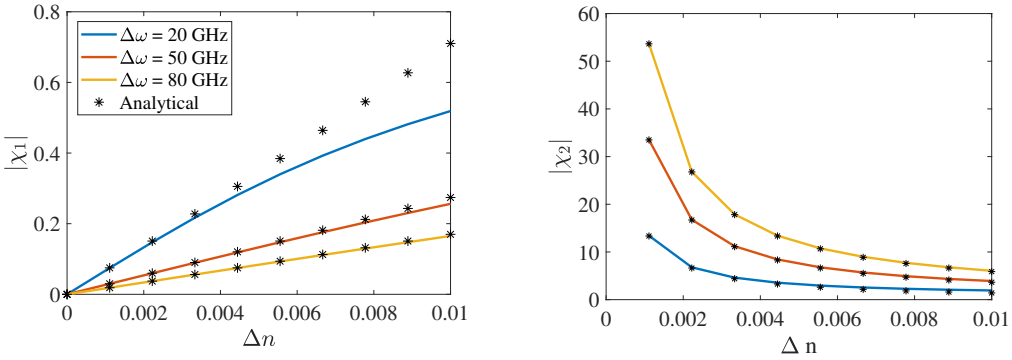

(a) (b)

Figure 5.10: Approximated solution (5.12) (black dots) compared with the numerical solution of (5.6).

where $\chi \triangleq E_1/E_2$. The factor χ quantifies the degree of mixing between the first two modes and therefore the localization effect. By inspection of the integrals defining k_{ij}, the envelopes $|\Psi_1|^2$ and $|\Psi_2|^2$ are very similar, so that $k_{11} \approx k_{22}$. Furthermore, since the eigenfunctions are real, $k_{12} = k_{21}$. Assuming $\chi \neq 0$, multiplying (5.9) by χ and applying the above approximations yields:

$$\chi^2 + \frac{\Delta\Omega}{\kappa}\chi - 1 = 0, \tag{5.10}$$

where $\kappa = k_{12} = k_{21}$ and $\Delta\Omega = \Omega_2 - \Omega_1$. Equation (5.10) has the solutions:

$$\chi_{1,2} = \frac{\Delta\Omega/\kappa \pm \sqrt{(\Delta\Omega/\kappa)^2 + 4}}{2}. \tag{5.11}$$

Since $\Delta\Omega/\kappa \gg 1$, a simplified expression can be obtained by Taylor expansion of the square root,

$$\chi_1 \approx \frac{\kappa}{\Delta\Omega} = -k_0 \frac{v_g \Gamma'_z}{\Delta\omega} \iint \Psi_1 \Psi_2 \delta n \, dx \, dy, \qquad \chi_2 \approx \frac{1}{\chi_1}. \tag{5.12}$$

Where $\Delta\Omega \approx i\Delta\omega$ has been used. The ideal unperturbed operation corresponds to $\chi_1 \to 0$. Eq. (5.12), in accordance with perturbative analyses, shows that the mixing of two modes is stronger for small frequency separations, which explains the unavoidable uncertainty of the modal parameters in the investigated bow-tie oxide aperture. Finally, Fig. 5.10 compares the numerical solution of (5.6) with the approximated analytical expression (5.12).

5.4 Effect of self-heating

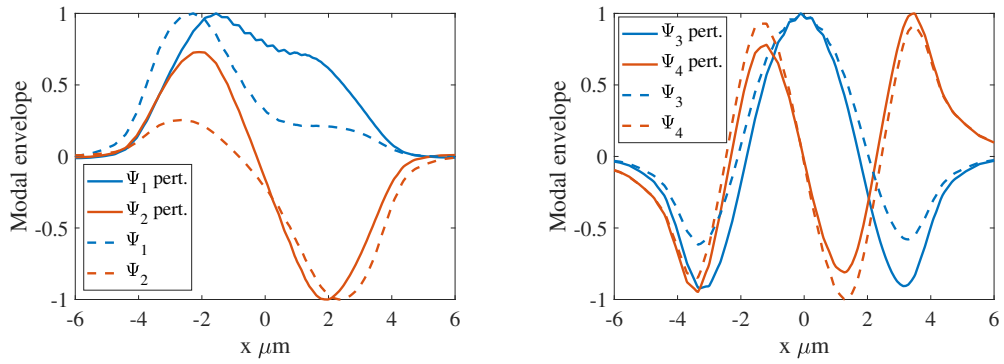

(a) (b)

Figure 5.11: Cold-cavity (dotted) and hot-cavity (solid) modes.

The self-heating terms ($k = k_{ox} + k_{th}$) are now introduced and the eigenvalue problem of Eq. (5.6) is solved. The assumed thermal profile is a Gaussian centered at the bridge center, whose expression reads:

$$T(x,y) = T_0 \exp\left(-\frac{x^2}{\sigma_x^2} - \frac{y^2}{\sigma_y^2}\right), \tag{5.13}$$

where T_0 is the peak self-heating temperature and $\sigma_{x,y}$ are the standard deviations, both chosen as fitting parameters. The temperature profile is then converted into a variation of refractive index by a phenomenological coefficient $\frac{dn}{dt} = 2.2 \cdot 10^{-4} \mathrm{K}^{-1}$. The same procedure of previous section is carried out to compute the hot cavity modes. The corresponding envelopes are shown in Fig. 5.11a. The main effects predicted by the electromagnetic simulations of Fig. 5.5 are reproduced: the modes tend to be less localized and are lensed toward the center of the device.

This analysis also provides useful insights into thermal lensing in a standard VCSEL. For a nominal symmetric device ($k_{ox} = 0$), thermal lensing acts as an even perturbation and therefore does not couple even and odd modes. Consequently, a treatment analogous to Eq. (5.12) can be carried out:

$$\chi \approx \mathrm{i}k_0 \frac{v_g \Gamma_{th}}{\Delta\Omega_{13}} \frac{dn}{dT} \iint \Psi_1 \Psi_3 T(x,y)\, dx\, dy, \tag{5.14}$$

and a similar expression holds for modes 2 and 4. Here, Γ_{th} is a phenomenological confinement factor of the temperature, set to 1. Despite $\Delta\Omega_{13}$ being large, the thermal

coupling is much stronger than the k_{ox}-induced coupling due to the higher longitudinal confinement. Eq. (5.14) shows that VCSELs with small modal frequency separations exhibit a stronger thermal-lensing effect. This conclusion is reasonable, because small frequency separation arise in weakly guiding structures, where indeed a stronger impact of the thermal lensing on the modes is expected.

5.5 Characterization and modeling of transverse modal locking

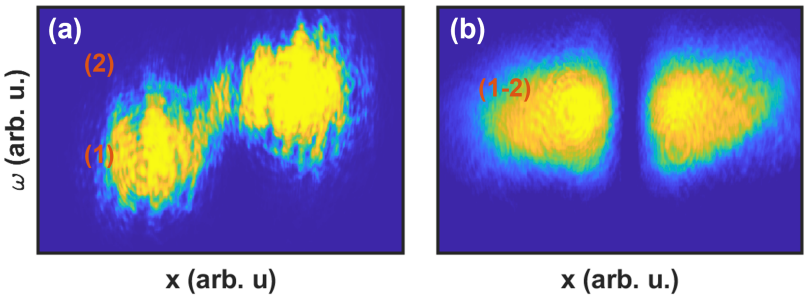

Figure 5.12: Frequency-resolved near field for $I = 7\,\text{mA}$ (a) and $8\,\text{mA}$ (b). In panel (a), each cavity features a dominant frequency, denoted by (1) and (2), while in panel (b) the cavities are frequency locked. Taken from [75].

In this section, the experimental characterization and numerical modeling of a bow-tie device are presented. The investigated structure corresponds to the one fabricated and reported in [75]. The oxide aperture profile, sketched in Fig. 5.1, includes an asymmetry inferred to reproduce the experimentally observed behavior, specifically $R_\text{l} = 1.5\,\mu\text{m}$ and $R_\text{r} = 1.4\,\mu\text{m}$.

The device exhibits two distinct regimes. At low injection currents, it operates in the *weakly coupled regime* (WCR), in which the two cavities lase at different wavelengths. At higher injection levels, the system transitions into the *coherent regime* (CR), characterized by frequency locking, such that both cavities emit at a common wavelength. The minimum current required to induce the transition between these two regimes is denoted by I_0, and for the device under consideration it lies in the range 5–8 mA. Figure 5.12 shows the frequency-resolved near field (FRNF) for injection currents I below and above the transition current

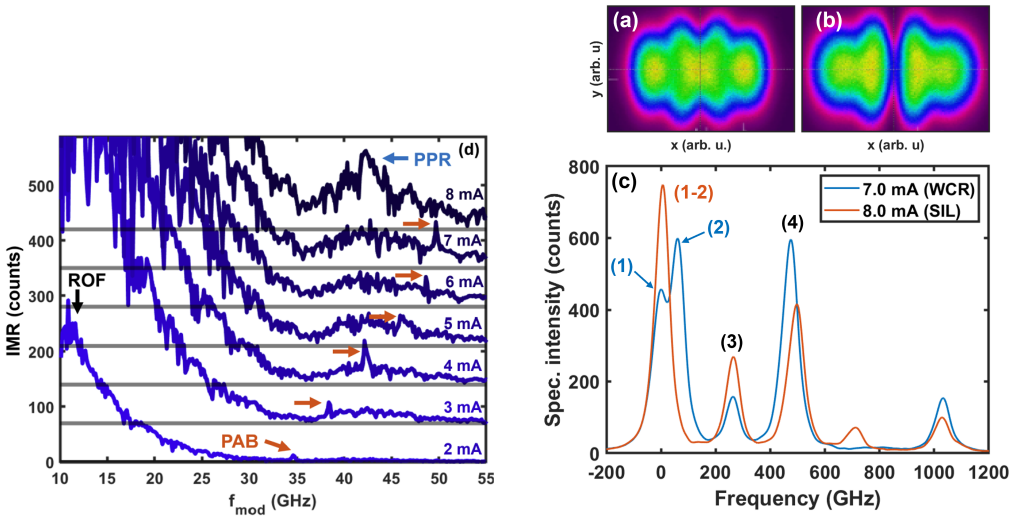

(a) (b)

Figure 5.13: Panel (a): measured IMR for varying current, highliting PPR and *plasma-assisted* beating (PAB). Panel (b): measured optical spectrum for the WCR (blue) and CR case (red). Top part of panel (b): FF for the WCR (left) and CR (right). Taken from [75].

I_0, in the left and right panels, respectively. Contributions from higher-order transverse modes are omitted for sake of clarity. This measurement highlights the distinct signatures of the two operational regimes: for $I < I_0$, each cavity exhibits a dominant and spectrally separated emission peak, while for $I > I_0$ the two cavities are frequency locked and emit at a common wavelength. This behavior is also evident in the measured optical spectrum reported in Fig. 5.13b: for $I > I_0$, the two lowest-order spectral peaks merge into a single line. In the CR, the spatial profile of the locked mode exhibits a central node, suggesting an odd-like supermode configuration. The far-field (FF) pattern in the WCR, shown in the upper inset, corresponds indeed to that of an out-of-phase near field. Figure 5.13a reports the intensity modulation response at each current. In the WCR, the response is that of a standard VCSEL plus a narrow peak, due to the beating of the first two modes. Such an effect is detrimental in datacom applications [117], but can be used to generate a radio-frequency signal by means of a photoconductive antenna [76]. As the current increases, the beating peak shifts toward higher frequency, until I_0 is reached. It has to be remarked that such a measurement, performed by a streak camera, tends to underestimate the amplitude of the beating peak, as discussed in [100]. In the CR, the beating peak is not visible, and the response is enhanced by a broader PPR feature, which, however, does

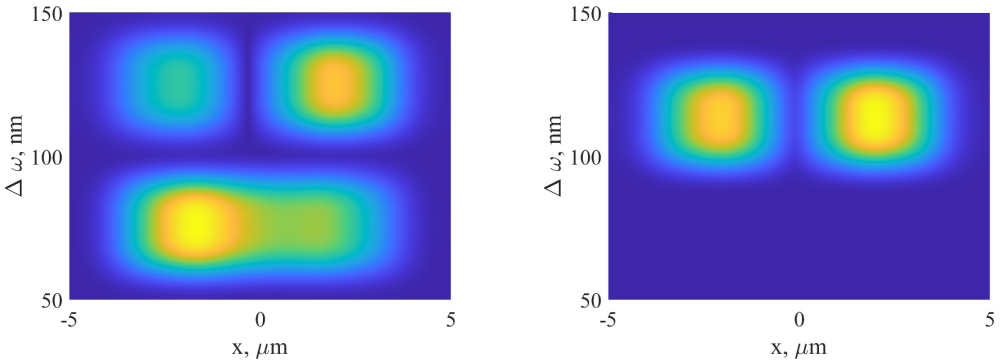

Figure 5.14: Simulated FRNF for the WCR (a) and CR (b). Taken from [75]

not provide an effective improvement of the high-speed performance since it is below the minus 3 dB line. For currents close to the transition, an intermediate regime, where both features are present, is visible.

The observed behavior is now reproduced and interpreted by means of the developed modeling chain. For sake of clarity, the simplified form of the material gain of Eq. (2.3) is considered. The modes of an asymmetric structure with an added thermal profile of Fig. 5.5 (c) are considered. Since the oxide asymmetries and self-heating are already taken into account by the modal solver, $k_{\mathrm{ox}} = k_{\mathrm{th}} = 0$ is set. The device is simulated for $I = 7\,\mathrm{mA}$ and 8 mA. The adopted model can naturally handle the transition from the WCR ($I = 7\,\mathrm{mA}$) to the CR ($I = 8\,\mathrm{mA}$) as a transverse-mode phase locking thanks to the presence of the modal coupling terms k_{ij}. In particular, the solutions of the electric field can be generally written as:

$$E_{\mathrm{s}}(r,t) = |A_1(t)|e^{\mathrm{i}\phi_1(t)}\Psi_1 + |A_2(t)|e^{\mathrm{i}\phi_2(t)}\Psi_2 + \cdots, \tag{5.15}$$

which can be classified, for the CR and WCR, respectively, as:

$$\partial_t(\phi_1 - \phi_2) = 0, \ (\mathrm{CR}) \quad \partial_t(\phi_1 - \phi_2) \neq 0 \ (\mathrm{WCR}). \tag{5.16}$$

The first expression corresponds to a frequency-locked solution, where the two first modes oscillate at the same frequency. In the CR case, the solution can be expressed as:

$$E_{\mathrm{s}}(r,t) \propto \underbrace{(k\Psi_1 + \Psi_2)}_{\text{coherent near field}} e^{\mathrm{i}\omega_{12}t} + \cdots, \tag{5.17}$$

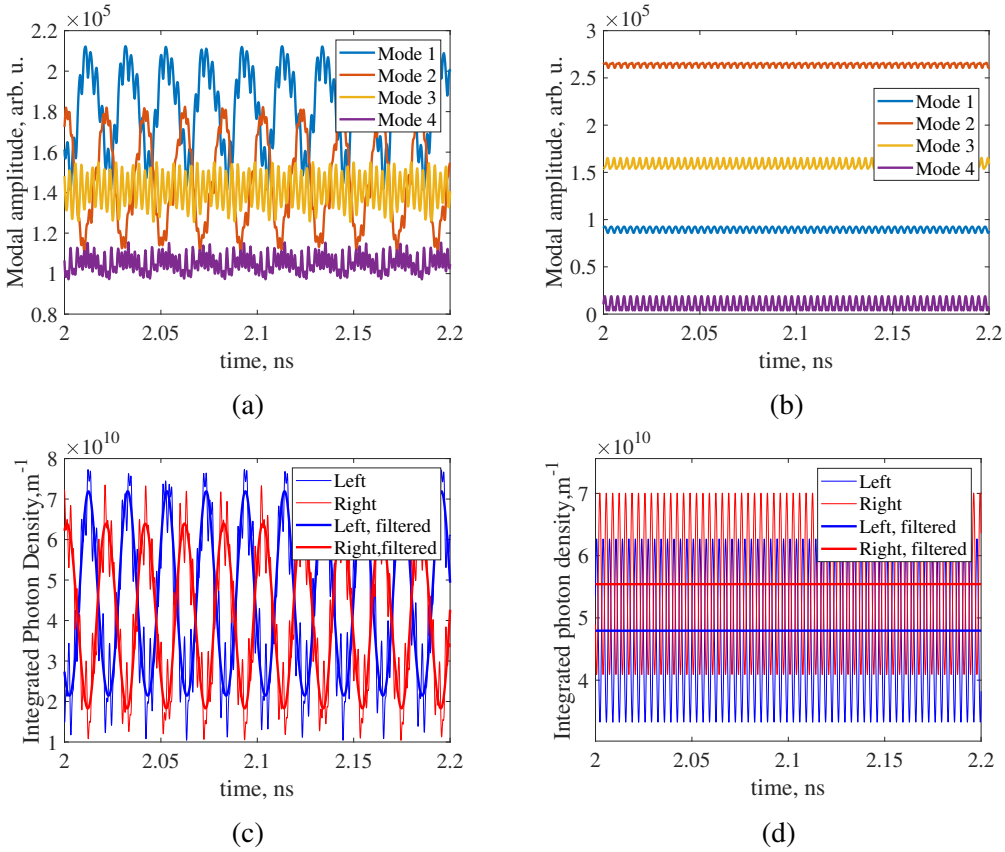

Figure 5.15: Top: Modal amplitudes for $I = 7\,\text{mA}$ (WCR) and 8 mA (CR) at left and right panels, respectively. Bottom: corresponding photon densities at the right and left cavities, with and without a numerical low-pass filter that eliminates the high-order beating.

where k is a complex number and ω_{12} is a locking frequency, both to be found as a solutions of the dynamical problem. Figure 5.14 shows the simulated FRNF for $I = 7\,\text{mA}$ (left) and 8 mA (right). The latter is obtained by considering the electric-field amplitudes as a function of frequency:

$$\text{FRNF}(x,\omega) = \sum_{i=1}^{N_\text{m}} E_i(\omega)\Psi_i(x,0). \tag{5.18}$$

In particular, once the turn-on transient is finished, each modal amplitude is processed by a bandpass filter centered at a selected frequency ω and featuring a passband of a few gigahertz, in order to emulate the spectral resolution of the measurement instrument, and the resulting signal is subsequently weighted by the corresponding wavefunction in

order to incorporate spatial resolution. It can be seen that an excellent agreement with the experimental observation of Fig. 5.12 is found.

To gain more insight about the description of both dynamical regimes, Fig. 5.15 shows the modal amplitude as a function of time for the CR and WCR. In the WCR (left), the modal amplitudes feature an oscillation due to the modal beating (*i.e.,* both supermodes lasing), while in the CR (right) the modal amplitude can be considered steady, as the separation frequency with high-order modes is sufficiently large to cut off the multimodal interaction, as in the incoherent approximation described in Sec. 4. The resulting photon densities are reported in the bottom part of Fig. 5.15. The thicker lines correspond to the low-pass-filtered photon density, which is introduced to mimic the receiver bandwidth and eliminate the contribution of high-order modal beating. It can be observed that, in the first case, a pronounced antiphase oscillation appears in the integrated photon density of the left and right cavities. Such antiphase oscillations have been experimentally reported in [74] by means of streak-camera measurements. In that configuration, however, the beating oscillations become visible only when an external optical pumping is applied. This limitation arises from the intrinsic operating principle of the streak camera, as discussed in [75]. The measurement procedure indeed performs an averaging over multiple acquisitions. Since the relative phase of the beating oscillations varies randomly from acquisition to acquisition, the streak-camera averaging suppresses the beating signature unless an optically injected pulse enforces phase synchronization. Nevertheless, the existence of anti-phase beating, even without external excitation, has been confirmed in [76]. Consequently, streak-camera measurements tend to underestimate the beating amplitude in the IMR, while this is significantly more visible in network analyzer measurements [73]. Finally, the IMR is simulated at $I = 2\,\mathrm{mA}$, $7\,\mathrm{mA}$, and $8\,\mathrm{mA}$. Such a simulation is performed by emulating the operating principle of a network analyzer. In particular, for each investigated frequency, an input sinusoidal current is superimposed on the static bias. The output is then filtered at the same frequency by means of a heterodyne receiver. For the $I = 2\,\mathrm{mA}$ case, self-heating is neglected, and therefore the modes of Fig. 5.5 (a) are used. In the WCR, when selecting a frequency close to the frequency separation, the beating peak falls into the receiver bandwidth. This explains the presence of the sharp feature in Fig. 5.13. It has to be remarked, however, that this feature does not represent any bandwidth improvement and it is solely an artifact of the adopted measurement and simulation technique. When the simulated VCSEL switches to the CR, a modest broader PPR feature is present, which, however, is too small to provide any bandwidth improvement. This happens due to the quasi-perfect symmetry of the cavity, which, as explained in Sec. 4.4, prevents having a single-contact PPR scheme. The three

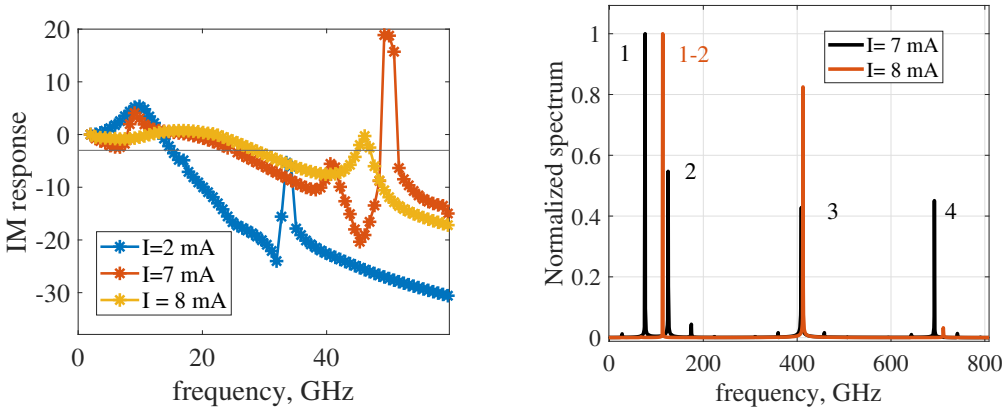

(a) (b)

Figure 5.16: Panel (a): simulated IMR responses for $I = 2\,\text{mA}$, $7\,\text{mA}$, and $8\,\text{mA}$. Panel (b): simulated optical spectrum at $I = 7.5\,\text{mA}$ (WCR) and $8\,\text{mA}$ (CR), from [75].

different regimes reported in Fig. 5.16a are reproduced with qualitative agreement. Finally, Fig. 5.16b shows the simulated optical spectrum for $I = 7\,\text{mA}$ and $8\,\text{mA}$, obtained by a FFT of the sum of the modal amplitudes. It can be seen that, when the CR takes place, the first two lines merge into a single one, Additionally, the third mode which lies in the bridge region of the bow-tie, takes advantage, while the fourth one is suppressed.

The conditions for which a stable CR solution is found are complex and depend on several factors, such as the modal overlap, which is related to self-heating and structural asymmetries, the material parameters, such as the linewidth enhancement factor, the injected current, and most importantly the frequency separation. Regarding the latter parameter, CR is possible only for sufficiently small frequency separations, in analogy to injection-locking theory [123]. Further insights are provided in the next chapter by means of a simplified and less computationally demanding lumped model.

5.6 Hot-cavity modes

In the previous section, the coherent regime was interpreted as a transverse mode locking, in which the spectral lines associated with the first two transverse modes collapse into a single emission peak. At first glance, this interpretation appears to conflict with the operating principle of PPR devices, which relies on the presence of two distinct modes separated by a characteristic frequency spacing Δf. Other examples of PPR effect in the CR

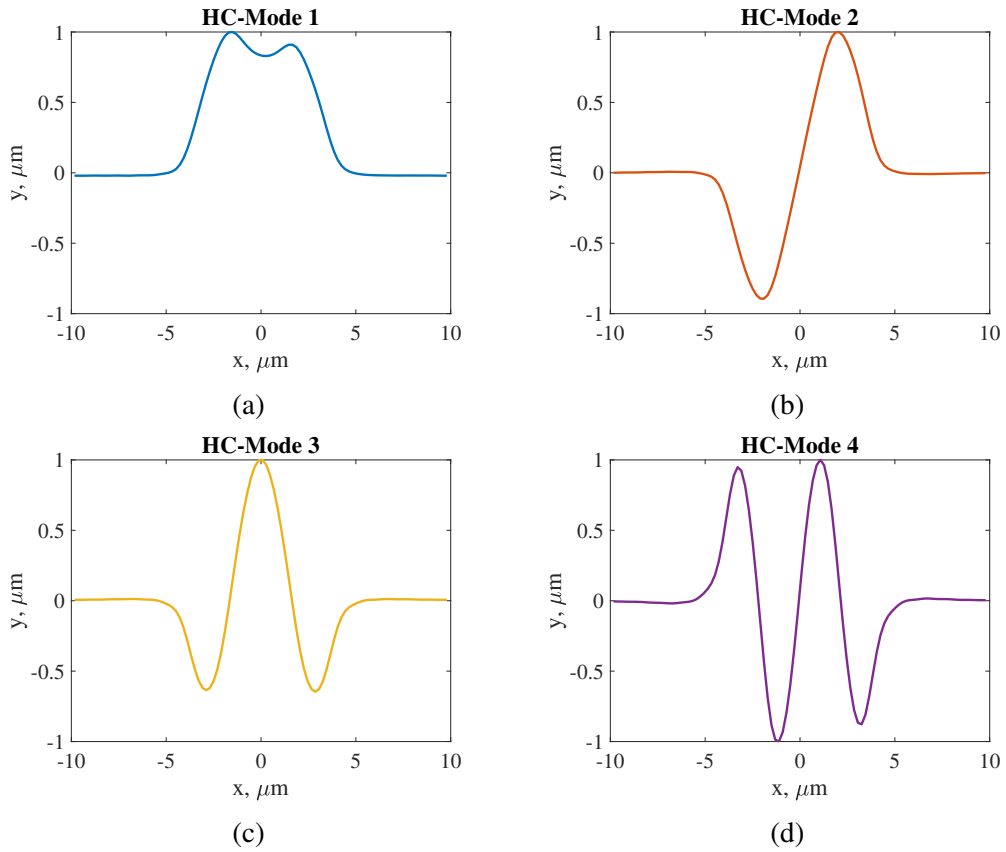

Figure 5.17: Plot of the hot cavity modal envelopes, defined as (5.20) in the coherent regime.

are observed in the noise spectrum in [61]. Moreover, from an experimental standpoint, it may seem natural to associate each observed spectral line with a nonzero modal amplitude. To resolve this apparent inconsistency, it is necessary to shift the focus from the optical modes, used in this work primarily as a mathematical basis for the field expansion, to the so-called *hot-cavity modes*, which are defined as follows.

If the carrier density does not vary significantly in time, as is the case in the coherent regime (CR), the coupling matrix $\underline{\underline{K}}$, which depends on the gain and therefore on the carrier density, may be treated as time-independent. Under this assumption, the electric-field dynamics can be written as

$$\partial_t \underline{E} = \left[\underline{\underline{D}} + \underline{\underline{K}}(N)\right] \underline{E} = \underline{\underline{A}}(N)\underline{E}. \tag{5.19}$$

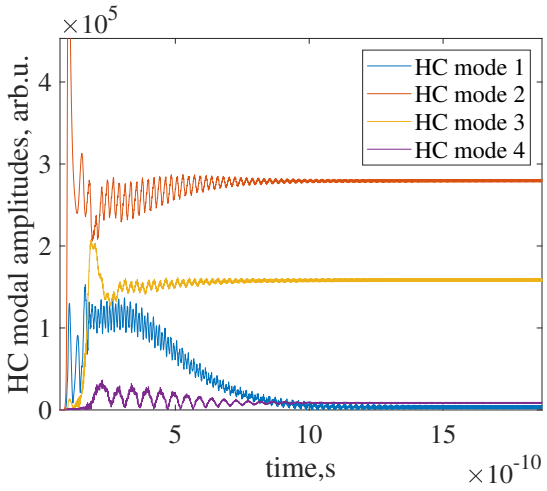

Figure 5.18: Amplitudes of the hot-cavity modes as a function of time

The time-harmonic field configurations that remain stable in the CR, referred to here as *hot-cavity* (HC) modes, correspond to specific linear combinations of the cold-cavity modes that diagonalizes the matrix $\underline{\underline{A}} = \underline{\underline{K}} + \underline{\underline{D}}$:

$$\Psi_i^{\mathrm{hc}} = \sum_{j=1}^{N_m} V_{ij} \Psi_j, \tag{5.20}$$

where V_{ji} is the j-th element of the i-th eigenvector of the matrix $\underline{\underline{A}}$. The imaginary parts of the eigenvalues of $\underline{\underline{A}}$ determine the oscillation frequencies of the HC modes, while the real parts describe their net losses.

Figures 5.17a–5.17d show the four HC modes found in the CR. The second HC mode corresponds to an odd supermode, which is also the experimentally observed stable configuration, whereas the first HC mode represents an alternative coherent solution with even symmetry. Specifically, these mode profiles closely resemble those of a perfectly symmetric device.

An *effective* mode spacing can be defined as

$$\Delta f_{\mathrm{eff}} = \frac{\Im\left(\lambda_1 - \lambda_2\right)}{2\pi}, \tag{5.21}$$

where λ are the eigenvalues of the matrix $\underline{\underline{A}}$. For the present device yields $\Delta f_{\mathrm{eff}} \approx 32$ GHz, therefore PPR effects are expected to occur at this characteristic frequency.

Fig. 5.18 reports the modal amplitudes expressed in the basis of the hot-cavity modes. In this representation, after an initial turn on transient, the number of nonzero modal

amplitudes coincides with the number of spectral peaks, thus restoring the intuitive correspondence "one spectral line for one (hot cavity) mode". The formation of hot-cavity modes takes place when multimode interactions are relevant, *i.e.,* for small frequency separation. This is also the case of large area VCSELs, where the hot-cavity modes approach might explain the localization of the optical modes induced by current crowding at the edge of the oxide aperture [34].

5.7 Unbalanced current injection

In this section, a device similar to those reported in [70, 61, 59] is simulated to provide an additional experimental benchmark. This geometry consists of a two-aperture laser defined by a photonic crystal, with the key difference that the two cavities are pumped independently. This configuration can be implemented, for example, via double electrical contacts combined with proton bombarding [59].

Specifically, the current distribution is modeled as

$$J(x,y) = J_1\, a_{\mathrm{l}}(x,y) + J_2\, a_{\mathrm{r}}(x,y), \tag{5.22}$$

where $a_{\mathrm{l,r}}(x,y)$ are port functions equal to 1 within the left and right apertures, respectively, and zero elsewhere.

The asymmetric geometry of Fig. 5.5 (b) is considered, and is then perturbed through the thermal coupling coefficients k_{th}. The thermal corrections k_{th} depend on the temperature distribution, which is phenomenologically linked to the injection currents through

$$T(x,y) = t_{\mathrm{l}}(x,y)\, I_{\mathrm{l}} + t_{\mathrm{r}}(x,y)\, I_{\mathrm{r}}, \qquad t_{\mathrm{l,r}}(x,y) = k \exp\left(-\frac{(x - x_{\mathrm{l,r}})^2}{\sigma_{\mathrm{x}}^2} - \frac{y^2}{\sigma_{\mathrm{y}}^2} \right), \tag{5.23}$$

where $x_{\mathrm{l,r}}$ denote the centers of the left and right apertures, respectively, and k is a phenomenological coefficient set to $7.5\,\mathrm{K\,mA^{-1}}$.

Figure 5.19 shows the optical spectrum associated with the first two modes as a function of I_{r}, for a fixed left-cavity current $I_{\mathrm{l}} = 3\,\mathrm{mA}$. The third and fourth transverse modes remain below cutoff in this configuration, unlike in the previously analyzed device. This difference arises from the modified injection profile, in particular from the absence of carrier injection in the bridge region. Superimposed on the optical spectrum, the green and red curves represent the emission wavelengths of the first and second hot-cavity modes, as defined in the previous section. The dotted green line denotes the region where the correspondent HC-mode is not lasing.

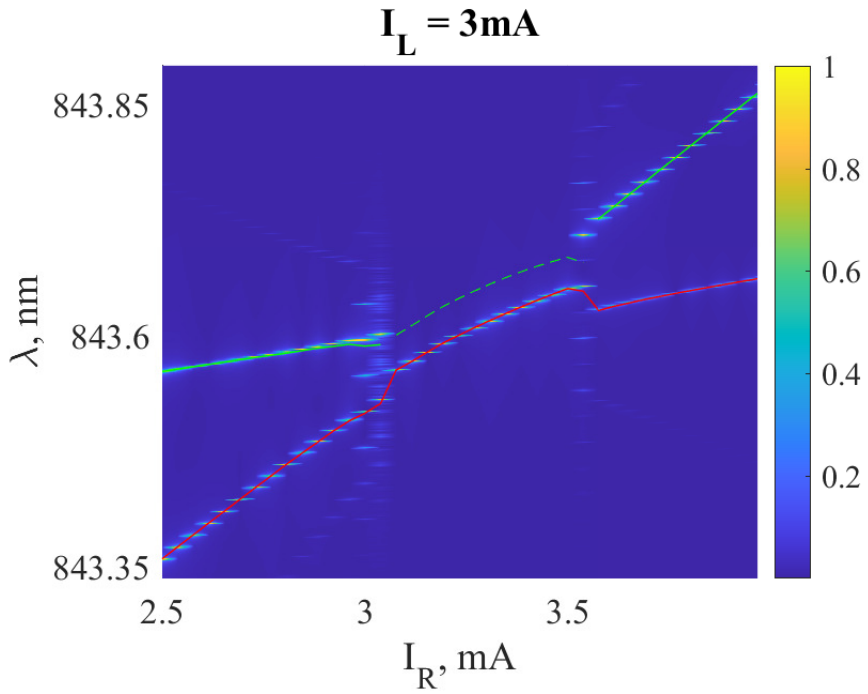

Figure 5.19: Simulated optical spectrum for varying I_r, at fixed $I_l = 3\,\text{mA}$. The green and red lines are the emission wavelengths of the hot-cavity modes, as defined in the previous section, from [106].

Figure 5.20 reports the corresponding frequency-resolved near fields (FRNFs) for different current combinations. Starting from the left side of Fig. 5.19, for $I_r < I_l$ the device operates in the weakly coupled regime (WCR), as illustrated in panel (a) of Fig. 5.20. In this regime, the temperature imbalance between the two cavities produces a frequency separation that is too large to allow coherent locking.

When I_r becomes comparable to I_l, the device transitions into the coherent regime. As extensively observed experimentally [59, 61], the CR region is not symmetric with respect to the point $I_r = I_l$, reflecting the structural asymmetry of the apertures. In particular, coherent coupling is observed when the smaller cavity is hotter. This suggests that small structural asymmetries can be compensated by thermal effects.

Finally, for $I_r > I_l$, the device returns into the WCR: the right cavity becomes the hottest and therefore emits at a longer wavelength. The computation of the HC modes eigenvalues allows to visualize a frequency separation also in the CR, where only one spectral line is present.

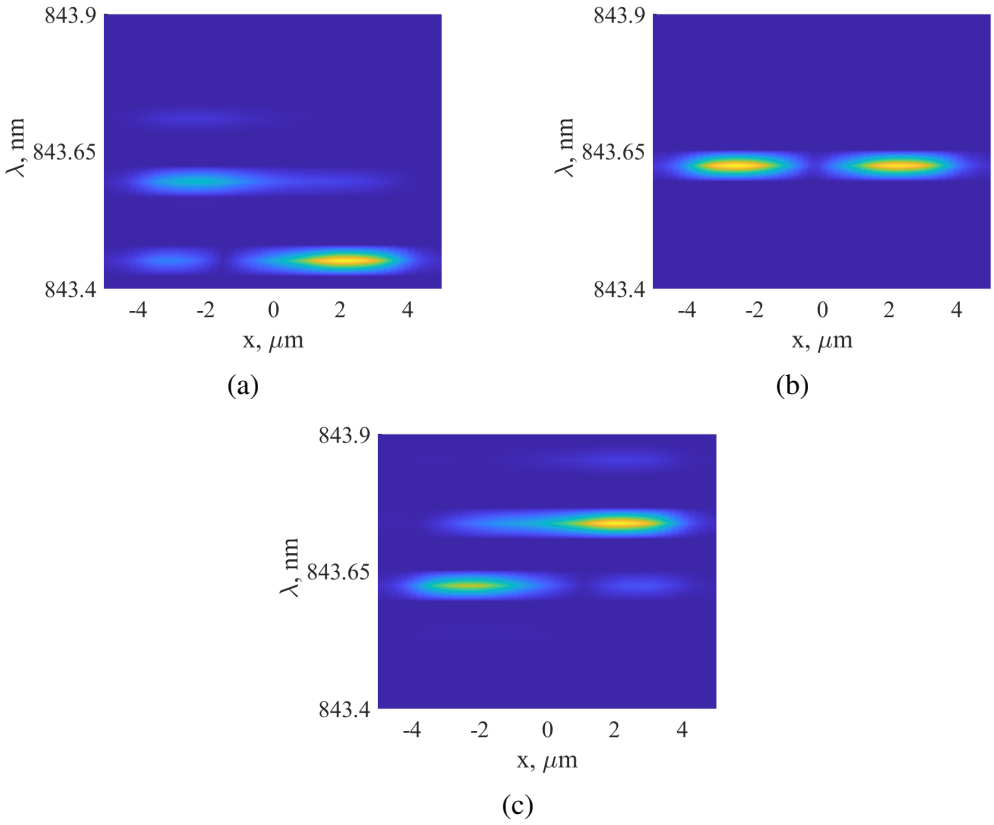

Figure 5.20: FRNF for $I = 2.8\,\mathrm{mA}$ (a), $3.3\,\mathrm{mA}$ (b), and $3.6\,\mathrm{mA}$ (c).

Chapter 6

Lumped model

The perturbative analysis performed in the previous sections 5.4 and 5.3 suggests that multimode interactions are relevant for small frequency separations. Specifically, truncation of the electric field to the first two modes is sufficient to study most of the effects investigated in this work, such as PPR and frequency locking. The field is therefore expanded as:

$$E_{\mathrm{S}} = E_{\mathrm{o}}\Psi_{\mathrm{o}} + E_{\mathrm{e}}\Psi_{\mathrm{e}}, \tag{6.1}$$

where the subscript o denotes the odd mode and the subscript e denotes the even mode. The dynamical equations read:

$$\partial_t E_{\mathrm{e}} = k_{\mathrm{ee}}E_{\mathrm{e}} + k_{\mathrm{eo}}E_{\mathrm{o}} - L_{\mathrm{e}}E_{\mathrm{e}}, \tag{6.2}$$

$$\partial_t E_{\mathrm{o}} = k_{\mathrm{oo}}E_{\mathrm{o}} + k_{\mathrm{oe}}E_{\mathrm{e}} - L_{\mathrm{o}}E_{\mathrm{o}} + \mathrm{i}\Delta\omega E_{\mathrm{o}}, \tag{6.3}$$

It is assumed that the carrier distribution is piecewise constant in the right and left cavities, with values N_{r} and N_{l}, respectively:

$$N(x) = \begin{cases} N_{\mathrm{l}}, & x < 0, \\ N_{\mathrm{r}}, & x > 0, \end{cases} \tag{6.4}$$

A linear form of the gain is also assumed:

$$g_{\mathrm{l,r}} = (1 + \mathrm{i}\alpha_{\mathrm{h}})G_{\mathrm{d}}\frac{(N_{\mathrm{l,r}} - N_{\mathrm{tr}})}{1 + \varepsilon S}. \tag{6.5}$$

The coupling coefficients k can therefore be computed as:

$$k_{ij} = (1+\mathrm{i}\alpha_\mathrm{h})G_\mathrm{d}v_\mathrm{g}\Gamma_\mathrm{z}\left[N_\mathrm{r}\underbrace{\iint_\mathrm{RC}\Psi_i^*\Psi_j\,\mathrm{d}x\,\mathrm{d}y}_{\triangleq\alpha_{ij,\mathrm{R}}}+N_\mathrm{l}\underbrace{\iint_\mathrm{LC}\Psi_i^*\Psi_j\,\mathrm{d}x\,\mathrm{d}y}_{\triangleq\alpha_{ij,\mathrm{L}}}\right], \qquad i\neq j, \tag{6.6}$$

$$k_{ii} = (1+\mathrm{i}\alpha_\mathrm{h})G_\mathrm{d}v_\mathrm{g}\Gamma_\mathrm{z}\left[N_\mathrm{r}\underbrace{\iint_\mathrm{RC}\Psi_i^*\Psi_i\,\mathrm{d}x\,\mathrm{d}y}_{\triangleq\alpha_{ii,\mathrm{R}}}+N_\mathrm{l}\underbrace{\iint_\mathrm{LC}\Psi_i^*\Psi_i\,\mathrm{d}x\,\mathrm{d}y}_{\triangleq\alpha_{ii,\mathrm{L}}}\right], \tag{6.7}$$

where RC and LC denote the Right and Left cavities. All the information on the spatial profile of the mode is compacted in the coefficients α. The photon density is computed as an integral over the Right and Left cavities of $|E|^2$:

$$S_\mathrm{l} = \alpha_{\mathrm{ee,l}}|E_\mathrm{e}|^2+\alpha_{\mathrm{oo,l}}|E_\mathrm{o}|^2+2\,\Re\big(\alpha_{\mathrm{oe,l}}E_\mathrm{e}E_\mathrm{o}^*\big), \tag{6.8}$$

$$S_\mathrm{r} = \alpha_{\mathrm{ee,r}}|E_\mathrm{e}|^2+\alpha_{\mathrm{oo,r}}|E_\mathrm{o}|^2+2\,\Re\big(\alpha_{\mathrm{oe,r}}E_\mathrm{e}E_\mathrm{o}^*\big). \tag{6.9}$$

The model is completed with the carrier equations:

$$\partial_t N_\mathrm{l,r} = -\frac{N_\mathrm{l,r}}{\tau_n}+G_\mathrm{d}\frac{(N_\mathrm{l,r}-N_\mathrm{tr})}{1+\varepsilon S_\mathrm{l,r}}S_\mathrm{l,r}+\frac{I_\mathrm{l,r}}{qV_\mathrm{a}}, \tag{6.10}$$

where V_a is the active volume associated with one cavity, and $I_\mathrm{l,r}$ is the current injected into each cavity. The lumped model presents all the features of its distributed counterpart [119], but lacks a quantitative description of spatial hole burning and modal competition. The presented strategy allows computationally efficient large parametric investigation of the equations under investigation.

6.1 Transverse mode locking maps

In Sec. 5.5, the characterization and modeling of transverse mode locking have been presented. The conditions for stable mode locking include a sufficient degree of coupling among the modes, *i.e.,* a sufficiently large spatial overlap, a suitable range of frequency separations $\Delta\omega$, and material parameters such as α_h.

In order to gain further insight into the stability ranges of the parameters yielding stable mode locking, a set of simulations has been performed by varying the aforemen-

tioned quantities, which are now treated as input parameters. Realistic estimates of the modal envelopes have been obtained by linear superposition of the even and odd modes, analogously to what has been reported in Sec. 5.3:

$$\Psi_1 = \frac{1}{\sqrt{1+\chi^2}}\left(\Psi_\mathrm{e} + \chi\Psi_\mathrm{o}\right), \qquad \Psi_2 = \frac{1}{\sqrt{1+\chi^2}}\left(-\chi\Psi_\mathrm{e} + \Psi_\mathrm{o}\right), \tag{6.11}$$

where the square-root factor provides normalization, and $\chi = 0$ corresponds to a perfectly symmetric device.

A double sweep over χ and $\Delta\omega$ has been carried out, both quantities being treated as free parameters. The coupling coefficients α have subsequently been computed, and the corresponding set of lumped equations has been assembled. The simulations have been performed under symmetric current injection, *i.e.,* $I_\mathrm{l} = I_\mathrm{r} = 4\,\mathrm{mA}$. Once the transient regime has finished, the optical spectrum has been evaluated by applying an FFT to the sum of the modal amplitudes. If the optical spectrum exhibits two distinct peaks, the corresponding solution has been classified as the weak coupling regime (WCR), while if a single peak is observed, the solution has been classified as the coupling regime (CR).

Figure 6.1 reports the classification of the obtained solutions as a function of $\Delta\omega$ and of the modal coupling k, defined as $2|\alpha_{\mathrm{eo},1}|$. The simulations have been performed both including and neglecting spectral hole burning ε. In the left panel, a zero threshold-gain separation between the modes has been assumed. Under this condition, the governing equations are symmetric with respect to $\Delta\omega = 0$, therefore, only the upper half of the parameter space is shown. It can be observed that the CR is allowed only for sufficiently large values of the coupling, and that spectral hole burning significantly enlarges the parameter region in which the CR is stable. However, the underlying description of this mechanism is phenomenological, therefore, the resulting predictions must be interpreted with caution.

In the right panel, a threshold gain separation of 20 % is considered, selecting the odd mode. Remarkably, in this case the CR region plot resembles that of phase locking in an optically pumped laser [124], featuring its typical frequency asymmetry [125]. In particular, the coupling is associated with the injected optical power, while $\Delta\omega$ is associated with the frequency detuning. It can be seen that, for a preferred frequency detuning, the required coupling is much lower than that needed in the left panel. An analytical investigation of the stable CR regions is carried out for the condition $k = 1$ in Sec. 6.3, where the concept of CR reduces to single-mode emission, and by neglecting spectral hole burning, revealing the mechanism of the frequency asymmetry of the presented equations.

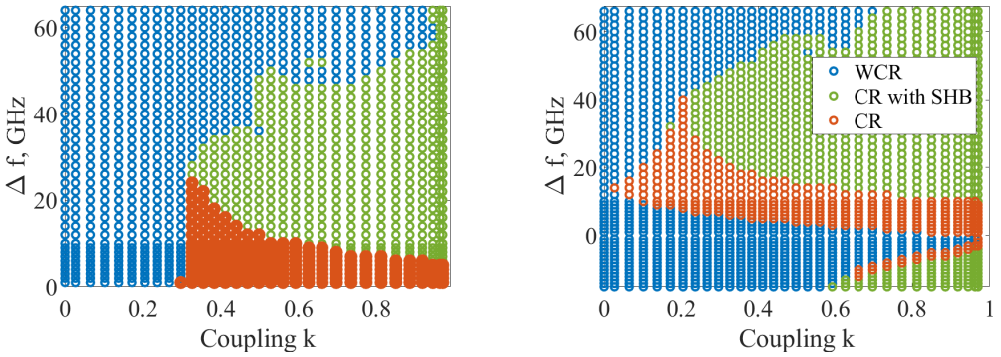

(a) (b)

Figure 6.1: Dynamical regime (CR or WCR) for varying the coupling k and the frequency separation Δf for threshold gain-degenerated modes (a) and assuming a 20 % separation (b).

6.2 Analytical investigation of the bandwidth enhancement

In this section, an analytical investigation of the derived lumped model is carried out to provide an interpretation of the findings outlined in Sec. 5.2. In order to obtain analytical solutions, the perfectly symmetric case is considered, *i.e.*,:

$$\alpha_{\mathrm{ee,l,r}} = \alpha_{\mathrm{oo,l,r}} = \frac{1}{2}, \qquad \alpha_{\mathrm{eo,l}} \approx \frac{1}{2}, \quad \alpha_{\mathrm{eo,r}} \approx -\frac{1}{2}. \tag{6.12}$$

In addition, spectral hole burning is neglected ($\varepsilon = 0$). The static solution for the current $I_{\mathrm{l}} = I_{\mathrm{r}} = I$ can be obtained by solving Eqs. (6.3)–(6.10), with $\partial_t = 0$:

$$\begin{aligned} &S = \frac{-N_{\mathrm{th}}/\tau_{\mathrm{n}} + I/(qV_{\mathrm{a}})}{v_{\mathrm{g}} G_{\mathrm{d}} (N_{\mathrm{th}} - N_0)}, \quad E_1 = \sqrt{2S}, \quad k_{ii} = (1 + \mathrm{i}\alpha_{\mathrm{h}}) L_1, \quad k_{ij} = 0, \\ &E_2 = 0, \quad N_{\mathrm{l,r}} = N_{\mathrm{th}}, \quad N_{\mathrm{th}} = \frac{1}{\tau_{\mathrm{p1}} v_{\mathrm{g}} \Gamma p_{\mathrm{R}}} + N_{\mathrm{tr}}. \end{aligned} \tag{6.13}$$

where E_1 is the amplitude of the lasing mode, which, without loss of generality, can be the even or the odd one and can be considered real. The modal loss difference $\Delta L \triangleq L_1 - L_2$ is negative: indeed solution (6.13) is physically meaningful only if the losses of the first mode are the smallest. The quantity $\Delta\omega = \omega_2 - \omega_1$ is positive or negative in the case of even or odd mode lasing, respectively, according to the nodes theorem, which states that the odd mode has a higher frequency.

As normally done in small-signal analysis, a small time-varying current is superimposed on the static one. This implies a small variation of the unknowns around their static values (marked with a tilde):

$$I(t) = I + \tilde{I}, \quad E_i(t) = E_i + \tilde{E}_i, \quad N_{\mathrm{l,r}}(t) = N_{\mathrm{l,r}} + \tilde{N}_{\mathrm{l,r}}, \tag{6.14}$$

where all variations are assumed to be much smaller than the static values. By substituting this $E(t)$ into the definition of the photon density of Eq. (2.21), and by neglecting higher-order terms, $S_{\mathrm{l,r}} = S + \tilde{S}_{\mathrm{l,r}}$ is obtained with:

$$\begin{aligned} \tilde{S}_{\mathrm{l}} &= \frac{1}{2}E_1\tilde{E}_2^* + \frac{1}{2}E_1^*\tilde{E}_2 + \frac{1}{2}E_1\tilde{E}_1^* + \frac{1}{2}E_1^*\tilde{E}_1, \\ \tilde{S}_{\mathrm{r}} &= -\frac{1}{2}E_1\tilde{E}_2^* - \frac{1}{2}E_1^*\tilde{E}_2 + \frac{1}{2}E_1\tilde{E}_1^* + \frac{1}{2}E_1^*\tilde{E}_1. \end{aligned} \tag{6.15}$$

By substituting these small-signal versions of the unknowns, by neglecting higher-order terms, and by subtracting the static equations, the small-signal model of the equations under study is obtained:

$$\begin{aligned} \partial_t\tilde{E}_1 &= \Gamma_{\mathrm{z}}G_{\mathrm{d}}\xi v_{\mathrm{g}}E_1\tilde{N}_{\mathrm{s}}, \\ \partial_t\tilde{E}_2 &= \left(\underbrace{v_{\mathrm{g}}\Gamma_{\mathrm{z}}G_{\mathrm{d}}N_{\mathrm{s}}}_{=L_1} - \frac{1}{2\tau_{\mathrm{p2}}} + \mathrm{i}\Delta\omega \right)\tilde{E}_2 + v_{\mathrm{g}}\Gamma_{\mathrm{z}}\xi E_1\tilde{N}_{\mathrm{d}}, \end{aligned} \tag{6.16}$$

where $\xi = \frac{1}{4}(1+\mathrm{i}\alpha_{\mathrm{h}})G_{\mathrm{d}}$, and N_{s} and N_{d} are the sum and difference carrier densities, defined as:

$$N_{\mathrm{s}} \triangleq N_{\mathrm{l}} + N_{\mathrm{r}}, \quad N_{\mathrm{d}} \triangleq N_{\mathrm{l}} - N_{\mathrm{r}}. \tag{6.17}$$

It can be seen that the small-signal dynamics of the lasing mode depend only on the sum carrier density N_{s}, while the dynamics of the side mode depend only on N_{d}.

The carrier equations can be expressed in terms of $N_{\mathrm{s,d}}$ by taking the sum and difference of Eq. (6.10), and by neglecting higher-order terms. In this way, two decoupled subsystems are obtained, one for $\tilde{N}_{\mathrm{s}}$ and the lasing-mode amplitude $\tilde{E}_1$:

$$\partial_t\tilde{N}_{\mathrm{s}} = -\frac{\tilde{N}_{\mathrm{s}}}{\tau_{\mathrm{n}}} + \frac{\tilde{I}_{\mathrm{s}}}{qV_{\mathrm{a}}} - v_{\mathrm{g}}G_{\mathrm{d}}\left[\tilde{N}_{\mathrm{s}}S + (N_{\mathrm{th}} - N_{\mathrm{tr}})(E_1\tilde{E}_1^* + E_1^*\tilde{E}_1)\right], \tag{6.18}$$

$$\partial_t\tilde{E}_1 = \Gamma_{\mathrm{z}}G_{\mathrm{d}}\xi v_{\mathrm{g}}E_1\tilde{N}_{\mathrm{s}}, \tag{6.19}$$

and another one for $\tilde{E}_2$ and $\tilde{N}_\mathrm{d}$, which reads:

$$\partial_t \tilde{N}_\mathrm{d} = -\frac{\tilde{N}_\mathrm{d}}{\tau_\mathrm{n}} - 2k_\mathrm{d}\tilde{N}_\mathrm{d} + \frac{\tilde{I}_\mathrm{d}}{qV_\mathrm{a}} - v_\mathrm{g}G_\mathrm{d}\left[\tilde{N}_\mathrm{d}S + (N-N_\mathrm{tr})(E_1\tilde{E}_2^* + E_1^*\tilde{E}_2)\right], \tag{6.20}$$

$$\partial_t \tilde{E}_2 = (\Delta L + \mathrm{i}\Delta\omega)\tilde{E}_2 + v_\mathrm{g}\Gamma_\mathrm{z}\xi\tilde{N}_\mathrm{d}E_1. \tag{6.21}$$

where $\tilde{I}_\mathrm{s} \triangleq \tilde{I}_\mathrm{l} + \tilde{I}_\mathrm{r}$ and $\tilde{I}_\mathrm{d} \triangleq \tilde{I}_\mathrm{l} - \tilde{I}_\mathrm{r}$. The first subsystem is a well-known complex field rate equation for a standard laser [3], which therefore describes the usual carrier–photon resonance (CPR) dynamics. The second one instead describes the PPR dynamics and therefore is the object of investigation of this section.

A phasor transform is applied to study the frequency response of Eqs. (6.21) and (6.20). Since the treated equations are complex, the complex conjugate of Eq. (6.21) is considered. Transforming the time derivative as $\mathrm{i}\omega$ yields a complex 3×3 system. To further simplify the model, the complex field equations can be considered (for $\Delta\omega < 0$) at $\partial_t = \mathrm{i}\omega = \mathrm{i}\Delta\omega$:

$$E^* \propto \frac{\tilde{N}_\mathrm{d}}{\Delta L}, \qquad E \propto \frac{\tilde{N}_\mathrm{d}}{\Delta L + 2\mathrm{i}\Delta\omega}. \tag{6.22}$$

A similar result holds for $\Delta\omega > 0$. Equation (6.22) shows that, for ω approaching $|\Delta\omega|$, one of the two electric fields is much greater than its complex conjugate. If the system has to be investigated around $\Delta\omega$, one of the two complex conjugated equations can be dropped and a two-dimensional complex system, which is an approximation of Eqs. (6.21) and (6.20), can be obtained:

$$[\mathrm{i}\omega\underline{\underline{I}} - \underline{\underline{J}}]\begin{bmatrix}\tilde{N}_\mathrm{d}\\ \tilde{E}_2\end{bmatrix} = \begin{bmatrix}\tilde{I}_\mathrm{d}/(qV_\mathrm{a})\\ 0\end{bmatrix}. \tag{6.23}$$

with:

$$J_{11} = -\frac{1}{\tau_\mathrm{n}} - v_\mathrm{g}G_\mathrm{d}S, \tag{6.24}$$

$$J_{12} = -v_\mathrm{g}G_\mathrm{d}(N-N_\mathrm{tr})E_1, \tag{6.25}$$

$$J_{21} = v_\mathrm{g}\Gamma\xi E_1, \tag{6.26}$$

$$J_{22} = \Delta L - \mathrm{i}\,|\Delta\omega|. \tag{6.27}$$

It can be noted how the modulus of $\Delta\omega$ appears in J_{22}, which is a compact equivalent to drop the *non-resonating* electric field equation (See Eq. (6.22)). The real and imaginary parts of the determinant of $\underline{\underline{J}}$ read, neglecting the recombination term, and expressing the

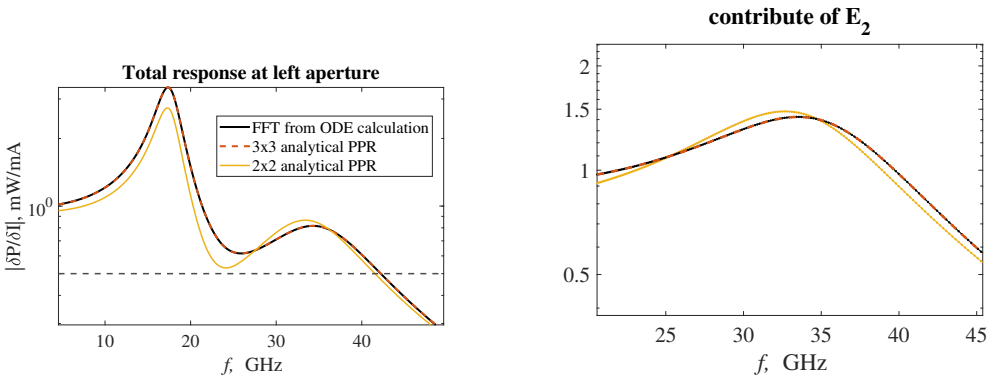

(a) (b)

Figure 6.2: Left: comparison of IMR computed with numerical integration and the 3×3 model of Eqs. (6.21) and (6.20), with the 2×2 approximation of Eq. (6.23).

negative quantity $\Delta L = -|\Delta L|$:

$$\Re(\omega) = -\omega^2 + |\Delta\omega|\,\omega + \alpha|\Delta L| + K, \tag{6.28}$$

$$\Im(\omega) = -(|\Delta L| + \alpha)\,\omega + \alpha\,|\Delta\omega| + \alpha_h\,K, \tag{6.29}$$

with:

$$K = v_g^2 G_d \Gamma \Re(\xi)\,(N - N_{tr})\,E_1^2, \qquad \alpha = v_g\,G_d\,S. \tag{6.30}$$

Since the peak of the PPR is found approximately at $\omega = \Delta\omega$, a good estimate of the maximum value of $|\tilde{E}_2|$ can be obtained by evaluating the determinant at this frequency and applying Cramer's rule, yielding:

$$|\tilde{E}_{2,\mathrm{peak}}| \approx \frac{|\tilde{I}_d|}{qV_a} \frac{v_g\Gamma|\xi|E_1}{\sqrt{(-\Delta\omega|\Delta L| + \alpha_h K)^2 + (\alpha|\Delta L| + K)^2}}. \tag{6.31}$$

Simple considerations on the derived analytical model can be made in order to explain the trends outlined in Sec. 5.2, specifically:

- Eq. (6.31) shows that the PPR peak is attenuated by the threshold-gain separation and the frequency separation.

- From inspection of Eq. (6.15), it can be seen that the dynamics of $S_l + S_r$ do not depend on the side mode $\tilde{E}_2$. For this reason, probing both cavities does not result in any bandwidth enhancement.

- The PPR dynamics are enabled by the current difference $\tilde{I}_{\mathrm{d}}$, therefore in-phase modulation of both cavities does not produce any bandwidth enhancement.

Fig. 6.2a shows a summary of the derived approximations for $\Delta f = -30\,\mathrm{GHz}$ and ΔL of 30 %. The black curve is the solution obtained with numerical integration, which is used as the benchmark. The red dotted curve is the total response obtained with the complex 3×3 system of Eqs. (6.21)–(6.20), which introduces no approximations. The yellow curve is the total response obtained by considering the 2×2 approximated system. It can be seen that the approximation is accurate only for f close to $|\Delta f|$. Figure 6.2b shows a detailed view around Δf of the sole contribution of $\tilde{E}_2$ for all the presented cases.

6.3 Stability and frequency-dependent modal competition

To investigate the stability of the static solutions of Eq. (6.13), the eigenvalues of the Jacobian associated with the nonlinear system of Eqs. (6.21) and (6.20) should be computed. This results in a three-dimensional eigenvalue problem, which would yield excessively complex expressions. To exploit the Routh stability criteria, which are well established for systems of equations with real coefficients, the real and imaginary parts of the electric field are chosen as the unknowns. This can be done by taking the sum and the difference of Eq. (6.21) with its complex conjugate. In doing so, the Jacobian reads:

$$J' = \begin{bmatrix} J_{11} & 2J_{12} & 0 \\ \Re\big(J_{21}\big) & \Delta L & \Delta\omega \\ -\alpha_{\mathrm{h}}\Re\big(J_{21}\big) & -\Delta\omega & \Delta L \end{bmatrix}. \tag{6.32}$$

Its associated characteristic polynomial is of the form $\lambda^3 + b\lambda^2 + c\lambda + d$, where:

$$\begin{aligned} d &= v_{\mathrm{g}} G_{\mathrm{d}} S\,(\Delta L^2 + \Delta\omega^2) - K\,(2\Delta L + 2\alpha_{\mathrm{h}}\Delta\omega), \\ c &= \Delta L^2 + 2J_{11}\Delta L + \Delta\omega^2 + 2K, \\ b &= -2\Delta L - J_{11}. \end{aligned} \tag{6.33}$$

The Routh criterion states that the following quantities must be positive in order for the system to be stable:

$$\begin{aligned} \mathrm{r}_1 &= b, \qquad \mathrm{r}_2 = \frac{cb-d}{b}, \\ \mathrm{r}_3 &= d. \end{aligned} \tag{6.34}$$

A recall of the sign of the various terms is useful for reading the stability criteria, specifically:

- ΔL is assumed to be negative in order for the static solution to be reasonable,
- J_{11} is negative (see Eq. (6.27)),
- K is positive (see Eq. (6.30)),
- α_h is assumed positive.

Given these considerations, b is always positive, so the analysis can be restricted to the terms:

$$\begin{aligned} \mathrm{r}_1' &= cb-d \\ &= \underbrace{(-2\Delta L)\Delta\omega^2 - 2\Delta L^3 - 4J_{11}\Delta L^2 + \left(-2K - 2J_{11}^2\right)\Delta L - 2J_{11}K}_{\text{positive}} + 2K\,\alpha_\mathrm{h}\Delta\omega > 0, \\ \mathrm{r}_2' &= d > 0. \end{aligned} \tag{6.35}$$

As a preliminary observation, note that for $\alpha_\mathrm{h} = 0$ the stability condition is always satisfied, because both r' terms are sums of positive contributions. When $\alpha_\mathrm{h} \neq 0$ (a positive value is assumed), additional dynamical instabilities arise. Starting from r_2', it can be seen that for negative $\Delta\omega$, which means that the higher-frequency mode is selected, this can become negative. The higher the optical power of the lasing mode, the stronger this effect becomes, since the α_h term is multiplied by K, which contains the photon density S. It can be seen that, for sufficiently large ΔL, this quantity can be made positive. The value of ΔL necessary to suppress this instability for each $\Delta\omega$ is referred to as ΔL_0. The analytical expression of ΔL_0 would require computing the discriminant of r_2, which is a second-order expression of $\Delta\omega$, and finding the minimum value to make the latter negative. Such a procedure is performed numerically, and its results are shown in Fig. 6.5, which reports the value of $\Delta G_0 \triangleq -\Delta L_0/(\Gamma_z v_\mathrm{g})$ as a function of the injected current and of α_h. Such values can be obtained by means of an etching, as illustrated in Fig. 5.4.

If the condition $\Delta L > |\Delta L_0|$ is met, the boundaries of the unstable region can be found by computing the roots of r_2', which yields an analytical expression for the boundaries of

the unstable region:

$$\Delta\omega_{1,2} = \frac{\alpha_h}{2\tau_p} \pm \sqrt{\left(\frac{\alpha_h}{2\tau_p}\right)^2 - \Delta L^2 - \frac{|\Delta L|}{2\tau_p}}. \tag{6.36}$$

In particular, the static solution is unstable if the frequency lies between $\Delta\omega_{12}$. The stability condition obtained in Eq. (6.36) can be met through three distinct mechanisms:

- by introducing a sufficiently large threshold-gain splitting, which makes the $\Delta\omega_{12}$ complex. This value however is not reachable with standard modal selection techniques. In particular, the solution is stable for ΔL values that fall outside the limit values:
$$\Delta L_{\pm} = \pm\frac{\sqrt{1+4\alpha_h^2}-1}{4\tau_p}. \tag{6.37}$$
the negative side however would not satisfy the condition on r_1'.
- For sufficiently large $\Delta\omega$, although in this regime no PPR effects are observed,
- for negative $\Delta\omega$, which means by selecting the odd mode.

Despite the analysis being performed for the perfectly symmetric device, this picture can be extended to explain the stability of the odd mode observed experimentally and reported in Fig. 5.12, which cannot be interpreted only in terms of gain-field overlap.

The condition on r_2' can be approximated, for small ΔL, as in devices where no modal selection is implied, as:

$$\Delta f_{12} = 0, \quad \frac{\alpha_h}{2\pi\tau_p}. \tag{6.38}$$

Figures 6.3 and 6.4 show, respectively, the real and imaginary parts of the three eigenvalues of Eq. (6.32) as functions of $\Delta\omega$ for two different values of ΔL. The unstable regions are identified by the presence of an eigenvalue with a positive real part. The roots of the characteristic polynomial include a complex conjugate pair, labeled with subscripts 2 and 3, and a purely real eigenvalue, labeled with subscript 1. Regarding the complex conjugate pair, this can be unstable for $\Delta\omega < 0$, therefore it can be associated with the coefficient r_1'. The effect of increasing ΔL is visible: for a reasonable value of threshold-gain separation, this is made stable at each frequency. The imaginary part of the complex conjugate pair is approximately equal to $\pm\Delta f$. For this reason, this mechanism can be identified as an unstable PPR oscillation. Furthermore, this root features many similarities to the one observed and investigated in [77], usually referred to as the Bogatov effect. In particular, such instability favours the lower-frequency mode, is more relevant the higher

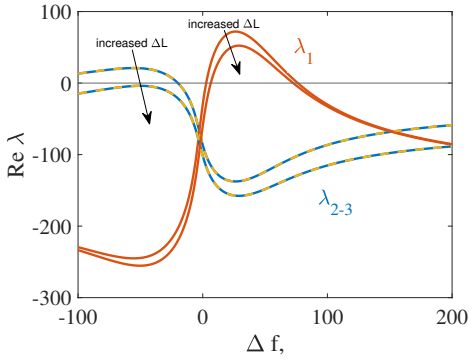

Figure 6.3: $\Re(\lambda)$ of Eq. (6.32), for increasing ΔL, expressed in GHz.

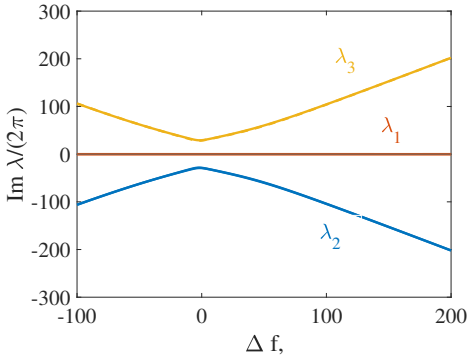

Figure 6.4: $\Im(\lambda)$ of Eq. (6.32), expressed in GHz.

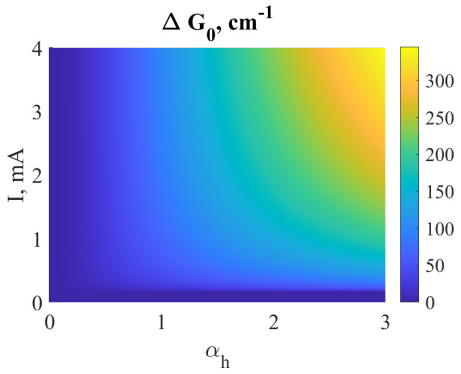

Figure 6.5: ΔL_0, expressed as an equivalent threshold gain per QW difference for varying α_h and I_0.

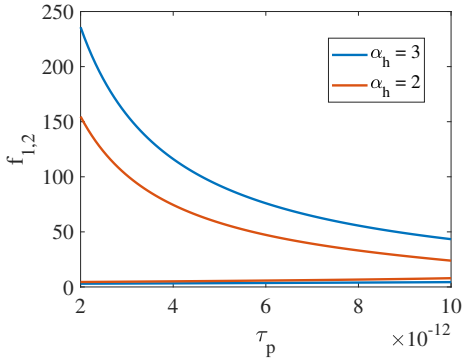

Figure 6.6: Plot of the boundaries of the stability regions expressed as frequency, GHz.

the power of the lasing mode, and features a characteristic shape of the real part of the root (see Fig. 6.3) which is similar to the one reported in [77].

The purely real root instead can become unstable for $\Delta\omega > 0$, that is when the lower-frequency mode is selected, and therefore can be associated with the coefficient r_2'. The mechanism underlying this instability is the following: a perturbation of N_d excites the side mode E_2; the excitation of E_2 modifies the photon densities S_l and S_r and burns carriers, thereby increasing N_d again and forming a positive feedback loop. This instability presents analogies with the ones reported in laser arrays [78, 79], arising from the coupled dynamics of carrier and electric field.

Finally, Fig. 6.6 shows the boundary values of such an instability region, f_{12}, obtained from Eq. (6.36). Even under pessimistic assumptions, such as $\alpha_h = 3$, the predicted unstable

region is unlikely to be observable in standard devices, where typical frequency detunings are on the order of a few hundred GHz. However, large-area VCSELs [23, 35] exhibit significantly smaller frequency spacings, potentially placing them within the unstable region identified by the present analysis. Consequently, the proposed expression may have practical implications for modal-selection mechanisms in such devices and requires further attention.

Chapter 7

Conclusions and future developments

In this thesis, a comprehensive and physically grounded modeling framework for the investigation of TCC-VCSELs has been developed, with particular emphasis on bow-tie geometries, representing a promising alternative for overcoming the intrinsic modulation bandwidth limitations of conventional VCSELs while simultaneously enabling functionalities such as beam steering and on-chip terahertz generation. However, such performance enhancements are accompanied by challenges, including dynamical instabilities and poor technological yield.

Previous modeling approaches to TCC-VCSELs have largely relied on phenomenological descriptions based on feedback, external optical injection, or perturbative coupled-cavity formulations. These approaches introduce fitting parameters that cannot be directly linked to the device geometry and therefore lack predictive capability. As a consequence, these models cannot be used to guide systematic design optimization, nor can they rigorously address the impact of self-heating and fabrication tolerances on device-level performance.

The present work introduces a paradigm shift in the modeling of TCC-VCSELs by treating them as single unconventional optical apertures rather than as assemblies of coupled sub-cavities. From this perspective, the defining feature of these devices is the unusually small frequency separation between supported transverse modes, typically on the order of tens of gigahertz rather than the hundreds of gigahertz characteristic of standard circular VCSELs. Starting from the scalar wave equation, a slowly varying envelope approximation and a modal expansion over cold-cavity eigenmodes yield a complete set of coupled rate equations governing the time evolution of the complex modal amplitudes.

In this formulation, modal coupling terms arise naturally from the spatial distribution of the carrier-induced gain and from refractive-index perturbations associated with thermal and technological effects.

Remarkably, all parameters entering the dynamical equations are modal quantities, such as field envelopes, resonance frequencies, and photon lifetimes, which can be directly extracted from electromagnetic modal simulations familiar in the VCSEL community. This establishes a direct and quantitative link between the device geometry and system-level performance, enabling predictive modeling and geometry-driven optimization. Furthermore, it is shown how the vast phenomenology of TCC-VCSELs can be understood within a unique set of equations.

The developed framework shows that the modulation response can be enhanced by the PPR and can be systematically engineered by controlling the separation between modal frequencies and threshold gains. However, analytical investigations reveal that, in perfectly symmetric devices, symmetry-breaking mechanisms, such as asymmetric pump–probe excitation schemes, are required to activate broadband PPR dynamics. Novel bow-tie geometries, such as the partially covered configuration [126], which may remove the aforementioned need for an asymmetric pump–probe scheme, can be investigated within the developed framework.

Beyond reproducing experimental behavior, the modal nature of the equations provides a clear analytical framework for the investigation of TCC-VCSELs. The analysis reveals the presence of frequency-dependent modal competition arising from the coupled carrier–field dynamics, where either higher-frequency or lower-frequency modes may be favored. This explains experimental observations of out-of-phase modal configurations that cannot be interpreted by conventional gain–field overlap arguments alone.

The impact of this work extends beyond TCC-VCSELs. The developed formalism is directly applicable to conventional VCSELs for quantifying the influence of temperature variations and fabrication tolerances, and to devices with small transverse-mode separations, such as large-area VCSELs.

In general, this thesis establishes a unified, geometry-linked, and predictive modeling platform for multimode VCSEL dynamics, providing both fundamental insight and a practical design methodology for next-generation VCSEL devices.

List of abbreviations

Acronym	Description
AR	Active region
CPR	Carrier–Photon resonance
CR	Coherent regime
CW	Continuous wave
DBR	Distributed Bragg reflector
EEL	Edge-emitting laser
FFT	Fast Fourier transform
GR	Grating relief
IMR	Intensity modulation response
LA	Left aperture
LP	Linearly polarized
MM	Multimode
MQW	Multi quantum well
MTJ	Multi-tunnel junction
PPR	Photon–photon resonance
QW	Quantum well
RA	Right aperture
RF	Radio frequency
SFM	Spin-flip model
SVEA	Slowly-varying envelope approximation
SWE	Scalar wave equation
TCC	Transverse-coupled cavity
TE	Transverse electric
TM	Transverse magnetic
VCSEL	Vertical-cavity surface-emitting laser
WCR	Weakly coupled regime

List of figures

Bibliography

[1] Rainer Michalzik, editor. *VCSELs: Fundamentals, Technology and Applications of Vertical-Cavity Surface-Emitting Lasers*, volume 166 of *Springer Series in Optical Sciences*. Springer Berlin Heidelberg, 2013.

[2] Kenichi Iga. Forty years of vertical-cavity surface-emitting laser: Invention and innovation. *Japan. J. Appl. Phys.*, 57, July 2018.

[3] L. A. Coldren and S. W. Corzine. *Diode Lasers and Photonic Integrated Circuits*. John Wiley & Sons, New York, 1995.

[4] Johannes M. Ostermann, Pierluigi Debernardi, Christof Jalics, Andrea Kroner, Martin Feneberg, Michael C. Riedl, and Rainer Michalzik. Monolithic polarization control of multimode VCSELs by a dielectric surface grating. *Vertical-Cavity Surface-Emitting Lasers VIII, Proc. SPIE 5364*, June 2004.

[5] Fortune Business Insights. VCSEL Market, 2025. https://www.fortunebusinessinsights.com/vcsel-market-110466 (2025-09-06).

[6] Heng Liu, Pei Miao, Yao Xiao, Chang Liu, Zhicheng Zhang, and Jun Wang. High performance multi-junction VCSELs for lidar applications. *Proc. SPIE, Vertical-Cavity Surface-Emitting Lasers XXVI*, 12020:1202005, 2022.

[7] Amirhossein Ghods, Karim Tatah, Mary Stocker, and Klein Johnson. Scaling characteristics of multijunction VCSELs. *IEEE Journal of Selected Topics in Quantum Electronics*, 2024.

[8] Alberto Gullino, Valerio Torrelli, Martino D'Alessandro, Alberto Tibaldi, Francesco Bertazzi, Michele Goano, and Pierluigi Debernardi. Algaas tunnel junction (tj)-VCSELs: a negf–drift-diffusion approach. *IEEE Photonics Journal*, 16(2):1–9, 2024.

[9] Yao Xiao, Jun Wang, Heng Liu, Pei Miao, Yudan Gou, Zhicheng Zhang, Guoliang Deng, and Shouhuan Zhou. Multi-junction cascaded vertical-cavity surface-emitting laser with a high power conversion efficiency of 74%. *Light: Science & Applications*, 13:60, 2024.

[10] Matthew M. Dummer, Amirhossein Ghods, Guoyang Xu, Sara Rothwell, and Klein Johnson. Single-mode multi-junction VCSELs with integrated transverse mode filter. *Proc. SPIE, Vertical-Cavity Surface-Emitting Lasers XXVII*, 12439:1243908, 2023.

[11] Guanzhong Pan, Meng Xun, Xiaoli Zhou, Yun Sun, Yibo Dong, and Dexin Wu. Harnessing the capabilities of VCSELs: unlocking the potential for advanced integrated photonic devices and systems. *Light: Science & Applications*, 13(1):229, 2024.

[12] Meng Xun, Guanzhong Pan, Zhuang Zhuang Zhao, Yun Sun, Weichao Wu, Wenjing Jiang, Runze Zhang, and Dexin Wu. High Single Fundamental-Mode Output Power From 795 nm VCSELs With a Long Monolithic Cavity. *IEEE Electron Device Lett.*, 44(7):1144–1147, July 2023.

[13] M. Huang, D. K. Serkland, and J. Camparo. A narrow-linewidth three-mirror VCSEL for atomic devices. *Appl. Phys. Lett.*, 121(11):114002, 2022.

[14] Yinli Zhou, Yuchen Jia, Xing Zhang, Jianwei Zhang, Zhanchao Liu, Yongqiang Ning, and Lijun Wang. Large-aperture single-mode 795 nm VCSEL for chip-scale nuclear magnetic resonance gyroscope with an output power of 4.1 mW at 80°c. *Opt. Express*, 30(6):8991–8999, March 2022.

[15] Kai Jin, Xuxing Geng, Zhi Liang, Wangwang Tang, Jianfeng Xiao, Heng Hu, Guangming Huang, Gaoxiang Li, Guoqing Yang, and Shangqing Liang. Design of portable self-oscillating VCSEL-pumped cesium atomic magnetometer. *MDPI Electron.*, 11(22):3666, November 2022.

[16] Quanpu Liu, Zhen Chai, Jixi Lu, Kaifeng Yin, and Jianli Li. Development of non-magnetic VCSEL module for compact atomic magnetometer. In *Proc. SPIE 12311*, page 123110U, December 2022.

[17] Yinli Zhou, Xing Zhang, Jianwei Zhang, Jinjiang Cui, Yongqiang Ning, Yugang Zeng, and Lijun Wang. Wavelength tuning robustness optimization for a high-temperature single-mode VCSEL used in chip-scale atomic sensing systems. *Appl. Opt.*, 61(9):2417–2423, March 2022.

[18] Lele Bai, Xin Wen, Yulin Yang, Lulu Zhang, Jun He, Yanhua Wang, and Junmin Wang. Quantum-enhanced rubidium atomic magnetometer based on Faraday rotation via 795 nm Stokes operator squeezed light. *J. Opt.*, 23(8):085202, August 2021.

[19] M. A. Bobrov, S. A. Blokhin, N. A. Maleev, A. A. Blokhin, A. P. Vasyl'ev, A. G. Kuzmenkov, A. S. Pazgalev, M. V. Petrenko, S. P. Dmitriev, A. K. Vershovskii, V. M. Ustinov, I. I. Novikov, and L. Ya Karachinskii. Optically pumped non-zero field magnetometric sensor for the magnetoencephalographic systems using intra-cavity contacted VCSELs with rhomboidal oxide current aperture. *J. Phys. Conf. Ser.*, 1697(1):012175, October 2020.

[20] N. A. Maleev, S. A. Blokhin, M. A. Bobrov, A. G. Kuz'menkov, M. M. Kulagina, and V. M. Ustinov. Laser source for a compact nuclear magnetic resonance gyroscope. *Gyroscopy Navig.*, 9(3):177–182, 2018.

[21] John Kitching. Chip-scale atomic devices. *Applied Physics Reviews*, 5(3), 2018.

[22] L. S. Watkins, C. Ghosh, J.-F. Seurin, D. Zhou, G. Xu, B. Xu, and A. Miglo. High power VCSEL devices for atomic clock applications. *Proc. SPIE 9616*, page 96160J, September 2015.

[23] Valerio Torrelli, Alberto Gullino, Alberto Tibaldi, Francesco Bertazzi, Michele Goano, and Pierluigi Debernardi. High-power emission via large-area VCSELs with single high-order mode operation. *IEEE Photonics Journal*, 16(2):1–7, April 2024.

[24] Xiuqin Zhan, Fa-Feng Xu, Zhonghao Zhou, Yongli Yan, Jiannian Yao, and Yong Sheng Zhao. 3d laser displays based on circularly polarized lasing from cholesteric liquid crystal arrays. *Advanced Materials*, 33(37), August 2021.

[25] Ming Kang and Jing Chen. Pseudo coherent-perfect-absorption approach toward perfect polarization conversion. *Optics Express*, 32(8):13357, March 2024.

[26] Zhiyi Yuan, Shih-Hsiu Huang, Zhen Qiao, Pin Chieh Wu, and Yu-Cheng Chen. Metasurface-tunable lasing polarizations in a microcavity. *Optica*, 10(2):269–278, Feb 2023.

[27] Xiangli Jia, Jonas Kapraun, Jiaxing Wang, Jipeng Qi, Yipeng Ji, and Connie Chang-Hasnain. Metasurface reflector enables room-temperature circularly polarized emission from VCSEL. *Optica*, 10(8):1093, August 2023.

[28] Kirill Voronin, Alexey S. Taradin, Maxim V. Gorkunov, and Denis G. Baranov. Single-handedness chiral optical cavities. *ACS Photonics*, 9(8):2652–2659, 2022.

[29] YiMing Zhu, Fan Zhang, GuanJun You, Jie Liu, John D. Zhang, Akhlesh Lakhtakia, and Jian Xu. Stable circularly polarized emission from a vertical-cavity surface-emitting laser with a chiral reflector. *Applied Physics Express*, 5(3):032102, February 2012.

[30] Valerio Torrelli, Martino D'Alessandro, Wolfgang Elsäßer, and Pierluigi Debernardi. On-demand polarization by a vertical-cavity surface-emitting laser with two tilted sub-wavelength gratings. *Opt. Lett.*, 49(13):3773–3776, Jul 2024.

[31] Valerio Torrelli, Lorenzo Miri, Martino D'Alessandro, Alberto Gullino, Michael Zimmer, Katharina Dahler, Michael Jetter, Peter Michler, Wolfgang Elsäßer, Francesco Bertazzi, Alberto Tibaldi, and Pierluigi Debernardi. Elliptical polarization in VCSELs via joint interaction of a tilted sub-wavelength grating and intrinsic semiconductor anisotropies. *Opt. Lett.*, 50(9):3082–3085, May 2025.

[32] Jason Zhang, Tan Nguyen, Benjamin Potsaid, Vijaysekhar Jayaraman, Christopher Burgner, Siyu Chen, Jinxi Li, Kaicheng Liang, Alex Cable, Giovanni Traverso, Hiroshi Mashimo, and James G. Fujimoto. Multi-MHz MEMS-VCSEL Swept-Source Optical Coherence Tomography for Endoscopic Structural and Angiographic Imaging with Miniaturized Brushless Motor Probes. *Biomedical Optics Express*, 12(4):2384–2403, 2021.

[33] G. Giuliani, M. Norgia, S. Donati, and T. Bosch. Laser diode self-mixing technique for sensing applications. *Journal of Optics A: Pure and Applied Optics*, 4:S283–S294, 2002.

[34] A. Brejnak, M. Gębski, A. K. Sokół, M. Marciniak, M. Wasiak, J. Muszalski, J. A. Lott, I. Fischer, and T. Czyszanowski. Boosting the output power of large-aperture lasers by breaking their circular symmetry. *Optica*, 8(9):1167–1175, Sep 2021.

[35] Anas Skalli, Joshua Robertson, Dafydd Owen-Newns, Matej Hejda, Xavier Porte, Stephan Reitzenstein, Antonio Hurtado, and Daniel Brunner. Photonic neuromorphic computing using vertical cavity semiconductor lasers. *Opt. Mater. Express*, 12(6):2395–2414, Jun 2022.

[36] Xavier Porte, Anas Skalli, Nasibeh Haghighi, Stephan Reitzenstein, James A. Lott, and Daniel Brunner. A complete, parallel and autonomous photonic neural network in a semiconductor multimode laser. *Journal of Physics: Photonics*, 3(2):024017, 2021.

[37] Hsin chieh Yu, Zhi wei Zheng, Yang Mei, Rong bin Xu, Jian ping Liu, Hui Yang, Bao ping Zhang, Tien chang Lu, and Hao chung Kuo. Progress and prospects of GaN-based VCSEL from near UV to green emission. *Progress in Quantum Electronics*, 57:1–19, 2018.

[38] G. Cardinali, F. Hjort, N. Prokop, J. Enslin, M. Cobet, M. A. Bergmann, J. Gustavsson, J. Ciers, I. Häusler, T. Kolbe, T. Wernicke, Å. Haglund, and M. Kneissl. Low-threshold AlGaN-based UVB VCSELs enabled by post-growth cavity detuning. *Applied Physics Letters*, 121(10):103501, 09 2022.

[39] Alexander Andrejew, Stephan Sprengel, and Markus Christian Amann. Gasb-based vertical-cavity surface-emitting lasers with an emission wavelength at 3 µm. *Optics Letters*, 41(12):2799–2802, June 2016.

[40] Andrea Simaz, Gerhard Böhm, Anna Köninger, and Mikhail A. Belkin. Low-Loss Tunnel Junction Integration in Mid-Infrared VCSELs. In *Conference on Lasers and Electro-Optics/Europe (CLEO/Europe 2025) and European Quantum Electronics Conference (EQEC 2025)*, page 45. Optica Publishing Group, 2025.

[41] Hui Li and Xiaowei Jia. Comparative study on stained InGaAs quantum wells for high-speed optical-interconnect VCSELs. *Optics Communications*, 415:1–5, 2018.

[42] Anjin Liu, Philip Wolf, James A. Lott, and Dieter Bimberg. Vertical-cavity surface-emitting lasers for data communication and sensing. *Photon. Res.*, 7(2):121–136, February 2019.

[43] Babu Dayal Padullaparthi, Jim A. Tatum, and Kenichi Iga, editors. *VCSEL industry - Communication and sensing*. John Wiley & Sons, Hoboken (NJ), 1st edition, 2022.

[44] Nikolay N. Ledentsov, O. Yu. Makarov, V. A. Shchukin, V. P. Kalosha, N. Ledentsov, L. Chrochos, M. Bou Sanayeh, and J. P. Turkiewicz. High speed VCSEL technology and applications. *J. Lightwave Technol.*, 40(6):1749–1763, March 2022.

[45] Muralikrishnan Srinivasan, Jinxiang Song, Alexander Grabowski, Krzysztof Szczerba, Holger K. Iversen, Mikkel N. Schmidt, Darko Zibar, Jochen Schröder, Anders Larsson, Christian Häger, and Henk Wymeersch. End-to-end learning for VCSEL-based optical interconnects: State-of-the-art, challenges, and opportunities. *J. Lightwave Technol.*, 41(11):3261–3277, June 2023.

[46] Petter Westbergh, Johan S. Gustavsson, Benjamin Kogel, Åsa Haglund, Anders Larsson, and A. Joel. Higher speed VCSELs by photon lifetime reduction. In *Proc. SPIE Vertical-Cavity Surface-Emitting Lasers XV*, 2011.

[47] Petter Westbergh, Johan S. Gustavsson, Benjamin Kogel, Åsa Haglund, and Anders Larsson. Impact of photon lifetime on high-speed VCSEL performance. *IEEE J. Select. Topics Quantum Electron.*, 17(6):1603–1613, November 2011.

[48] Erik Haglund, Petter Westbergh, Johan S. Gustavsson, Emanuel P. Haglund, and Anders Larsson. High-Speed VCSELs With Strong Confinement of Optical Fields and Carriers. *J. Lightwave Technol.*, 34(2):269–277, January 2016.

[49] Martino D'Alessandro, Alberto Gullino, Alberto Tibaldi, Francesco Bertazzi, Michele Goano, and Pierluigi Debernardi. Physics-Based Time-Domain Modeling of VCSELs. In *2022 International Conference on Numerical Simulation of Optoelectronic Devices (NUSOD)*, pages 61–62, 2022.

[50] Anders Larsson, Johan S. Gustavsson, Attila Fülöp, Erik Haglund, Emanuel P. Haglund, and André Kelkkanen. The future of VCSELs: Dynamics and speed limitations. In *2020 IEEE Photonics Conference (IPC)*, September 2020.

[51] Hao-Tien Cheng, Yun-Cheng Yang, Te-Hua Liu, and Chao-Hsin Wu. Recent advances in 850 nm VCSELs for high-speed interconnects. 9(2):107, February 2022.

[52] Jingyi Wang, Ramana M. V. Murty, Sizhu Jiang, David W. Dolfi, and et al. 200 Gb/s PAM4 oxide VCSEL development progress at Broadcom. In *Proc. SPIE Vertical-Cavity Surface-Emitting Lasers XXIX*, 2025.

[53] Daniel M. Kuchta, Alexander V. Rylyakov, Clint L. Schow, Jonathan E. Proesel, Christian W. Baks, Petter Westbergh, Johan S. Gustavsson, and Anders Larsson. A 50 Gb/s NRZ modulated 850 nm VCSEL transmitter operating error free to 90 °c. *J. Lightwave Technol.*, 33(4):802–810, February 2015.

[54] Jiao Zhang, Pengqi Gou, Miao Kong, Kaibo Fang, Jiangnan Xiao, Qi Zhang, Xiangjun Xin, and Jianjun Yu. PAM-8 IM/DD transmission based on modified lookup table nonlinear predistortion. *IEEE Photon. J.*, 10(3):1–9, June 2018.

[55] Honghang Zhou, Yan Li, Yuyang Liu, Lei Yue, Chao Gao, Wei Li, Jifang Qiu, Hongxiang Guo, Xiaobin Hong, Yong Zuo, and Jian Wu. Recent advances in equalization technologies for short-reach optical links based on PAM4 modulation: A review. *MDPI Appl. Sci.*, 9(11):2342, March 2019.

[56] Leonardo Minelli, Fabrizio Forghieri, Antonino Nespola, Stefano Straullu, and Roberto Gaudino. A multi-rate approach for nonlinear pre-distortion using end-to-end deep learning in IM-DD systems. *J. Lightwave Technol.*, 41(2):420–431, January 2023.

[57] Ludovic Marigo-Lombart, Christophe Viallon, Alexandre Rumeau, Alexandre Arnoult, Aurélie Lecestre, Laurent Mazenq, Ayad Ghannam, Hugo Thienpont, Krassimir Panajotov, and Guilhem Almuneau. Electro-absorption modulator vertically integrated on a VCSEL: Microstrip-based high-speed electrical injection on top of a bcb layer. *Journal of Lightwave Technology*, 37(15):3861–3868, 2019.

[58] Markus Lindemann, Gaofeng Xu, Tobias Pusch, Rainer Michalzik, Martin R Hofmann, Igor Žutić, and Nils C Gerhardt. Ultrafast spin-lasers. *Nature*, 568(7751):212–215, 2019.

[59] Stewart T. M. Fryslie, Zihe Gao, Harshil Dave, Bradley J. Thompson, Katherine Lakomy, Shiyun Lin, Patrick J. Decker, David K. McElfresh, José E. Schutt-Ainé, and Kent D. Choquette. Modulation of coherently coupled phased photonic crystal vertical cavity laser arrays. *IEEE J. Select. Topics Quantum Electron.*, 23(6):1700409, 2017.

[60] Elham Heidari, Hamed Dalir, Moustafa Ahmed, Volker J. Sorger, and Ray T. Chen. Hexagonal transverse-coupled-cavity VCSEL redefining the high-speed lasers. *Nanophoton.*, 9(16):4743–4748, 2020.

[61] W. North, N. Jahan, P. Strzebonski, A. Khurana, S. E. Ralph, and K. D. Choquette. Analysis and characterization of photon-photon resonance in coupled dual-element photonic crystal vertical cavity surface emitting laser arrays. *J. Lightwave Technol.*, 42(1):236–242, 2024.

[62] Hamed Dalir and Fumio Koyama. Bandwidth enhancement of single-mode VCSEL with lateral optical feedback of slow light. *IEICE Electron. Express*, 8(13):1075–1081, 2011.

[63] Da Chen, Ye Liu, and Yonglin Yu. Understanding the photon-photon resonance of DBR lasers using mode expansion method. *Opt. Quantum Electron.*, 55:29, November 2022.

[64] Hamed Dalir and Fumio Koyama. 29 ghz directly modulated 980 nm vertical-cavity surface emitting lasers with bow-tie shape transverse coupled cavity. *Applied Physics Letters*, 103(9), 2013.

[65] R. Lang and K. Kobayashi. External optical feedback effects on semiconductor injection laser properties. *IEEE J. Quantum Electron.*, 16(3):347–355, March 1980.

[66] Moustafa Ahmed, Ahmed Bakry, Mohamed S. Alghamdi, Hamed Dalir, and Fumio Koyama. Enhancing the modulation bandwidth of VCSELs to the millimeter-waveband using strong transverse slow-light feedback. *Opt. Express*, 23(12):15365–15371, 2015.

[67] William North, Nusrat Jahan, Pawel Strzebonski, and Kent D. Choquette. Modal characteristics of coupled vertical cavity surface emitting laser diode arrays. *J. Appl. Phys.*, 132(17):173102, 2022.

[68] Pawel J. Strzebonski, William North, Nusrat Jahan, and Kent D. Choquette. Analysis of coherence and coupling in vertical cavity surface emitting laser arrays. *IEEE J. Quantum Electron.*, 58(4):2400508, August 2022.

[69] Harshil Dave, Zihe Gao, Stewart Thomas McKee Fryslie, Bradley J. Thompson, and Kent D. Choquette. Static and dynamic properties of coherently-coupled photonic-crystal vertical-cavity surface-emitting laser arrays. *IEEE Journal of Selected Topics in Quantum Electronics*, 25(6):1–8, 2019.

[70] Zihe Gao, Stewart T. M. Fryslie, Bradley J. Thompson, P. Scott Carney, and Kent D. Choquette. Parity-time symmetry in coherently coupled vertical cavity laser arrays. *Optica*, 4(3):323–329, 2017.

[71] Mohammad-Ali Miri and Andrea Alù. Exceptional points in optics and photonics. *Science*, 363(6422):eaar7709, 2019.

[72] Pawel Strzebonski and Kent D. Choquette. Complex waveguide supermode analysis of coherently-coupled microcavity laser arrays. *IEEE Journal of Selected Topics in Quantum Electronics*, 28(1: Semiconductor Lasers):1–6, 2022.

[73] N. Ledentsov Jr., V. A. Shchukin, Ł. Chorchos, O. Yu. Makarov, J.-R. Kropp, I. E. Titkov, V. P. Kalosha, V. Zerova, M. Lindemann, N. C. Gerhardt, M. D'Alessandro, V. Torrelli, P. Debernardi, A. Tibaldi, M. R. Hofmann, and N. N. Ledentsov. Analysis of laterally-coupled-cavity VCSELs for ultra-high-frequency photon-photon resonance modulation. In Chun Lei and Kent D. Choquette, editors, *Vertical-Cavity Surface-Emitting Lasers XXVIII*, volume 12904, page 1290405. International Society for Optics and Photonics, SPIE, 2024.

[74] M. Lindemann, N. C. Gerhardt, M.R. Hofmann, N. Jr. Ledentsov, V. A. Shchukin, N. N. Ledentsov, O. Yu. Makarov, Ł. Chorchos, and J. P. Turkiewicz. Coupled aperture VCSELs suitable for 100 GHz intensity modulation. In *2023 23rd International Conference on Transparent Optical Networks (ICTON)*, August 2023.

[75] Markus Lindemann, Martino D'Alessandro, Nikolay N. Ledentsov, O. Yu. Makarov, N. C. Gerhardt, and M. R. Hofmann. Laterally coupled vertical-cavity surface-emitting lasers with tunable resonance width and frequency. *J. Appl. Phys.*, 138(5):053102, August 2025.

[76] Yinghui Hu, Carsten Brenner, Martin R. Hofmann, and Markus Lindemann. Coherent CW THz generation with a coupled-cavity mini-array VCSEL. *Electronics Letters*, 61(1):e70146, 2025.

[77] A. Bogatov, P. Eliseev, and B. Sverdlov. Anomalous interaction of spectral modes in a semiconductor laser. *IEEE Journal of Quantum Electronics*, 11(7):510–515, 1975.

[78] F. Prati, D. Vecchione, and G. Vendramin. Frequency locking of supermodes and stability of the out-of-phase-locked state in one-dimensional and two-dimensional arrays of vertical-cavity surface-emitting lasers. *Opt. Lett.*, 22(21):1633–1635, Nov 1997.

[79] H. G. Winful and S. S. Wang. Stability of phase locking in coupled semiconductor laser arrays. *Applied Physics Letters*, 53(20):1894–1896, 11 1988.

[80] G. Ghione. *Semiconductor Devices for High-Speed Optoelectronics*. Cambridge University Press, Cambridge, U.K., 2009.

[81] Antoine Pissis, Eimantas Duda, Stefano Tirelli, Urs Siegenthaler, David Quandt, Donato Bonfrate, Pratyush Das Kanungo, Martin Spieser, and Evgeny Zibik. Efficient tunnel junction lithographic aperture 940 nm VCSEL. *IEEE Photonics Technology Letters*, 35(7):389–392, 2023.

[82] Giuseppe Pio Pisa. Temperature-dependent rate equation model for high-speed vertical-cavity surface-emitting lasers. Master's thesis, Politecnico di Torino, academic year 2020/21 2020. Electronic, Corso di laurea magistrale in Ingegneria Elettronica (Electronic Engineering).

[83] Alberto Tibaldi, Francesco Bertazzi, Michele Goano, Rainer Michalzik, and Pierluigi Debernardi. VENUS: a Vertical-cavity surface-emitting laser Electro-opto-thermal NUmerical Simulator. *IEEE J. Select. Topics Quantum Electron.*, 25(6):1500212, November/December 2019.

[84] Y. Ou, J. S. Gustavsson, P. Westbergh, A. Haglund, A. Larsson, and A. Joel. Impedance characteristics and parasitic speed limitations of high-speed 850-nm VCSELs. *IEEE Photonics Technology Letters*, 21(24):1840–1842, 2009.

[85] Anders Larsson, Per Westbergh, Joel S. Gustavsson, Erik Haglund, and Emma P. Haglund. High-speed VCSELs and VCSEL arrays for single- and multi-core fiber interconnects. In *Vertical-Cavity Surface-Emitting Lasers XIX*, volume 9381 of *Proceedings of SPIE*, pages 93810D–1, San Francisco, CA, 2015. SPIE.

[86] Alexander Grabowski, Johan S. Gustavsson, and Anders Larsson. Impact of carrier transport and capture on VCSEL dynamics. *IEEE Journal of Quantum Electronics*, 59(1):1–6, 2023.

[87] F. Prati, A. Tesei, L. A. Lugiato, and R. J. Horowicz. Stable states in surface-emitting semiconductor lasers. *Chaos Solitons Fractals*, 4(8–9):1637–1654, August 1994.

[88] C. H. Henry. Theory of the linewidth of semiconductor lasers. *IEEE J. Quantum Electron.*, QE-18(2):259–264, February 1982.

[89] G. Ronald Hadley. Effective index model for vertical-cavity surface-emitting lasers. *Opt. Lett.*, 20(13):1483–1485, 2005.

[90] Allan W Snyder, John D Love, et al. *Optical waveguide theory*, volume 175. Chapman and hall London, 1983.

[91] Weng Cho Chew. Lectures on theory of microwave and optical waveguides, 2021. arXiv:2107.09672 [physics.class-ph].

[92] G. P. Bava, P. Debernardi, and L. Fratta. Three-dimensional model for vectorial fields in vertical-cavity surface-emitting lasers. *Phys. Rev. A*, 63(2):23816, 2001.

[93] P. Debernardi, G. P. Bava, F. Monti di Sopra, and M. B. Willemsen. Features of vectorial modes in phase-coupled VCSEL arrays: experiments and theory. *IEEE J. Quantum Electron.*, 39(1):109–119, January 2003.

[94] Pierluigi Debernardi, Johannes Michael Ostermann, Markus Sondermann, Thorsten Ackemann, Gian Paolo Bava, and Rainer Michalzik. Theoretical-experimental study of the vectorial modal properties of polarization-stable multimode grating VCSELs. *IEEE Journal of Selected Topics in Quantum Electronics*, 13(5):1340–1348, 2007.

[95] P. Debernardi. HOT-VELM: a comprehensive and efficient code for fully vectorial and 3-D hot-cavity VCSEL simulation. *IEEE J. Quantum Electron.*, 45(8):979–992, August 2009.

[96] Torrelli Valerio. *Vertical-cavity surface-emitting lasers: computer-aided modal and polarization engineering*. PhD thesis, Politecnico di Torino, 2025.

[97] Martino D'Alessandro, Valerio Torrelli, Francesco Bertazzi, Michele Goano, Nikolay N. Ledentsov, Markus Lindemann, Mariangela Gioannini, Pierluigi Debernardi, and Alberto Tibaldi. Transverse coupled cavity VCSELs: Bridging ultrabroadband dynamics to optical supermodes. *IEEE Photonics Journal*, 16(2):1–7, 2024.

[98] M. San Miguel, Q. Feng, and J. V. Moloney. Light-polarization dynamics in surface-emitting semiconductor lasers. *Phys. Rev. A*, 52:1728–1739, Aug 1995.

[99] J. Martín-Regalado, M. San Miguel, N. B. Abraham, and F. Prati. Polarization switching in quantum-well vertical-cavity surface-emitting lasers. *Opt. Lett.*, 21(5):351–353, Mar 1996.

[100] Markus Lindemann, Gaofeng Xu, Tobias Pusch, Rainer Michalzik, Martin R. Hofmann, Igor Žutić, and Nils C. Gerhardt. Ultrafast spin-lasers. *Nature*, 568(7751):212–215, April 2019.

[101] M. San Miguel, Q. Feng, and J. V. Moloney. Light-polarization dynamics in surface-emitting semiconductor lasers. *Physical Review A*, 52(2):1728–1739, August 1995.

[102] Yohann G. Sanvert, Jules Mercadier, Stefan Bittner, Angel Valle, and Marc Sciamanna. Polarization and transverse-mode nonlinear dynamics in a multimode vcsel. *Opt. Lett.*, 50(24):7645–7648, Dec 2025.

[103] Johannes Michael Ostermann, Pierluigi Debernardi, and Rainer Michalzik. Polarization-controlled surface grating VCSELs under unpolarized and polarized optical feedback. *IEEE Photonics Technology Letters*, 19(18):1359–1361, 2007.

[104] J. M. Ostermann, P. Debernardi, C. Jalics, and R. Michalzik. Polarization-stable oxide-confined VCSELs with enhanced single-mode output power via monolithically integrated inverted grating reliefs. *IEEE J. Select. Topics Quantum Electron.*, 11(5):982–989, 2005.

[105] Luigi Lugiato, Franco Prati, and Massimo Brambilla. *The adiabatic elimination principle*, page 105–111. Cambridge University Press, 2015.

[106] Martino D'Alessandro, Valerio Torrelli, Pierluigi Debernardi, Alberto Gullino, Keyvan Azimi Asrari, Markus Lindemann, Thomas de Adelsburg Ettmayer, Guido Giuliani, and Alberto Tibaldi. Modelling coherent emission in transverse coupled cavity VCSELs. In *NUSOD 2025*, September 2025.

[107] Martino D'Alessandro, Nikolay Ledentsov Jr., Vitaly A. Shchukin, Nikolai N. Ledentsov, Markus Lindemann, and Alberto Tibaldi. Physics-based computer-aided modelling of transverse coupled cavity VCSELs. In Kent D. Choquette and Luke A. Graham, editors, *Vertical-Cavity Surface-Emitting Lasers XXIX*, volume PC13384, page PC1338405. International Society for Optics and Photonics, SPIE, 2025.

[108] Christophe Geuzaine and Jean-François Remacle. Gmsh: A 3-D finite element mesh generator with built-in pre- and post-processing facilities. *International Journal for Numerical Methods in Engineering*, 79(11):1309–1331, 2009.

[109] Philip Trøst Kristensen, Kathrin Herrmann, Francesco Intravaia, and Kurt Busch. Modeling electromagnetic resonators using quasinormal modes. *Advances in Optics and Photonics*, 12(3):612–702, 2020.

[110] P. T. Kristensen, C. Van Vlack, and S. Hughes. Generalized effective mode volume for leaky optical cavities. *Optics Letters*, 37(10):1649–1651, 2012.

[111] Philippe Lalanne, Wei Yan, Kevin Vynck, Christophe Sauvan, and Jean-Paul Hugonin. Light interaction with photonic and plasmonic resonances. *Laser & Photonics Reviews*, 12(5):1700113, 2018.

[112] P. T. Leung, S. Y. Liu, and K. Young. Completeness and orthogonality of quasinormal modes in leaky optical cavities. *Physical Review A*, 49(4):3057–3074, 1994.

[113] E. A. Muljarov and W. Langbein. Exact mode volume and purcell factor of open optical systems. *Physical Review B*, 94(23):235438, 2016.

[114] E. Kapon, J. Katz, and A. Yariv. Supermode analysis of phase-locked arrays of semiconductor lasers. *Opt. Lett.*, 9(4):125–127, 1984.

[115] W. J. Fader and G. E. Palma. Normal modes of n coupled lasers. *Opt. Lett.*, 10(8):381–383, Aug 1985.

[116] Mirvais Yousefi and Daan Lenstra. Rate-equation description of multi-mode semiconductor lasers. In *Proc. SPIE 8980*, page 89800B, February 2014.

[117] Cristina Rimoldi, Marco Novarese, Lorenzo Luigi Columbo, Sebastian Romero García, Christian Raabe, and Mariangela Gioannini. Near-field measurement and four-wave mixing in single-polarization elliptical multimode VCSELs. *Journal of Physics: Photonics*, 8(1):015002, nov 2025.

[118] Cristina Rimoldi, Lorenzo L. Columbo, Alberto Tibaldi, Pierluigi Debernardi, Sebastian Romero García, Christian Raabe, and Mariangela Gioannini. Impact of coherent mode coupling on noise performance in elliptical aperture vcsels for datacom. *IEEE Journal of Selected Topics in Quantum Electronics*, 31(2: Pwr. and Effic. Scaling in Semiconductor Lasers):1–13, 2025.

[119] Martino D'Alessandro, Valerio Torrelli, Francesco Bertazzi, Michele Goano, Nikolay N. Ledentsov, Markus Lindemann, Mariangela Gioannini, Pierluigi Debernardi, and Alberto Tibaldi. Transverse coupled cavity VCSELs: Bridging ultrabroadband dynamics to optical supermodes. *IEEE Photon. J.*, 16(2):0600807, 2024.

[120] M. Lindemann, N. C. Gerhardt, M.R. Hofmann, N. Ledentsov, V. A. Shchukin, N. N. Ledentsov, O. Yu. Makarov, Ł. Chorchos, and J. P. Turkiewicz. Coupled aperture VCSELs suitable for 100 ghz intensity modulation. In *2023 23rd International Conference on Transparent Optical Networks (ICTON)*, pages 1–4, 2023.

[121] Hamed Dalir and Fumio Koyama. 29 GHz directly modulated 980 nm vertical-cavity surface emitting lasers with bow-tie shape transverse coupled cavity. *Appl. Phys. Lett.*, 103(9):091109, 2013.

[122] Martino D'Alessandro, Markus Lindemann, Nikolay Ledentsov, Nikolay N. Ledenstov, and Alberto Tibaldi. Physics-oriented model for bow-tie VCSELs. In *2024 IEEE Photonics Conference (IPC)*, pages 1–2, 2024.

[123] Chih-Hao Chang, L. Chrostowski, and C.J. Chang-Hasnain. Injection locking of VCSELs. *IEEE Journal of Selected Topics in Quantum Electronics*, 9(5):1386–1393, 2003.

[124] Najm M. Al-Hosiny. 3d injection-locking maps of semiconductor laser under multiple optical injections. *Journal of Optics*, 50(4):629–636, 2021.

[125] Cheng Wang, Frédéric Grillot, Vassilios Kovanis, and Jacky Even. Rate equation analysis of injection-locked quantum cascade lasers. *Journal of Applied Physics*, 113, 02 2013.

[126] Chuyu Zhong, Jian Feng, Shupeng Deng, Shihao Ding, Wenjie Rao, Shaochi Pan, Zhao Chen, Xing Zhang, Wei Miao, Nannan Li, et al. Breaking the bandwidth limit of vertical-cavity surface-emitting lasers by selective spatial-mode outcoupling. *Laser & Photonics Reviews*, page e00880, 2025.